Summer 2010

Coherent strong field interactions between a nanomagnet and a photonic cavity

Öney Orhunç Soykal
University of Iowa

COHERENT STRONG FIELD INTERACTIONS BETWEEN A NANOMAGNET AND A PHOTONIC CAVITY

by

Öney Orhunç Soykal

An Abstract

Of a thesis submitted in partial fulfillment of the
requirements for the Doctor of Philosophy
degree in Physics in the
Graduate College of The
University of Iowa

July 2010

Thesis Supervisor: Professor M. E. Flatté

ABSTRACT

Strong coupling of light and matter is an essential element of cavity quantum electrodynamics (cavity-QED) and quantum optics, which may lead to novel mixed states of light and matter and to applications such as quantum computation. In the strong-coupling regime, where the coupling strength exceeds the dissipation, the light-matter interaction produces a characteristic vacuum Rabi splitting. Therefore, strong coupling can be utilized as an effective coherent interface between light and matter (in the form of electron charge, spin or superconducting Cooper pairs) to achieve components of quantum information technology including quantum memory, teleportation, and quantum repeaters. Semiconductor quantum dots, nuclear spins and paramagnetic spin systems are only some of the material systems under investigation for strong coupling in solid-state physics. Mixed states of light and matter coupled via electric dipole transitions often suffer from short coherence times (nanoseconds). Even though magnetic transitions appear to be intrinsically more quantum coherent than orbital transitions, their typical coupling strengths have been estimated to be much smaller. Hence, they have been neglected for the purposes of quantum information technology.

However, we predict that strong coupling is feasible between photons and a ferromagnetic nanomagnet, due to exchange interactions that cause very large numbers of spins to coherently lock together with a significant increase in oscillator strength while still maintaining very long coherence times. In order to examine this new exciting possibility, the interaction of a ferromagnetic nanomagnet with a single photonic mode of a cavity is analyzed in a fully quantum-mechanical treatment. Exceptionally large quantum-coherent magnet-photon coupling with coupling terms in excess of several THz are predicted to be achievable in a spherical cavity of ~ 1 mm radius with a nanomagnet of ~ 100 nm radius and ferromagnet resonance frequency of ~ 200 GHz. This should substantially exceed the coupling observed in solids

between orbital transitions and light. Eigenstates of the nanomagnet-photon system correspond to entangled states of spin orientation and photon number over 10^5 values of each quantum number. Initial coherent state of definite spin and photon number evolve dynamically to produce large coherent oscillations in the microwave power with exceptionally long dephasing times of few seconds. In addition to dephasing, several decoherence mechanisms including elementary excitation of magnons and crystalline magnetic anisotropy are investigated and shown to not substantially affect coherence upto room temperature. For small nanomagnets the crystalline magnetic anisotropy of the magnet strongly localize the eigenstates in photon and spin number, quenching the potential for coherent states and for a sufficiently large nanomagnet the macrospin approximation breaks down and different domains of the nanomagnet may couple separately to the photonic mode. Thus the optimal nanomagnet size is predicted to be just below the threshold for failure of the macrospin approximation. Moreover, it is shown that initially unentangled coherent states of light (cavity field) and spin (nanomagnet spin orientation) can be phase-locked to evolve into a coherent entangled states of the system under the influence of strong coupling.

Abstract Approved: _____
Thesis Supervisor

_____
Title and Department

_____
Date

COHERENT STRONG FIELD INTERACTIONS BETWEEN A NANOMAGNET AND A PHOTONIC CAVITY

by

Öney Orhunç Soykal

A thesis submitted in partial fulfillment of the
requirements for the Doctor of Philosophy
degree in Physics in the
Graduate College of The
University of Iowa

July 2010

Thesis Supervisor: Professor M. E. Flatté

Graduate College
The University of Iowa
Iowa City, Iowa

CERTIFICATE OF APPROVAL

PH.D. THESIS

This is to certify that the Ph.D. thesis of

Öney Orhunç Soykal

has been approved by the Examining Committee
for the thesis requirement for the Doctor of
Philosophy degree in Physics at the July 2010
graduation.

Thesis Committee: _____
Michael E. Flatté, Thesis Supervisor

_____
David R. Andersen

_____
Wayne N. Polyzou

_____
Craig E. Pryor

_____
Markus Wohlgenannt

To my family

ACKNOWLEDGMENTS

First and foremost, I owe my deepest gratitude to my supervisor, Professor Michael E. Flatté, for his encouragement and guidance from the initial to the final level. This thesis would not have been possible without his immense insight, knowledge, and continuous support. One simply could not wish for a better or more inspirational supervisor. I also wish to thank Professor Craig E. Pryor for his support and helpful discussions on many occasions. It was an honor for me to have Professor Wayne N. Polyzou, Professor Markus Wohlgenannt, and Professor David R. Andersen in my committee with their support and insights on the subject. I am very grateful to have an extremely friendly and interactive research group, and I am indebted to all of my colleagues in our group for their friendship and support. In particular, my special thanks to my colleague and good friend Dr. Amrit De for his support and fruitful discussions. I also would like to thank my family for their understanding, selfless love and caring through this work. Last but not least, I would like to thank love of my life, my wife and aşkım Christine, for being there for me with her infinite patience, love, and caring.

TABLE OF CONTENTS

LIST OF TABLES vi

LIST OF FIGURES vii

CHAPTER

1 INTRODUCTION 1

1.1 Strong Field Interactions between a Nanomagnet and a Photonic Cavity 3
1.2 Atom-Cavity Interaction Models 5
1.2.1 Jaynes-Cummings Model 5
1.2.2 Standard Dicke Model 11
1.2.3 Tavis-Cummings Model 16
1.3 Spin Wave Theory 23
1.3.1 Direct Exchange Interaction and Magnons 23
1.3.2 Ferromagnetic Resonance 31
1.4 Spin Torque Nano Oscillators 32
1.4.1 Spin Torque from a Single Electron at an Interface . . 34
1.4.2 Spin-Flip and Spin-Wave Relaxation Time 36
1.4.3 Stimulated Emission of Spin Waves 39

2 SPIN-CAVITY HAMILTONIAN 40

2.1 Spherical Wave Expansion of the Cavity Field in the presence of Intrinsic Magnetization 41
2.2 Second Quantization of the Cavity Field Modes 43
2.2.1 TE mode 45
2.2.2 TM mode 47
2.3 Interaction Hamiltonian 48

3 SOLUTIONS OF THE SPIN-CAVITY HAMILTONIAN 53

3.1 Fock Basis Representation 53
3.2 Continuous Representation 56
3.3 Coherent-State Representation 63
3.3.1 Fock Representation of the Coherent State 64
3.3.2 Coordinate Representation of the Coherent State . . . 66
3.3.3 Coherent State of the Spin-Cavity Hamiltonian 67

4 DECOHERENCE MECHANISMS 73

4.1 Elementary Excitation of Magnons 73
4.2 Magnetocrystalline Anisotropy 76
4.3 Effects of the Nanomagnet Size 79

5 PHASE-LOCKING OF LIGHT AND SPIN COHERENT STATES 87

5.1 Coherent States of Light and Spin 87
5.2 Phase-locked Photon-Spin System 91

6 CONCLUSION 94

APPENDIX

A BASIS FUNCTIONS FOR TE AND TM MODES 96

BIBLIOGRAPHY 98

LIST OF TABLES

Table

4.1 Crystalline magnetic anisotropy energies E_{CMA} for different nanomagnet sizes (with radii r_0 and consisting of N spins) are shown in comparison with the magnet-photon coupling strength at the superradiance regime ($\tau(n_0)$). 85

LIST OF FIGURES

Figure

1.1 Energy level diagram of an n molecule gas, each molecule having 2 nondegenerate energy levels. Spontaneous radiation rates are indicated. $E_m = mE$. As illustrated in Ref. [1] 15

1.2 Schematic of matrix representation of H. As illustrated in Ref. [2] . . 18

1.3 Submatrix for given r and c. As illustrated in Ref. [2] 19

1.4 Selected eigenvalues $A_n^{(r,c,j)}$. As illustrated in Ref. [2] 22

2.1 Schematic of our nanomagnet-microcavity system consists of a spherical nanomagnet of radius 100 nm placed at a distance of d from the center of a microcavity of radius R. A uniform magnetic field, $\boldsymbol{B}$, is applied along the **z**-axis causing the precession of the total nanomagnet spin, $\boldsymbol{S}$, with frequency of ω. 41

2.2 The orientations of the electric $\boldsymbol{E}$ and magnetic field $\boldsymbol{H}$ at the nanomagnet site are shown for transverse magnetic (TM) and transverse electric (TE) modes of the photonic cavity. 44

3.1 Lattice-like schematic of the spin-cavity Hamiltonian is shown where successive lattice sites represent the corresponding photon numbers in the microcavity. Note that the constant of motion of the Hamiltonian can also be clearly seen from the addition of arrows belonging to the nanomagnet spins along the z-axis S_z (*purple*) and corresponding cavity photon numbers n (*red*) for each site. 54

3.2 The effective potential of the magnet-cavity system (for $N = 10^9$ spins) in the WKB approximation is shown with respect to cavity photon number n centered around the superradiance regime n_0. 60

3.3 Normalized wavefunctions of the nanomagnet-cavity system consisting of 10^2 spins obtained from the exact solutions (*black, dotted*), and from the continuous WKB (*red, solid*) approximation are shown for the (a) ground state, and (b) 1^{st}, (c) 2^{nd}, (d) 3^{rd}, (e) 10^{th}, and (f) 15^{th} excited states. 61

3.4 Normalized wavefunctions of the nanomagnet-cavity system consisting of 10^3 spins obtained from the exact solutions (*black, dotted*), and from the continuous WKB (*red, solid*) approximation are shown for the (a) ground state, and (b) 1^{st}, (c) 2^{nd}, (d) 3^{rd}, (e) 10^{th}, and (f) 15^{th} excited states. 62

3.5 Some wavefunctions of the nanomagnet-cavity system are shown as a function of photon number, n, centered about the equilibrium point $n_0 = 4\xi/3 = 6.66667 \times 10^8$ for $N = 10^9$ spins: (a) ground state with a width of roughly 10^4 photons(spins), (b) 1^{st}, (c) 2^{nd}, and (d) 150^{th} excited states. 63

3.6 Matching between the Gaussian function with FWHM $\simeq 46199$ (*Red*) and the ground state of the nanomagnet-cavity system centered at $n_0 = 6.67 \times 10^8$ (*Blue,dashed*) is shown with respect to photon number x of the cavity. 68

3.7 Amplitude of the coherent state of the nanomagnet-cavity system is shown as a function of photon number $x - n_0$ at times $t = 0$, and $t = 2.37$ μs. The large oscillations of this coherent state about $n_0 = 6.667 \times 10^8$ occurs between -267000 (*Filled*), and 267000 (*Dashed*) in photon numbers with a period of $T = 4.74$ μs. 70

3.8 Time evolution of the Zeeman energy of the nanomagnet (*Red*), and the amplitude of the transverse magnetic cavity field for the TM mode (*Purple*) are shown in the coherent representation of the spin-cavity system. 70

3.9 Autocorrelation function between the initial coherent state $|\phi(0)\rangle$ and the coherent state at any given time $|\phi(t)\rangle$, defined as $P(t) = |\langle\phi(t)|\phi(0)\rangle|^2$, is shown as a function of time t. 72

3.10 Dephasing time of the coherent state is obtained by the Gaussian fit of e^{-t^2/τ^2} to the peak values of the auto-correlation function at successive time intervals. 72

4.1 Temperature dependence of magnon numbers is shown by using density of states approach (*Blue*) and exact summation (*Red*) over all possible $\boldsymbol{k}$'s for the size of the nanomagnet in consideration. Fitting of a function in the form of $\alpha T^{3/2}$ to the exact summation data yields to the expected temperature behavior of magnons with $\alpha \approx 756$ K$^{-3/2}$. 74

4.2 Due to the calculated number of magnons N_m excited in the spin system, the reduction percentage of the total magnetic moment $\boldsymbol{J}$ is shown with respect to temperature T. 75

4.3 Spheroidal charge distribution and the relative spin directions is shown in two different type of configurations. The energy of (a) is different than the energy of (b) due to spin-orbit interactions. 77

4.4 Wave functions of the nanomagnet-cavity system shown as a function of photon number, n, centered about n_0, for nanomagnets of radius $r_0 = 2.3, 11, 50$ nm, consisting of $N = 10^4$, $N = 10^6$, and $N = 10^8$ spins respectively. First row (a)-(e)-(i) are the ground states with a full width half maximum (FWHM) represented in photon numbers, second row (b)-(f)-(j) are the first excited states, third row (c)-(g)-(k) are the second excited states, and the fourth row (d)-(h)-(l) are the 150^{th} excited states. 80

4.5 Amplitude of a coherent state for 3 different nanomagnet-photon systems consisting of (a) $N = 10^4$, (b) $N = 10^6$, and (c) $N = 10^8$ spins are shown as a function of photon number n. The large oscillations of these coherent states occur about (a) $n_0 \sim 6666$ with a period of $T = 1.5ms$, (b) $n_0 \sim 6.66 \times 10^5$ with a period of $T = 150\mu s$, and (c) $n_0 \sim 6.66 \times 10^7$ with a period of $T = 15\mu s$, respectively. 81

4.6 Time evolution of the Zeeman energy of the nanomagnets (*red*, *solid*) consisting of (a) $N = 10^4$, (b) $N = 10^6$, and (c) $N = 10^8$ spins are shown in coherent state representation as well as the amplitude of the transverse magnetic mode of the cavity field (*blue*, *dashed*) at nanomagnet location $z = d$. 82

4.7 Dephasing time of the coherent state for nanomagnet-photon systems of (a) $N = 10^4$, (b) $N = 10^6$, and (c) $N = 10^8$ spins (or equivalently photons) obtained by a Gaussian fit to the peak values of the dephasing functions (insets) at successive time intervals. Each peak value represents the amount of correlation after every full period T of oscillation. 84

5.1 Coherent states of light with respect to photon number n are shown with different given values of $\alpha = 5.0(Red), 8.2(Green), 9.0(Blue)$ for a system of 100 photons, whereas superradiance region is represented by dashed lines. 89

5.2 Coherent states of spin with respect to S_z eigenvalues m are shown with different given values of $\phi = 0.5(Red), 0.7(Green), 2.0(Blue)$ for a system of $S = 50$ ($\xi = 50$, corresponding to 100 spin one-halves), whereas superradiance region is represented by dashed lines. 90

5.3 For $N = 100$ spins and photons, the initial independent photon (*Red*) and spin (*Blue*) coherent states before the interaction is turned on are shown for different values of α and ϕ (a)-(f)-(k), whereas superradiance regime is represented by a *Dashed* line. For each initial configuration (columns), products of these photon and spin coherent states (*Green*) under the influence of coupling are plotted for times $t = 0$, 0.01, 0.1, and 1 seconds with respect to photon number n. 92

CHAPTER 1
INTRODUCTION

Modern cavity quantum electrodynamics (CQED) provides the most fundamental machinery for calculating coherent properties in quantum mechanics, and has long been a central paradigm for the study of open quantum systems. Even though experiments on atoms in cavities can be explained by elementary models, measurements still reveal intriguing subtleties of the influences of external couplings on coherent dynamics. Since any open system is never more than partially coherent, quantum mechanics at its conceptual core takes coherence for granted. However, full consideration of realistic quantum phenomena requires a lot more than a straightforward integration of the Scrödinger equation. Modern research on open quantum systems inspects these differences between axiomatic theory and empirical realism as it seeks to answer some of the most pressing open issues such as decoherence and the emergence of semiclassical dynamics in micro- and mesoscopic physics.

The term "cavity" refers to an optical or microwave resonator, whereas "QED" implies the interaction of some matter system (usually atomic) with the electromagnetic field (photons) inside the cavity. Enclosure in a high-quality cavity can largely isolate a matter-photon system from decohering interactions with its environment, causing the system to maintain quantum coherence over dynamically important time scales. The high degree of coherence achievable in CQED experiments makes them ideal candidates to test the basic principles of some very important rising fields in modern technological outlook such as quantum control and quantum computation. Since, according to quantum mechanics, the joint entity consisting of a system and its environment must evolve in an overall coherent fashion, coherences that originate within the system of interest will tend to be converted into entanglements between the system and the environment. As this process diminishes the coherence of the system alone, and is thereby called decoherence, figuratively one can think of coherence leaking out from

the system into the environment. Therefore, a cavity in CQED can be understood as means of minimizing such leakage from a localized system of interacting atoms and photons. Recent research in the literature has identified a strong coupling regime for CQED [3], in which the atom-photon coupling (the vacuum Rabi frequency) is much larger than both the atomic dipole decay rate and the cavity field decay rate. The decisive accomplishment of strong coupling has been an achievement of recent experimental work in microwave [4, 5], and optical [3] CQED with alkali atoms.

These CQED systems can then be used to implement schemes for quantum information processing. Further advances in experimental CQED have been achieved in the past decade. Quantum nondemolition measurements with the realization of a universal quantum logic gate [6, 7], quantum nonlinear optics providing entry to a quantum regime for nonlinear optics [8], atom-cavity microscopy resulting in sensitive measurements of an individual atom's motion [9, 10], quantum state synthesis making the preparation of single-photon Fock states possible [11, 12], nonclassical correlations testing the theoretical models of entanglement and dehocerence [13, 14] are only some of the highlights of recent progress in CQED.

Moreover, strong coupling between light and electronic transitions [3–5, 15, 16] permits coherent transfer of quantum information between the two systems, as well as a host of exotic phenomena, including slow light [17, 18], lasing without population inversion [19, 20], and index enhancement via quantum coherence [21, 22]. One of the most striking applications harnessing such a powerful consequence of strong coupling via CQED is the teleportation of an unknown qubit (the unit quanta of information) between two distant systems without physical transfer of the associated quantum-information carrier [23]. The teleportation can be achieved via preparation of initial maximally entangled states between a target qubit B and an auxiliary qubit C, and successive Bell measurements on an input qubit A and C. This teleportation scheme is successfully demonstrated in various experiments [24–28]. Because of its purely

quantum nature, teleportation can be attained in systems that exhibit a fully quantum behaviour such as cavity QED, i.e. coherent strong coupling between Rydberg atoms and cavity photons [4, 29–33]. In cavity QED schemes, the main idea for teleportation is indeed to harness the coherent atom-field interaction using cavity field modes or additional atoms as auxiliary systems.

Due to shorter coherence time of electrical dipole transitions in solids compared to atoms, strong coupling between light and electronic transitions in solids has been challenging; however, strong coupling in a single quantum dot-semiconductor microcavity system [34] has been demonstrated with a coupling strength $\sim 80\ \mu$eV. The strong coupling investigations are often focused on electric dipole (orbital) transitions instead of magnetic (spin) transitions, whose typical oscillator are estimated [35] to be smaller by a factor of the fine structure constant, ~ 137. However, the recent investigations has shown that paramagnetic spin systems in solids appear intrinsically more quantum coherent than orbital coherent states [36, 37]. Collective spin-photon effects such as superradiance [38–40] (including molecular magnets of ~ 10 spins [41]) in these systems are also demonstrated recently.

1.1 Strong Field Interactions between a Nanomagnet and a Photonic Cavity

The coherent strong-field properties of ferromagnetic systems still remain to be explored. In ferromagnets, the exchange interaction can cause a very large number of spins to lock together into one macrospin with a corresponding increase in oscillator strength. Therefore, for nanomagnets with ~ 100 spins or more, the spin-photon coupling strength may exceed that of a two-level electronic orbital transition occuring by electric dipole coupling, while still maintaining long coherence times. In this area, ferromagnetic nanomagnet oscillators have been demonstrated [42, 43] with Q factors in excess of 500. Such ferromagnetic oscillations can also be coherently driven by electrical spin currents [43–48]. Thus a single coupled nanomagnet-photonic mode

system provides an efficient method of strongly coupling electronic, magnetic, and photonic degrees of freedom.

In this thesis, a new physical realization of a CQED system based on the interaction of a many-spin (rather than atomic) system confined into a ferromagnetic nanomagnet with a single mode of a photonic cavity is introduced and strong field interactions between the two are examined. Since the spin system, where each spin acting like a two-level system, can be confined into a very small nanomagnet compared to the wavelength of the cavity mode, it can be treated like a giant macrospin with collective spin operators. A dramatic enhancement of spin-photon coupling relative to paramagnetic spin systems, yielding coupling much larger than found by coupling light to orbital transitions is predicted. The Hamiltonian of the spin-cavity system (obtained in a fully quantum treatment by using collective spin operator approach and the second quantization of the spherical cavity modes satisfying the appropriate boundary conditions) is given in Chapter 2. Note that only in the sense of atomic systems, some CQED models such as Jaynes-Cummings Model (JCM) [49] for the interaction of a single atom with a single mode of the cavity, and standard Dicke Model [1] for N gas molecules, or Tavis-Cummings Model [2, 50] for more generalized case of N atoms, have already been introduced in order to explain the matter-cavity interactions. However, none of these models were able to examine the coherent interaction of ferromagnetic systems without applying very strict approximations, or using very specific asymptotic limits of the problem. Morever, since none of these models have been developed for spin systems, they also lack the means of easily obtaining some of the very important features of modern CQED such as real-time feedback to compensate the effects of decoherence. These models will be emphasized further in the following sections of this chapter. Furthermore, some of the striking similarities such as superradiance phenomena and the isomorphism of the spin subspaces between the obtained Hamiltonian and the standard Dicke Model will be

highlighted in Chapter 3, in addition to the introduction of the methods of obtaining the corresponding solutions for the nanomagnet-cavity system. Possible decoherence mechanisms, including elementary excitation of magnons and magnetocyrstalline anisotropy, as well as the effect of nanomagnet size on the coherent properties of the nanomagnet-photonic cavity will be taken into consideration in the Chapter 4. Finally, in Chapter 5, the phase-locking of light and spin coherent states under strong coupling will be examined followed by the concluding remarks of Chapter 6.

1.2 Atom-Cavity Interaction Models

1.2.1 Jaynes-Cummings Model

Jaynes-Cummings Model (JCM) is the most elementary model proposed in 1963 by E. Jaynes and F. Cummings [49] in order to examine the relationship between the quantum theory of radiation, where the quantized electromagnetic field-expansion coefficients satisfy the Weyl-Heisenberg commutation relations, and the semiclassical theory, where the electromagnetic field is considered as an explicit function of time rather than as an operator. It describes the system of a two-level atom interacting with a quantized single mode of a cavity and is of great interest in atomic physics and quantum optics [51, 52] both experimentally and theoretically. The revival of the atomic population inversion after its collapse [53–55] is a direct consequence of the quantum treatment of the field as photon number states and this is a pure quantum effect that can be described by the JCM, but not with the semi-classical theory. It also provides the simplest illustration of spontaneous emission, and therefore explains the effects of various quantum statistics of the field in complicated systems such as masers and lasers [56, 57].

The interaction of a single-electron atom with a radiation field $\boldsymbol{E}$ can be described by the following Hamiltonian in the dipole approximation:

$$\mathscr{H} = \mathscr{H}_A - e\boldsymbol{r} \cdot \boldsymbol{E} + \mathscr{H}_F, \tag{1.1}$$

where $\mathscr{H}_A$, and $\mathscr{H}_F$ are the energies for the atom and the radiation field, respectively. The position vector of the electron is given by $\boldsymbol{r}$ in the absence of the interaction, and the field is assumed to be uniform over the whole atom in the dipole approximation.

The energy of the free field $\mathscr{H}_F$ is given as

$$\mathscr{H}_F = \sum_{\boldsymbol{k}} \hbar\nu_k \left(a_{\boldsymbol{k}}^\dagger a_{\boldsymbol{k}} + \frac{1}{2}\right), \tag{1.2}$$

in terms of the creation and annihilation operators. $\mathscr{H}_A$ and and $e\boldsymbol{r}$ can be expressed in terms of the atom transition operators

$$\sigma_{ij} = |i\rangle\langle j|, \tag{1.3}$$

where $|i\rangle$ represents a complete set of atomic energy eigenstates, satisfying the completeness relation, $\sum_i |i\rangle\langle i| = 1$. Therefore, the energy for the atom is given by

$$\mathscr{H}_A = \sum_i E_i |i\rangle\langle j| = \sum_i E_i \sigma_{ii}, \tag{1.4}$$

in terms of the atom transition operators. Similarly, $e\boldsymbol{r}$ can be expressed in terms of the electric dipole transition matrix element, $\varrho_{ij} = e\langle i|\boldsymbol{r}|j\rangle$, as

$$e\boldsymbol{r} = \sum_{i,j} e|i\rangle\langle i|\boldsymbol{r}|j\rangle\langle j| = \sum_{i,j} \varrho_{ij}\sigma_{ij}. \tag{1.5}$$

The electric field operator, evaluated at the position of the atom in dipole approximation, can be written as:

$$\boldsymbol{E} = \sum_{\boldsymbol{k}} \hat{\mathbf{e}}_{\boldsymbol{k}} \varepsilon_{\boldsymbol{k}} (a_{\boldsymbol{k}} + a_{\boldsymbol{k}}^\dagger), \tag{1.6}$$

where $\varepsilon_{\boldsymbol{k}} = (\hbar\nu_k/2\epsilon_0 V)^{1/2}$ considered in a linear polarization basis.

Finally, substituting for $\mathscr{H}_F$, $\mathscr{H}_A$, $e\boldsymbol{r}$, and $\boldsymbol{E}$ from Eqs. (1.2), (1.4), (1.5), and (1.6) into Eq. (1.1), and omitting the zero-point energy from the first term results with the following Hamiltonian:

$$\mathscr{H} = \sum_{\boldsymbol{k}} \hbar\nu_{\boldsymbol{k}} a_{\boldsymbol{k}}^\dagger a_{\boldsymbol{k}} + \sum_i E_i \sigma_{ii} + \sum_{i,j} \sum_{\boldsymbol{k}} g_{\boldsymbol{k}}^{ij} \sigma_{ij} \left(a_{\boldsymbol{k}} + a_{\boldsymbol{k}}^\dagger\right) \tag{1.7}$$

where

$$g_{\boldsymbol{k}}^{ij} = -\frac{\varrho_{ij} \cdot \hat{\mathbf{e}}_{\boldsymbol{k}} \varepsilon_{\boldsymbol{k}}}{\hbar}. \tag{1.8}$$

By defining $\varrho_{eg} = \varrho_{ge}$, and $g = g_{\boldsymbol{k}}^{eg} = g_{\boldsymbol{k}}^{ge}$ for the case of a two-level atom and a

single mode of the field, one can proceed with the Hamiltonian

$$\mathscr{H} = \hbar\nu a^\dagger a + (E_e\sigma_{ee} + E_g\sigma_{gg}) + \hbar g(\sigma_{eg} + \sigma_{ge})(a + a^\dagger). \tag{1.9}$$

Note that by using the relations $E_e - E_g = \hbar\omega$ and $\sigma_{ee} + \sigma_{gg} = 1$, the second term can be rewritten as

$$E_e\sigma_{ee} + E_g\sigma_{gg} = \frac{1}{2}\hbar\omega\left(\sigma_{ee} - \sigma_{gg}\right) + \frac{1}{2}\left(E_e + E_b\right), \tag{1.10}$$

where the constant energy term $\left(E_e + E_g\right)/2$ can be ignored. Furthermore, using the following notations:

$$\sigma_z = \sigma_{ee} - \sigma_{gg} = |e\rangle\langle e| - |g\rangle\langle g|, \tag{1.11}$$

$$\sigma_+ = \sigma_{eg} = |e\rangle\langle g|, \tag{1.12}$$

$$\sigma_- = \sigma_{ge} = |g\rangle\langle e|, \tag{1.13}$$

in Eq. (1.9), will yield to the final Hamiltonian,

$$\mathscr{H} = \mathscr{H}_0 + \mathscr{H}_I, \tag{1.14}$$

describing the interaction of a single mode quantized field of frequency ν with a single two-level atom, where

$$\mathscr{H}_0 = \hbar\nu a^\dagger a + \frac{1}{2}\hbar\omega\sigma_z, \tag{1.15}$$

$$\mathscr{H}_I = \hbar g\left(\sigma_+ a + \sigma_- a^\dagger\right). \tag{1.16}$$

Note that the interaction energy in Eq. (1.9) actually consists of four terms. The term $\sigma_- a^\dagger$ corresponds to the process in which the atom is taken from the excited state into the ground state and a photon is created, whereas the term $\sigma_+ a$ describes the opposite process. The energy is conserved in both processes. However, the term $\sigma_- a$ corresponds to the process in which the atom makes a transition from the excited to the ground state and a photon is annihilated, resulting in the loss of roughly $2\hbar\omega$ in energy. Similarly, the term $\sigma_+ a^\dagger$ results with a gain of $2\hbar\omega$ in energy. Therefore, these energy nonconserving terms have been dropped in Eq. (1.16) by using the

rotating-wave approximation [58].

The Hamiltonian in the interaction picture, can be obtained as

$$\begin{aligned} \mathscr{V} &= e^{i\mathscr{H}_0 t/\hbar}\mathscr{H}_I e^{-i\mathscr{H}_0 t/\hbar} \\ &= \hbar g\left(\sigma_+ a e^{i\Delta t} + \sigma_- a^\dagger e^{-i\Delta t}\right), \end{aligned} \tag{1.17}$$

where $\Delta = \omega - \nu$. Therefore, the equation of motion for $|\psi\rangle$, given by

$$i\hbar\frac{\partial|\psi\rangle}{\partial t} = \mathscr{V}|\psi\rangle, \tag{1.18}$$

can be easily solved with the substitution of

$$|\psi(t)\rangle = \sum_n \left[c_{e,n}(t)|e,n\rangle + c_{g,n}(t)|g,n\rangle\right], \tag{1.19}$$

and the projection of the resulting equations onto $\langle e,n|$, and $\langle g,n+1|$, while keeping in mind that the interaction energy in Eq. (1.17) can only cause transitions between the states $|e,n\rangle$, and $|g,n+1\rangle$. Therefore, the following coupled differential equations

$$\dot{c}_{e,n} = -ig\sqrt{n+1}e^{i\Delta t}c_{g,n+1}, \tag{1.20}$$

$$\dot{c}_{g,n+1} = -ig\sqrt{n+1}e^{-i\Delta t}c_{e,n}, \tag{1.21}$$

can be solved exactly as:

$$\begin{aligned} c_{e,n}(t) &= \left\{c_{e,n}(0)\left[\cos\left(\frac{\Omega_n t}{2}\right) - \frac{i\Delta}{\Omega_n}\sin\left(\frac{\Omega_n t}{2}\right)\right]\right. \\ &\quad \left. -\frac{2ig\sqrt{n+1}}{\Omega_n}c_{g,n+1}(0)\sin\left(\frac{\Omega_n t}{2}\right)\right\}e^{i\Delta t/2}, \end{aligned} \tag{1.22}$$

$$\begin{aligned} c_{g,n+1}(t) &= \left\{c_{g,n+1}(0)\left[\cos\left(\frac{\Omega_n t}{2}\right) + \frac{i\Delta}{\Omega_n}\sin\left(\frac{\Omega_n t}{2}\right)\right]\right. \\ &\quad \left. -\frac{2ig\sqrt{n+1}}{\Omega_n}c_{e,n}(0)\sin\left(\frac{\Omega_n t}{2}\right)\right\}e^{-i\Delta t/2}, \end{aligned} \tag{1.23}$$

where the Rabi frequency is defined as

$$\Omega_n^2 = \Delta^2 + 4g^2(n+1). \tag{1.24}$$

Assuming the atom is initially in the excited state $|e\rangle$ then $c_{e,n}(0) = c_n(0)$, and $c_{g,n+1} = 0$. Here, $c_n(0)$ is the probability amplitude for the field alone. Therefore, the

complete solution of the problem is reached as

$$c_{e,n}(t) = c_n(0)\left[\cos\left(\frac{\Omega_n t}{2}\right) - \frac{i\Delta}{\Omega_n}\sin\left(\frac{\Omega_n t}{2}\right)\right] e^{i\Delta t/2}, \tag{1.25}$$

$$c_{g,n+1}(t) = -c_n(0)\frac{2ig\sqrt{n+1}}{\Omega_n}\sin\left(\frac{\Omega_n t}{2}\right) e^{-i\Delta t/2}. \tag{1.26}$$

All the physically important quantities related to the atom and the quantized field can be easily obtained from Eqs. (1.25), and (1.26).

For instance, the probability $p(n)$ that there are n photons in the field at time t is obtained by taking the trace over the atomic states, i.e.,

$$\begin{aligned} p(n) &= |c_{e,n}(t)|^2 + |c_{g,n}(t)|^2 \\ &= \rho_{n,n}(0)\left[\cos^2\left(\frac{\Omega_n t}{2}\right) + \left(\frac{\Delta}{\Omega_n}\right)^2 \sin^2\left(\frac{\Omega_n t}{2}\right)\right] \\ &\quad + \rho_{n-1,n-1}(0)\left(\frac{4g^2 n}{\Omega_{n-1}^2}\right)\sin^2\left(\frac{\Omega_{n-1} t}{2}\right), \end{aligned} \tag{1.27}$$

where $\rho_{nn}(0) = |c_n(0)|^2$ is the probability that there are n photons present in the field at time $t = 0$. An initial coherent state can be defined by the following Poisson distribution:

$$\rho_{nn}(0) = \frac{\langle n\rangle^n e^{-\langle n\rangle}}{n!}. \tag{1.28}$$

Another physically important quantity is the population inversion $W(t)$ obtained as:

$$W(t) = \sum_n \left[|c_{e,n}|^2 - |c_{g,n}|^2\right] \tag{1.29}$$

$$= \sum_{n=0}^{\infty} \rho_{nn}(0)\left[\frac{\Delta^2}{\Omega_n^2} + \frac{4g^2(n+1)}{\Omega_n^2}\cos(\Omega_n t)\right]. \tag{1.30}$$

by substituting for the probability amplitudes $c_{e,n}(t)$ and $c_{g,n}(t)$ from Eqs. (1.25) and (1.26), respectively. It is important to note that even for initial vacuum field, defined by $\rho_{nn}(0) = \delta_{n0}$, it can be clearly seen from

$$W(t) = \frac{1}{\Delta^2 + 4g^2}\left\{\Delta^2 + 4g^2\cos\left(\sqrt{\Delta^2 + 4g^2}t\right)\right\} \tag{1.31}$$

that Rabi oscillations still take place. This is drastically different from the predictions of the semiclassical theory, since in semiclassical theory the atom in the excited state

can not make a transition to the lower state in the absence of a driving field. However, in the quantum picture, the transition from the upper state to the lower state in the vacuum becomes possible due to spontaneous emission. The envelope of the sinusoidal Rabi oscillations collapses to zero and we encounter a revival of the collapsed inversion as time increases. As this behavior of collapse and revival of inversion takes place repeatedly with a decreasing amplitude of Rabi oscillations, the time duration in which revival takes place increases and ultimately overlaps with the earlier revival.

The phenomena of collapse and revival can be physically described by Eq. (1.30). Each term in the summation corresponds to the Rabi oscillations for a definite value of n, whereas the photon distribution function $\rho_{nn}(0)$ stands for the relative weight for each value of n. Since initially, $t = 0$, the atom is prepared in a definite initial state, all the terms in the summation are correlated. However, since the Rabi oscillations associated with different excitations have different frequencies, as time passes they become uncorrelated leading to a collapse of inversion. As time is further increased, the correlation gets restored leading to a revival of inversion. An infinite sequence of revivals occur with the repetition of this behavior. These revivals occur only because of the discreteness of the photon distribution, and therefore, it is a pure quantum phenomenon. As known from semiclassical theory, a continuous photon distribution related to a classical random field, would give a collapse, but no revivals.

The time period τ_R of the Rabi oscillations is given by the inverse of the Rabi frequency Ω_n at $n = \langle n \rangle$, i.e.,

$$\tau_R \sim \frac{1}{\Omega_{\langle n \rangle}} = \frac{1}{\left(\Delta^2 + 4g^2\langle n \rangle\right)^{1/2}}, \tag{1.32}$$

in the limit of $\langle n \rangle \gg 1$.

1.2.2 Standard Dicke Model

Dicke Model is one of the most interesting models, which is of particular importance for nuclear magnetic resonance experiments [59, 60], some microwave spectroscopic applications [61–63], Raman scattering [64–71], and study of quantum phase transitions [72–74], proposed in 1954 by R. H. Dicke to describe the interaction of N two-level atomic systems with a single mode of a field. By considering a radiating gas as a single quantum-mechanical system, it examines the energy levels corresponding to certain correlations between individual gas molecules. Spontaneous emission of radiation in a transition between two such levels results with coherent radiation for a gas of small dimension compared with a wavelength. It also includes the effect of photon recoil momentum on coherence for a gas of large extent. Morever, the effect of a radiation pulse in super-radiant states can be obtained with Dicke Model.

Before the Dicke Model was proposed, the usual treatment of spontaneous radiation by a gas was considered as though the separate molecules radiate independently of each other. Intuitively, one might argue that the probability of a given molecule emitting a photon should be independent of the states of other molecules since molecules are seperated by large distances and subsequently interacting in a weak regime. However, this earlier simplified model ignores the fact that all the molecules are coupled by interacting with a common radiation field and hence can not be treated as independent.

In the following derivations, the gas as a whole is considered as a single quantum-mechanical system to find the energy eigenstates corresponding to the correlated motions in the system. The spontaneous emission of coherent radiation accompany transitions between such levels.

The gas is assumed to be confined into a small volume compared with the radiation wavelength. Degeneracy and collision broadening are neglected in order to reduce the scope of the problem to its bare essentials. It is also assumed that the

gas has a very low density and therefore there is not enough overlapping of the wave functions of separate molecules to require the wave function symmetrization. The Hamiltonian for an N molecule gas system in the absence of the radiation field is given by

$$\mathscr{H} = H_0 + E\sum_{j=1}^{n} R_{jz}, \tag{1.33}$$

where molecular excitation is defined as $E = \hbar\omega$. H_0 represents the translational and intermolecular interaction energies of the gas in the center-of-mass coordinate system, whereas the internal energy of the jth molecule is given by ER_{jz} with an eigenvalue of $\pm\frac{1}{2}E$. Since H_0 and all the R_{jz} commute with each other, energy eigenfunctions are chosen to be the simultaneous eigenfunctions of H_0,R_{1z},R_{2z},...,R_{Nz} given as

$$\psi_{gm} = U_g\left(\boldsymbol{r_1}\cdots\boldsymbol{r_N}\right)\left[+_1 +_2 -_3 +_4 \cdots +_N\right] \tag{1.34}$$

where $\boldsymbol{r_j}$, and $\pm_j$ represent the center-of-mass coordinates of the N molecules, and the two levels of the internal energy states of the various molecules, respectively. If the number of molecules for the energy states $+$ and $-$ are given by N_+ and N_-, respectively, then m is defined as

$$\begin{aligned} m &= \frac{1}{2}\left(N_+ - N_-\right), \\ N &= N_+ + N_-. \end{aligned} \tag{1.35}$$

Therefore, the total energy of the system is given by

$$E_{gm} = E_g + mE \tag{1.36}$$

where the energy of motion and mutual interaction of the molecules is denoted by E_g which satisfies $H_0U_g = E_gU_g$. The degeneracy only due to the interchange of internal coordinates of the energy E_{gm} is

$$\frac{N!}{\left(\frac{1}{2}N+m\right)!\left(\frac{1}{2}N-m\right)!}. \tag{1.37}$$

Moreover, the degeneracy of the total wave function depends upon whether or not the molecules are distinguishable or not. However, the molecules have no overlapping

wavefunctions, because the gas is assumed to have a very low density. Therefore, the distinguishability of the molecules has no further effect.

Except for the factor $\frac{1}{2}$, R_{jz} is analogous to the Pauli spin operator σ_z, and therefore the other two orthogonal operators analogous to σ_x and σ_y can be introduced satisfying the following relations:

$$\begin{aligned} R_{jx}\left[\ldots \pm_j \ldots\right] &= \frac{1}{2}\left[\ldots \mp_j \ldots\right], \\ R_{jy}\left[\ldots \pm_j \ldots\right] &= \pm\frac{1}{2} i \left[\ldots \mp_j \ldots\right]. \end{aligned} \tag{1.38}$$

Assuming the interaction of each molecule with the electromagnetic field is electric dipole, the interaction energy of the jth molecule with the field can be written as

$$-\boldsymbol{A}\left(\boldsymbol{r_j}\right) \cdot \sum_{k=1}^{N-1} \frac{e_k}{m_k c} \boldsymbol{P}_k. \tag{1.39}$$

where e_k and m_k are the charge and the mass of the kth molecule. Since $\boldsymbol{P}_k$ is the corresponding momentum of the molecule in the center-of-mass coordinate system and it is an odd operator, it has only off-diagonal terms in a representation of the internal energy basis. Therefore, the interaction Hamiltonian can be written as

$$\mathscr{H}_I = -\sum_j \boldsymbol{A}\left(\boldsymbol{r_j}\right) \cdot \left(\mathbf{e}_1 R_{jx} + \mathbf{e}_2 R_{jy}\right) \tag{1.40}$$

in terms of the operators introduced in Eq. (1.38), where $\mathbf{e}_1$ and $\mathbf{e}_2$ are vectors which are the same for all molecules. Summation over the molecules can be carried out easily as

$$\mathscr{H}_I = -\boldsymbol{A}(0) \cdot \left(\mathbf{e}_1 R_{jx} + \mathbf{e}_2 R_{jy}\right) \tag{1.41}$$

by omitting the dependence of the vector potential on the center of mass of the molecules with the assumption that the dimensions of the container confining the gas are small compared with the field wavelength. Since the interaction Hamiltonian in Eq. (1.41) does not contain the center-of-mass coordinates, the selection rule for the molecular motion quantum number g is obtained as $\Delta g = 0$. Therefore, there is also no effect of Doppler broadening on the transition frequency. Moreover, the selection

rule for m is given by $\Delta m = \pm 1$. Because of the very close analogy between this formalism and that of a system of spin-$\frac{1}{2}$ particles, known results can be taken over from the angular momentum and spin formalism.

Since $\mathscr{H}$ and R^2 commute, stationary states can be chosen to be simultaneous eigenkets of both operators. The operator R^2 has eigenvalues $r(r+1)$ where r (the so-called "cooperation number") satisfies the following relation:

$$|m| \leq r \leq \frac{1}{2}n. \tag{1.42}$$

The new eigenstates ψ_{gmr} in terms of cooperation number r can be denoted by

$$\mathscr{H}\psi_{gmr} = (E_g + mE)\,\psi_{gmr}, \tag{1.43}$$

$$R^2\psi_{gmr} = r(r+1)\psi_{gmr}. \tag{1.44}$$

The degeneracy of the stationary states is not completely removed by introducing R^2 and still have a degeneracy of

$$\frac{N!(2r+1)}{\left(\frac{1}{2}N + r + 1\right)!\left(\frac{1}{2}N - r\right)!}. \tag{1.45}$$

The nondegenerate state given by $\psi_{g,\frac{1}{2}N,\frac{1}{2}N} = U_g\,[+ + \ldots +]$ has the largest value of m and r as $r = m = \frac{1}{2}N$. All the states with the same value of $r = \frac{1}{2}N$, but with different values of m, are also nondegenerate and can be generated as

$$\psi_{gmr} = \left[\frac{R_x - iR_y}{\sqrt{R^2 - R_z^2 - R_z}}\right]^{r-m} \psi_{grr}. \tag{1.46}$$

Note that $R_x - iR_y$ act like an angular momentum ladder operator, and reduces the value of m by unity. With the same approach, the states with $r = \frac{1}{2}N - 1$ can be generated with $(N-1)$-fold degeneracy, the states with $r = \frac{1}{2}N - 2$ with $\frac{1}{2}N(N-3)$-fold degeneracy, and so on. This procedure can be repeated until all states for all possible values of r are generated.

By using the elements of the interaction Hamiltonian

$$\langle g, r, m|\mathbf{e}_1 R_1 + \mathbf{e}_2 R_2|g, r, m \mp 1\rangle = \frac{1}{2}\,(\mathbf{e}_1 \pm i\mathbf{e}_2)\,[(r \pm m)(r \mp m + 1)]^{\frac{1}{2}}\,, \tag{1.47}$$

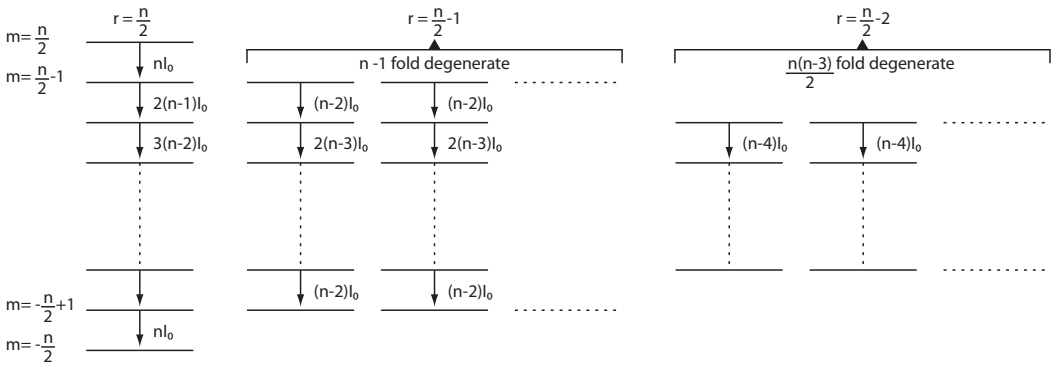

Figure 1.1: Energy level diagram of an n molecule gas, each molecule having 2 nondegenerate energy levels. Spontaneous radiation rates are indicated. $E_m = mE$. As illustrated in Ref. [1]

the spontaneous radiation probabilities can be written as

$$I = I_0(r+m)(r-m+1), \tag{1.48}$$

where the radiation rate of a gas consists of only one molecule in its excited state is $I_0 = \frac{\omega^2}{3c}\left(e_1^2 + e_2^2\right)$, by setting $r = m = \frac{1}{2}$. If all the molecules are excited $m = r = \frac{1}{2}N$, the radiation rate is $I = NI_0$. However, coherent radiation will be emitted for large r, but small $|m|$ values. The largest rate corresponds to

$$r = \tfrac{1}{2}N, \quad m = 0; \quad I = \tfrac{1}{2}N\left(\tfrac{1}{2}N + 1\right)I_0, \tag{1.49}$$

for even number of molecules N. Therefore, this highly coherent strong radiation state is called "*superradiant*" states [38–40]. Although the superradiant states have abnormally large spontaneous radiation rates proportional with N^2, the stimulated emission rate given by

$$(r+m)(r-m+1) - (r+m+1)(r-m) = 2m. \tag{1.50}$$

is normal. The energy level diagram demonstrated by Dicke [1] including the relative magnitudes of the various radiation probabilities is shown in Fig. 1.1.

1.2.3 Tavis-Cummings Model

Almost fifteen years later after Dicke pointed out the importance of treating radiating gas molecules as a single quantum system, in which the molecules are interacting with a common field, and should not be treated as independent, M. Tavis and F. W. Cummings [2] showed some of the exact solutions for a problem of N identical two-level molecules interacting through a dipole coupling with a single-mode quantized radiation field at resonance. They developed approximate expressions for the eigenvectors and eigenvalues for the ground and low-lying excited states, as well as the most highly excited states [50]. These expressions were also compared with exact results. Dicke's results were obtained in first-order perturbation theory, and along the lines many subsequent authors [75–77] have considered other approximations to the N-molecule radiation field problem. However, exact solutions to model problems have historically provided much insight into realistic physical systems, as well as affording a standard of comparison for approximation techniques. Moreover, these exact solutions obtained can be used as a basis set in which the state of a more realistic model may be expanded. For instance, Scully and Lamb [78] described a system of N molecules by a 2×2 matrix, instead of by one of dimension 2^N, and Yu and Eberly [79] showed the entanglement between the two particles coupled with two independent environments became completely vanishing in a finite time along the course of the dynamics of entanglement in bipartite systems. This surprising phenomenon, contrary to intuition based on experience about qubit decoherence, intrigues great interests [80–84]. Therefore the states obtained in Tavis-Cummings model provides a convenient basis for an N-molecule analysis along the similar lines.

In their formulation of the problem, the Hamiltonian which describes the interaction of N-identical two-level systems with a single-mode radiation field is given as:

$$H = R_3 + a^\dagger a - \kappa^* a R_+ - \kappa a^\dagger R_-, \tag{1.51}$$

$$= \quad H_0 - \kappa^* a R_+ - \kappa a^\dagger R_-. \tag{1.52}$$

The N identical two-level systems are assumed to have nonoverlapping space functions and the energy separation of each two-level system (TLS) is equal to the mode frequency of the electromagnetic field. Complex coupling constant divided by the mode frequency is given by $\kappa = |\kappa| e^{-i\phi_1}$. The TLS are coupled to the single-mode radiation field in the dipole approximation and all TLS are assumed to be located at fixed mode positions or to be confined to a container whose dimensions are small compared to the radiation wavelength. The terms which do not conserve energy in the first order perturbation are ignored, since their contribution is very small except for very high intensity fields.

States of the noninteracting system are defined as

$$\begin{aligned}
H_0|n\rangle|r,m\rangle &= (m+n)|n\rangle|r,m\rangle, && (1.53)\\
R_0|r,m\rangle &= \sum_{j=1}^{N} R_{j3}|r,m\rangle = m|r,m\rangle, && (1.54)\\
R_\pm|r,m\rangle &= \sum_{j=1}^{N} R_{j\pm}|r,m\rangle,\\
&= e^{i\phi_2}\left[r(r+1) - m(m\pm 1)\right]^{1/2}|r,m\pm 1\rangle && (1.55)\\
a|n\rangle &= e^{i\phi_3}\sqrt{n}|n-1\rangle. && (1.56)
\end{aligned}$$

Similar to the angular momentum formalism, the eigenstates of H_0 have been chosen to be simultaneous eigenstates of $R^2 = R_3^2 + (R_+R_- + R_-R_+)/2$. The cooperation number r, first defined in Dicke Model, satisfies

$$R^2|r,m\rangle = r(r+1)|r,m\rangle, \tag{1.57}$$

with the condition of $|m| \leq r \leq N/2$, where r and m are either integers or half-integers. The operators defined in Eqs. (1.54-1.56) also satisfy the commutation relations

$$\begin{aligned}
[R_3, R_\pm] &= \pm R_\pm, && (1.58)\\
[R_+, R_-] &= 2R_3, && (1.59)
\end{aligned}$$

$$\left[a, a^{\dagger}\right] \;=\; 1. \tag{1.60}$$

Since both operators R^2 and H_0 commute with the total Hamiltonian H, the eigenstates of H may be chosen to be simultaneous eigenstates of these two operators, and they can be labeled by the cooperation number r and c the eigenvalue of H_0. For any given r and c, $2r+1$ energy eigenvalues will be symmetrically displaced about this constant c, where $-r \leq c < \infty$.

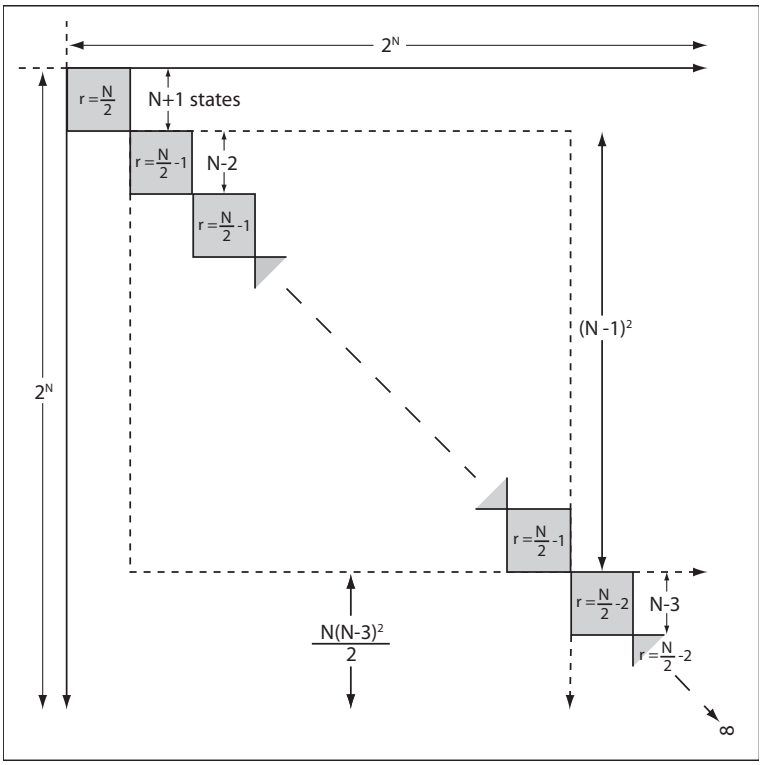

Figure 1.2: Schematic of matrix representation of H. As illustrated in Ref. [2]

The elements $\langle n|\langle r, m|H|r', m'\rangle|n\rangle$ are displayed as a matrix in Fig. 1.2, where there is a grouping into an infinite number of blocks of dimension 2^N along the main diagonal. Each 2^N dimensional block in turn breaks up into smaller blocks along the main diagonal, in which their number and dimension are determined according to the irreducible representations of the group $SU(2)$. Note that only the shaded blocks have

nonzero elements. There are $N!(2r+1)/\left[(N/2+r+1)!(N/2-r)!\right]$ identical blocks for each value of r and each smaller block is of dimension $2r+1$. The values of r range from $N/2$ for the largest single shaded block at the top left-hand corner of the schematic, down to either $r=0$, or $r=1/2$ depending on whether N is even or odd. Also, for a given of r, an integer change in c corresponds to a change to an adjacent block of dimension 2^N. Moreover, the elements of one of the shaded blocks of Fig. 1.2 is also shown for a particular value of r in Fig. 1.3 taken from their paper. The related block has nonzero elements only along the tridiagonal. Assuming the eigenstates of H

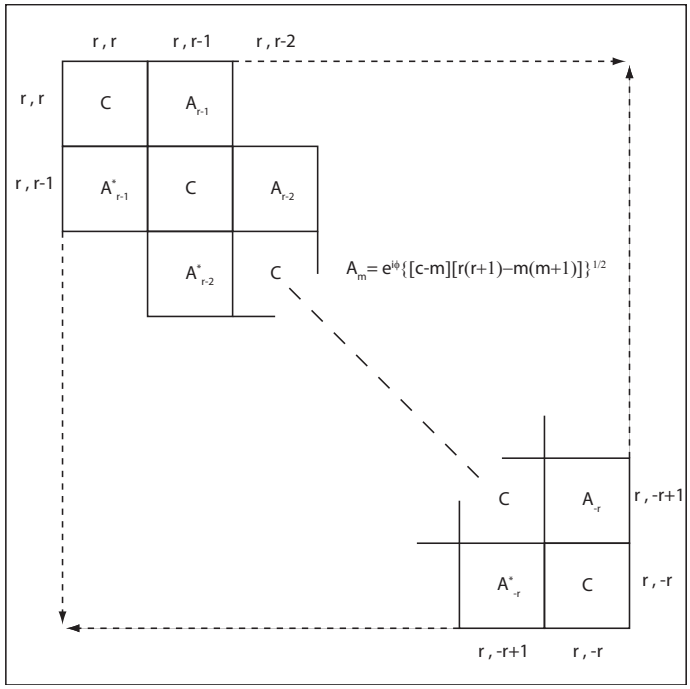

Figure 1.3: Submatrix for given r and c. As illustrated in Ref. [2]

are given as $|r,c,j\rangle$,

$$H|r,c,j\rangle = \lambda_{r,c,j}|r,c,j\rangle, \tag{1.61}$$

where if $c \geq r$, then j takes on $2r+1$ values, i.e. $0,1,2,\ldots,2r$; on the otherhand if $c<r$, then it takes on $c+r+1$ values, i.e. $0,1,\ldots c+r$. Since $|r,c,j\rangle$ are also

eigenstates of H_0 and R^2, and that $m = c - n$ varies between r and $-r$,

$$|r, c, j\rangle = \sum_{n=c-r}^{c+r} A_n^{(r,c,j)} |n\rangle |r, c, j\rangle, \tag{1.62}$$

whereas expressing the total Hamiltonian in terms of $R\pm$ and H_0, given in Eq. (1.52), and using the necessary commutation relations yields to the following difference equation

$$-|\kappa| e^{i\phi} n^{1/2} C_{r,c-n} A_{n-1}^{(r,c,j)} + (c - \lambda_{r,c,j}) - |\kappa| e^{-i\phi} (n+1)^{1/2} C_{r,c-n-1} A_{n+1}^{(r,c,j)} = 0, \tag{1.63}$$

where

$$\phi \equiv \phi_1 + \phi_2 + \phi_3, \tag{1.64}$$

and

$$C_{r,c-n} \equiv [r(r+1) - (c-n)(c-n+1)]^{1/2}. \tag{1.65}$$

The $A_n^{(r,c,j)}$ satisfy the end conditions

$$A_{r+c+1}^{(r,c,j)} = A_{c-r-1}^{(r,c,j)} = 0 \qquad c \geq r, \tag{1.66}$$

and

$$A_{r+c+1}^{(r,c,j)} = A_{-1}^{(r,c,j)} = 0 \qquad c < r. \tag{1.67}$$

It is very useful to define B_n's so that

$$A_n = \frac{(qe^{i\phi})^n B_n}{\sqrt{n!} C_{c-1} C_{c-2} \dots C_{c-n}} \qquad c < r, \tag{1.68}$$

and

$$A_n = \frac{(qe^{i\phi})^n B_n}{\sqrt{n!} C_{r-1} C_{r-2} \dots C_{r-n}} \qquad c \geq r, \tag{1.69}$$

where

$$q = (c - \lambda)/2|\kappa|, \tag{1.70}$$

and the superscripts (c, r, j) have been dropped for simplicity purposes. The effective eigenvalues are given by q in Eq. (1.70), where its maximum value for a given r and c corresponding to the ground state of the system. B_n satisfies the difference equation

$$q^2 B_{n+1} - 2q^2 B_n + n C_{c-n}^2 B_{n-1} = 0. \tag{1.71}$$

The non-normalized exact solution of Eq. (1.71) are

$$\begin{aligned} B_n &= 2^n \textstyle\sum_{l=0}^{n/2} (2q)^{-2l} \mathcal{S}_l^{(n-1)} (-1)^l, & c \le r \\ B_n &= 2^n q^{r-c} \textstyle\sum_{l=0}^{n/2} (2q)^{-2l} \mathcal{S}_l^{(n-1)} (-1)^l, & c > r \end{aligned} \tag{1.72}$$

where the $\mathcal{S}_l^{(n-1)}$ are the sums of all products of $\mathcal{C}_m$'s where $\mathcal{C}_m \equiv m C_{c-m}^2$, l at a time, $\mathcal{C}_{n-1}$ being the maximum and no nearest neighbors are included in the products. Here are some examples

$$\mathcal{S}_3^{(6)} = \mathcal{C}_1\mathcal{C}_3\mathcal{C}_5 + \mathcal{C}_1\mathcal{C}_3\mathcal{C}_6 + \mathcal{C}_1\mathcal{C}_4\mathcal{C}_6 + \mathcal{C}_2\mathcal{C}_4\mathcal{C}_6, \tag{1.73}$$

$$\mathcal{S}_3^{(5)} = \mathcal{C}_1\mathcal{C}_3\mathcal{C}_5, \tag{1.74}$$

$$\mathcal{S}_2^{(4)} = \mathcal{C}_1\mathcal{C}_3 + \mathcal{C}_1\mathcal{C}_4 + \mathcal{C}_2\mathcal{C}_4, \tag{1.75}$$

also $\mathcal{S}_0^{(n)} \equiv 1$ and $\mathcal{S}_l^{(n)} = 0$ if $l > \frac{1}{2}(n+1)$, e.g. $\mathcal{S}_3^{(4)}$. By induction, it can be easily seen that $\mathcal{S}_l^{(n)}$ obey the following recursion relation:

$$\mathcal{S}_l^{(n)} = \mathcal{S}_l^{(n-1)} + \mathcal{C}_n \mathcal{S}_{l-1}^{(n-2)}. \tag{1.76}$$

The exact eigenvalues, or equivalently the eigenvalues q's are determined from the conditions

$$\begin{aligned} B_{r+c+1} &= B_{c-r-1} = 0 & c \ge r \\ B_{r+c+1} &= B_{-1} = 0 & c < r. \end{aligned} \tag{1.77}$$

These are the polynomials in $2q$ of degree $2r+1$ if $c \ge r$ and of degree $r+c+1$ if $c < r$. Note that if r is an integer, they will have a degree $2r$ if $c \ge r$, and $r+c$ if $c < r$. Whenever r is an integer, the solution corresponding to $q = 0$ can be found directly from the equation for A_n and given by

$$\begin{aligned} A_n &= (-1)^{n/2} \mathcal{S}_{n/2}^{(n-1)} / \sqrt{n!} C_{c-1} C_{c-2} \ldots C_{c-n}, & n \text{ even}, 0 \le n \le c+r \\ A_n &= 0, & n \text{ odd}, 0 \le n \le c+r \end{aligned} \tag{1.78}$$

and

$$\begin{aligned} A_n &= (-1)^{(r+n-c)/2}\mathcal{S}^{(n-1)}_{(r+n-c)/2}/\sqrt{n!}C_{r-1}C_{r-2}\ldots C_{c-n}, \qquad n-(c-r) \text{ even}, \\ & \qquad\qquad\qquad\qquad\qquad\qquad\qquad\qquad\qquad\qquad\qquad\qquad c-r \le n \le c+r \\ A_n &= 0, \qquad\qquad\qquad\qquad\qquad\qquad\qquad\qquad\qquad\qquad\qquad\qquad n-(c-r) \text{ odd}, \\ & \qquad\qquad\qquad\qquad\qquad\qquad\qquad\qquad\qquad\qquad\qquad\qquad c-r \le n \le c+r. \end{aligned} \tag{1.79}$$

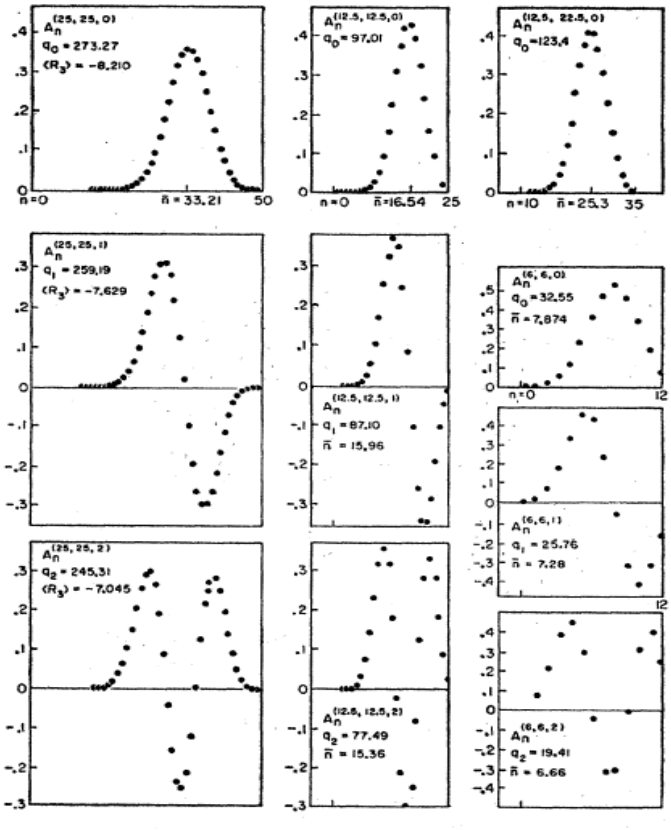

Figure 1.4: Selected eigenvalues $A_n^{(r,c,j)}$. As illustrated in Ref. [2]

The calculated values of $A_n^{(r,c,j)}$ are shown in Fig. 1.4 as a function of n for several values of r,c, and j. The value $j = 0$ corresponds to the ground state, $j = 1$ to the first excited state, and $j = 2r$ to the most highly excited state. The value q_0 corresponds to the ground state and is the largest value of q. The q values are

displaced symmetrically about zero, such that $q_{2r} = -q_0$, $q_{2r-1} = -q_1$, and so on. For integer values of r, the states $A_n^{(j)}$ for $j = 2r, 2r-1, \ldots, r+1$ can be found from the states $A_n^{(j)}$ for $j = 0, 1, \ldots, r-1$ by replacing q by $-q$, or equivalently ϕ by $\phi + \pi$, in Eq. (1.68), and Eq. (1.69). Note that the phase ϕ is assumed to be zero in Fig. 1.4.

1.3 Spin Wave Theory

1.3.1 Direct Exchange Interaction and Magnons

In the previous section, some of the most fundamental models of QED explaining the interaction of light and atomic two-level systems are outlined. In this section, the exchange interaction of spins and the spin waves in ferromagnets (magnons) are examined to achieve a basis for the validity of the macrospin approach used in Section 2.3 and consequently for the comparison of these QED models with the spin-light interaction.

For the sake of simplicity, the development of the spin-spin interaction will be examined for an electron gas embedded in a rigid lattice of positively charged ions starting with the Hartree-Fock approximation [85,86]. The difficulty with this problem lies in the electron-electron interaction terms. In the absence of this interaction, the many-body problem would decouple into one-body problems which simply describe the motion of an electron in a given potential. This very advantageous one-electron approximation can be achieved by the Hartree-Fock approximation while including at least parts of the electron-electron interaction. One can start with the following Hamiltonian:

$$H = -\sum_i \frac{\hbar^2}{2m}\nabla_i^2 + \sum_i V(\boldsymbol{r}_i) + \frac{1}{8\pi\epsilon_0}\sum_{i,j}\frac{e^2}{|\boldsymbol{r}_i - \boldsymbol{r}_j|} = \sum_i H_i + \sum_{i,j} H_{i,j}, \tag{1.80}$$

where the electron-ion interaction H_{el-ion} as $\sum_i V(\boldsymbol{r}_i)$ with $V(\boldsymbol{r}_i) = \sum_i V(\boldsymbol{r}_i - \boldsymbol{R}_i^0)$. There are $N!$ possible ways of distributing N electrons at the N positions $\boldsymbol{r}_1\boldsymbol{r}_2\cdots\boldsymbol{r}_N$. Each possibility is equally likely, because of the indistinguishability of the electrons. Wave functions $\varphi_j(\boldsymbol{q}_i)$ are chosen for the jth electron with coordinates $\boldsymbol{q}_i$, including

spatial coordinates $\boldsymbol{r}_i$ and spin. Therefore, the wavefunction of the electron system can be written with a normalized Slater determinant

$$\Phi = (N!)^{-1/2} \begin{vmatrix} \varphi_1(\boldsymbol{q}_1) & \dots & \varphi_N(\boldsymbol{q}_1) \\ \vdots & & \vdots \\ \vdots & & \vdots \\ \varphi_1(\boldsymbol{q}_N) & \dots & \varphi_N(\boldsymbol{q}_N) \end{vmatrix}, \tag{1.81}$$

in order to satisfy the Pauli principle. If two electrons are interchanged, two columns of the determinant are interchanged and Φ changes sign. Also if two electrons have the same coordinates, two columns are identical and Φ vanishes. Therefore, by using the wavefunction defined in Eq. (1.81), the expectation value of the energy given as $\langle \Phi E \Phi \rangle$ can be calculated as

$$\begin{aligned} E &= \sum_i \int \varphi_i^*(\boldsymbol{q}_1) H_i \varphi_i(\boldsymbol{q}_1) d\tau_1 + \frac{e^2}{8\pi\epsilon_0} \sum_{i,j} \int \frac{|\varphi_i(\boldsymbol{q}_1)|^2 |\varphi_j(\boldsymbol{q}_2)|^2}{|\boldsymbol{r}_1 - \boldsymbol{r}_2|} d\tau_1 d\tau_2 \\ &\quad - \frac{e^2}{8\pi\epsilon_0} \sum_{i,j} \int \frac{\varphi_i^*(\boldsymbol{q}_1)\varphi_i(\boldsymbol{q}_2)\varphi_j^*(\boldsymbol{q}_2)\varphi_j(\boldsymbol{q}_1)}{|\boldsymbol{r}_1 - \boldsymbol{r}_2|} d\tau_1 d\tau_2, \end{aligned} \tag{1.82}$$

where the integration includes a summation over the spins.

The Hartree-Fock electron has a mean kinetic energy proportional to k_F^2 and a mean exchange energy proportional to $-k_F$, assuming the exchange integral itself is positive. Therefore, the energy of spin-compensated ground state is given by $N(ak_F^2 - bk_F)$. If all the spins are parallel, the electron occupy states in a sphere of double the volume in $\boldsymbol{k}$-space. The energy of such a ferromagnetic state becomes $N(a2^{2/3}k_F^2 - b2^{1/3}k_F)$, where the energy lies below the energy of the spin-compensated state if k_F is less than $0.44b/a$. In conclusion, the ferromagnetic state is always favored in an electron gas of low density, because of small Fermi sphere radius. The energy of the ground state is given by Eq. (1.82), where all the electron wavefunctions have the same spin. Therefore, as a direct consequence of spin functions orthogonality, all spin functions can be dropped out of Eq. (1.82), and the coordinates $\boldsymbol{q}_i$ can be replaced by spatial coordinates of electrons $\boldsymbol{r}_i$. An excited state of the system can be obtained by

reversing the spin of one electron. The energy of this excited state is obtained from Eq. (1.82) by associating with $N-1$ electrons the spin function $\alpha(j)$ and with the ith electron the spin function $\beta(i)$. Note that the spin functions are considered in the spinor form:

$$\left| \begin{array}{c} \alpha \\ \beta \end{array} \right\rangle, \tag{1.83}$$

which Pauli matrices operate on. Because of the orthogonality of spin functions, all the exchange integrals connecting this one electron with all other electrons in the system will disappear. The difference in energy between the excited and ground states is

$$E_i - E_0 = \frac{e^2}{8\pi\epsilon_0} \sum_{j \neq i} \int \frac{\varphi_j^*(\boldsymbol{q}_1)\varphi_j(\boldsymbol{q}_2)\varphi_i^*(\boldsymbol{q}_2)\varphi_i(\boldsymbol{q}_1)}{|\boldsymbol{r}_1 - \boldsymbol{r}_2|} d\tau_1 d\tau_2 \equiv \frac{1}{2} \sum_{j \neq i} J_{ij}. \tag{1.84}$$

The excited state $|i\rangle$ is degenerate with all states $|n\rangle$ in which another electron likewise has opposite spin. The solution of the Schrödinger equation for an excited state with this energy can be constructed as a linear combination of all $|n\rangle$, i.e. $\Phi = \sum_n a_n |n\rangle$. This representation is analogous to that of lattice vibrations where kinetic energy fed into one lattice ion spreads itself by Coulomb interaction over all ions. As in the case of phonons, the excitation can be described by wavelike states, $a_n \sim \exp i\boldsymbol{k} \cdot \boldsymbol{r}$, which results with the distribution of the energy needed to reverse a spin throughout the entire spin system in the form of so-called spin waves. Quantization of these spin waves leads to new collective excitations, called magnons.

However, instead of using the Hartree-Fock equations of the free electron gas for this new type of elementary excitation, a more general approach needs to be followed. The spins whose correlation in ferromagnetism leads to a spontaneous magnetic moment are mostly localized on the lattice ions [87]. Moreover, several electrons contribute to the total ion spin. Then the ferromagnetic state is the result of exchange interaction between the total spins of the different ions.

The exchange Hamiltonian can be written in the form of an operator introduced

by Heisenberg,

$$H = -\sum_{i,j} J_{ij} \boldsymbol{S}_i \cdot \boldsymbol{S}_j, \tag{1.85}$$

where J_{ij} is an exchange integral, and the $\boldsymbol{S}_i$ are the vector spin operators of the ith lattice ion. Note that the sum is over all pairs of lattice ions.

For the case $s = 1/2$ the spin operators in Eq. (1.85) are given by the Pauli matrices

$$S_x = \tfrac{1}{2}\begin{bmatrix} 0 & 1 \\ 1 & 0 \end{bmatrix}, \qquad S_y = \tfrac{1}{2}\begin{bmatrix} 0 & -\mathrm{i} \\ \mathrm{i} & 0 \end{bmatrix}, \qquad S_z = \tfrac{1}{2}\begin{bmatrix} 1 & 0 \\ 0 & -1 \end{bmatrix}, \tag{1.86}$$

while satisfying the commutation relations given as $[S_k, S_l] = \mathrm{i}\epsilon_{klm} S_m$, where $k, l, m = x, y, z$.

For the spin functions α, β, defined in the spinor form in Eq. (1.83), operations of Pauli matrices are obtained as:

$$S_z\alpha = \tfrac{1}{2}\alpha, \qquad S_z\beta = -\tfrac{1}{2}\beta, \qquad S^2\alpha = \tfrac{3}{4}\alpha, \qquad S^2\beta = \tfrac{3}{4}\beta, \tag{1.87}$$

where α thus describes the state with $s_z = +1/2$, β the state with $s_z = -1/2$, and the eigenvalue of the operator S^2 is $s(s+1) = 3/4$. Moreover, the corresponding raising and lowering operators defined as $S_+ = S_x + iS_y$ and $S_- = S_x - iS_y$,respectively, have the following relations:

$$S_+\alpha = 0, \qquad S_+\beta = \alpha, \qquad S_-\alpha = \beta, \qquad S_-\beta = 0. \tag{1.88}$$

for the case of $s = 1/2$.

For a total spin $s = n/2$, the spin matrices S_k are $n+1$ dimensional and there are $n+1$ spin functions. The eigenvalues of S_z are $-s, -s+1, \ldots, s-1, s$, and of S^2 are $s(s+1)$.

The expectation value of the exchange energy given in Eq. (1.85) can be obtained as

$$\begin{aligned} E_{\uparrow\uparrow} &= -J_{ij}\langle\alpha_i\alpha_j|\boldsymbol{S}_i \cdot \boldsymbol{S}_j|\alpha_i\alpha_j\rangle = -\frac{1}{4}J_{ij}, \\ E_{\uparrow\downarrow} &= -J_{ij}\langle\alpha_i\beta_j|\boldsymbol{S}_i \cdot \boldsymbol{S}_j|\alpha_i\beta_j\rangle = +\frac{1}{4}J_{ij}. \end{aligned} \tag{1.89}$$

by using the spin operators defined in Eq. (1.86) for $s = 1/2$ and the orthonormalization of the spin functions α and β. The difference between these two possibilities is therefore $J_{ij}/2$, and the difference between a state in which all spins are aligned parallel and one in which the ith spin is reversed is $\sum_{j\neq i} J_{ij}/2$. This agrees with the findings of Eq. (1.84). As a result, the exchange interaction is formally reproduced by the operator in Eq. (1.85) as if it were explicitly a spin-spin interaction.

In Eq. (1.85), only the terms formed by an $\boldsymbol{R}_j = \boldsymbol{R}_i + \boldsymbol{R}_\delta$ will be considered, where the vector to the nearest neighbor of the ith ion is given by $\boldsymbol{R}_\delta$, because the exchange interaction between nearest neighbors is dominant. If it is also further assumed that $J_{i,i+\delta} = J$ for all δ, the effective interaction Hamiltonian becomes

$$H = -J \sum_{i,\delta} \boldsymbol{S}_i \cdot \boldsymbol{S}_{i+\delta}. \tag{1.90}$$

It is clear that the ground state of the electron system corresponds to a configuration in which the ion spins are so aligned that their z-components have the maximum values s. The wave function for the ground state can be described as a product of spin functions $|s\rangle_n$ which represent the spin of the nth ion in state s, i.e. $\Phi_0 = \prod_n |s\rangle_n$. In terms of spin raising and lowering operators, the Hamiltonian in Eq. (1.90) yields

$$H = -J \sum_{ij} \left[S_{iz} S_{jz} + \frac{1}{2} \left(S_{i+} S_{j-} + S_{i-} S_{j+} \right) \right], \qquad \text{where } (j = i + \delta). \tag{1.91}$$

By using this Hamiltonian, the ground state energy can be obtained as

$$E_0 = -s^2 J \sum_{i,i+\delta} 1 = -Js^2 \nu N, \tag{1.92}$$

where the application of spin raising operator to a spin function with maximum spin led to zero and ν is again the number of nearest neighbors of the ion.

Application of the state $\Phi_m = S_{m-} \prod_n |s\rangle_n$, in which the mth spin is reduced by one, to the Hamiltonian given in Eq. (1.91) yields

$$H\Phi_m = -J \sum_{ij} \left[S_{iz} S_{jz} S_{m-} + \frac{1}{2} \left(S_{i+} S_{j-} S_{m-} + S_{i-} S_{j+} S_{m-} \right) \right] \Phi_0. \tag{1.93}$$

Using the commutation relations, $[S_+, S_-] = 2S_z$ and $[S_\mp, S_z] = \pm S_\mp$, the above relation can be further simplified to

$$H\Phi_m = E_0\Phi_m + 2Js\sum_\delta (\Phi_m - \Phi_{m+\delta}). \tag{1.94}$$

From above it is clear that Φ_m is not an eigenstate of the Hamiltonian, and therefore an eigenstate can be rather expanded in terms of all the degenerate states defined as $\Phi_m = S_{m-}\Phi_0$, i.e. $\Phi = \sum_m a_m\Phi_m$. In the view of the translational invariance of the lattice, the a_m have the form $\exp(i\boldsymbol{k}\cdot\boldsymbol{R}_m)$. It then follows that

$$H\Phi = \sum_m \exp(i\boldsymbol{k}\cdot\boldsymbol{R}_m) H\Phi_m = [E_0 + 2J\nu s(1-\gamma_{\boldsymbol{k}})]\Phi, \tag{1.95}$$

where

$$\gamma_{\boldsymbol{k}} = \frac{1}{\nu}\sum_\delta \exp(i\boldsymbol{k}\cdot\boldsymbol{R}_\delta). \tag{1.96}$$

Therefore, the energy of the excited state is

$$E_{\boldsymbol{k}} = E_0 + 2J\nu s(1-\gamma_{\boldsymbol{k}}), \tag{1.97}$$

where the wavevector $\boldsymbol{k}$ is limited to the N values inside a Brillouin zone in $\boldsymbol{k}$-space.

For small $\boldsymbol{k}$, this energy of the excited state becomes

$$E_{\boldsymbol{k}} = E_0 + Js\sum_\delta (\boldsymbol{k}\cdot\boldsymbol{R}_\delta)^2. \tag{1.98}$$

The Eq. (1.97) and Eq. (1.98) are the dispersion relations for spin waves.

Since all spins are aligned parallel in the ground state and their z-components have the maximum value $s_z = s$, an excited state can be described by a number n, which specifies the amount of units that s_z differ from the maximum value. By also adding the index of the ion in question, then each state is described by determining the $n_1, n_2, \ldots, n_N$ in which $n_i = 0, 1, 2, \ldots, 2s$. The excited state can be defined by a state vector $|n_1, n_2, \ldots, n_N\rangle$ for bosons in an occupation number representation. Therefore, in terms of the creation and annihilation operators, the operator $a_j^\dagger a_j$ defines the departures of the spin of the jth ion from the maximum value. By using the following

relations

$$\begin{aligned} S_{j+}|n_j\rangle &= \sqrt{n_j\,(2s+1-n_j)}|n_j-1\rangle \\ S_{j-}|n_j\rangle &= \sqrt{(n_j+1)\,(2s-n_j)}|n_j+1\rangle \\ S_{jz}|n_j\rangle &= (s-n_j)\,|n_j\rangle, \end{aligned} \tag{1.99}$$

where only the state of the jth ion has been given in the wave functions, the spin operators can be expressed in terms of the creation and annihilation operators,

$$S_+ = a\sqrt{2s-a^\dagger a}, \qquad S_- = a^\dagger\sqrt{2s-a^\dagger a}, \qquad S_z = s-a^\dagger a. \tag{1.100}$$

Note that $a_j^\dagger$ and a_j change the spin of the jth ion, and through the exchange interaction this change in spin is propagated through the whole spin system [88]. Therefore, a transformation to creation and annihilation operators of the spin wave quanta which corresponds to the transition from atomic to normal coordinates of lattice vibrations needs to be included. The corresponding transformation is given by

$$a_j^\dagger = \tfrac{1}{\sqrt{N}}\textstyle\sum_{\boldsymbol{k}} \exp\left(i\boldsymbol{k}\cdot\boldsymbol{R}_j\right) b_{\boldsymbol{k}}^\dagger, \qquad a_j = \tfrac{1}{\sqrt{N}}\textstyle\sum_{\boldsymbol{k}} \exp\left(-i\boldsymbol{k}\cdot\boldsymbol{R}_j\right) b_{\boldsymbol{k}}, \tag{1.101}$$

with the commutation relations $[b_{\boldsymbol{k}}, b_{\boldsymbol{k}'}^\dagger] = \delta_{\boldsymbol{k}\boldsymbol{k}'}$, $[b_{\boldsymbol{k}}, b_{\boldsymbol{k}'}] = [b_{\boldsymbol{k}}^\dagger, b_{\boldsymbol{k}'}^\dagger] = 0$, and the relation $\sum_j a_j^\dagger a_j = \sum_{\boldsymbol{k}} b_{\boldsymbol{k}}^\dagger b_{\boldsymbol{k}}$. With this transformation, the Hamiltonian can be presented in terms $b_{\boldsymbol{k}}^\dagger$ and $b_{\boldsymbol{k}}$ which occur under the square root, and hence the expansion of roots has to be inserted into the Hamiltonian. However, one can restrict oneself to small departures from the ground state, since it is the only region where the concept of elementary excitations is reasonable. Therefore, for small n_j, the expansion of the root converges early. Then S_+ is a series with operators of the form $b_{\boldsymbol{k}}, b_{\boldsymbol{k}} b_{\boldsymbol{k}'}^\dagger b_{\boldsymbol{k}''}, \ldots$, whereas S_- is a series with operators $b_{\boldsymbol{k}}^\dagger, b_{\boldsymbol{k}}^\dagger b_{\boldsymbol{k}'}^\dagger b_{\boldsymbol{k}''}, \ldots$. As a result of this, the Hamiltonian for a lattice with a centre of inversion, i.e. $\gamma_{\boldsymbol{k}} = \gamma_{-\boldsymbol{k}}$, can be expanded as

$$\begin{aligned} H &= E_0 + \sum_{\boldsymbol{k}} 2J\nu s\,(1-\gamma_{\boldsymbol{k}})\, b_{\boldsymbol{k}}^\dagger b_{\boldsymbol{k}} \\ &\quad + \frac{\nu J}{2N}\sum_{\boldsymbol{k},\boldsymbol{k}',\boldsymbol{\kappa}} \left(\gamma_{\boldsymbol{k}-\boldsymbol{\kappa}} + \gamma_{\boldsymbol{k}'} - 2\gamma_{\boldsymbol{k}-\boldsymbol{\kappa}-\boldsymbol{k}'}\right) b_{\boldsymbol{k}-\boldsymbol{\kappa}}^\dagger b_{\boldsymbol{k}'+\boldsymbol{\kappa}}^\dagger b_{\boldsymbol{k}'} b_{\boldsymbol{k}} + \cdots, \end{aligned} \tag{1.102}$$

where $\gamma_{\boldsymbol{k}}$ is given by Eq. (1.96). The above approach consisting of rewriting the Hamiltonian in terms of creation, annihilation operators, and the expansion of the roots are called *Holstein-Primakoff approximation* [89].

The first term is the energy of the ground state, the second is the energy contained in the magnons, which can be expressed as

$$\hbar\omega_{\boldsymbol{k}} = 2J\nu s\left(1-\gamma_{\boldsymbol{k}}\right), \tag{1.103}$$

whereas $b^{\dagger}_{\boldsymbol{k}} b_{\boldsymbol{k}}$ is the magnon number operator. The other terms in Eq. (1.102) describe the magnon-magnon interaction [90]. The third term in particular contains processes in which two magnons $\boldsymbol{k}$,$\boldsymbol{k}'$ are annihilated and two magnons $\boldsymbol{k}-\boldsymbol{\kappa}$, $\boldsymbol{k}'+\boldsymbol{\kappa}$ created throughout the processes in which momentum $\boldsymbol{\kappa}$ is transferred from one magnon to another while conserving the total momentum. Note that this term also contains processes in which $\boldsymbol{\kappa}=0$ or $\boldsymbol{k}'=\boldsymbol{k}-\boldsymbol{\kappa}$. Such terms contribute to the magnon energy given in Eq. (1.103) and can be interpreted as renormalization of the magnon energy through exchange interaction.

For the isotropic case $\hbar\omega_k \sim k^2$, the energy contained in the magnons can be estimated as

$$\begin{aligned} E = \sum_{\boldsymbol{k}} \frac{\hbar\omega_{\boldsymbol{k}}}{\exp\left(\hbar\omega_{\boldsymbol{k}}/k_B T\right)-1} &\propto \int d\tau_{\boldsymbol{k}} \frac{k^2}{\exp\left(\alpha k^2/T\right)-1} \\ &\propto \int_0^{k_{max}} dk \frac{k^4}{\exp\left(\alpha k^2/T\right)-1}, \end{aligned} \tag{1.104}$$

where the summation in $\boldsymbol{k}$-space is replaced by an integral. The upper limit k_{max} of the magnon dispersion spectrum in Eq. (1.104) can be replaced with infinity, because the estimate is only valid for low temperature where only few magnons are excited. Therefore, the temperature dependence of the energy is obtained to be proportional with $T^{3/2}$.

Moreover, the differentiation of the magnetization from the saturation value given as $\Delta M = M(T)-M(0)$ is proportional to the average number of magnons $\sum_{\boldsymbol{k}} \bar{n}_{\boldsymbol{k}}$. Hence, as it can be seen from Eq. (1.104) that it is proportional to an integral with k^2

in the numerator of the integrand, the temperature dependence of the magnetization also leads to a $T^{3/2}$ law [91]. The range of validity is limited most of all by the magnon-magnon interaction and by the assumption that Eq. (1.98) is mainly restricted the isotropic k^2-law. The concept of elementary excitation is only useful for the case that mutual interactions between the excitations are negligible.

1.3.2 Ferromagnetic Resonance

As in the case of nuclear magnetic resonance, the precession in a constant magnetic field of the magnetic moment associated with ferromagnetism resonates with a varying external magnetic field when its frequency is equal to that of the precession. This ferromagnetic resonance absorption was first observed by Griffith [92].

In ferromagnetic material, there exists a certain internal magnetic field which accompanies the magnetization of the substance. This internal magnetic field is called the demagnetization field and is denoted by $\boldsymbol{B}^i$. The demagnetization field is the result of the fields of the dipoles induced at each interior point of the ferromagnet. The components of the internal magnetic field $\boldsymbol{B}^i$ are related to the applied field by

$$B_x^i = B_x^0 - N_x M_x, \qquad B_y^i = B_y^0 - N_y M_y, \qquad B_z^i = B_z^0 - N_z M_z. \tag{1.105}$$

The Lorentz field $(4\pi/3)\boldsymbol{M}$ and exchange field $\lambda \boldsymbol{M}$ do not contribute to the torque in the spin equation of motion $\dot{M} = \gamma(\boldsymbol{M} \times \boldsymbol{B}^i)$. For an applied magnetic field along the $\boldsymbol{z} - axis$, the equation of motion becomes

$$\begin{aligned} \frac{dM_x}{dt} &= \gamma(M_y B_z^i - M_z B_y^i) = \gamma\left[B_0 + (N_y - N_z)M_z\right] M_y, \\ \frac{dM_y}{dt} &= \gamma(M_z B_x^i - M_x B_z^i) = -\gamma\left[B_0 + (N_x - N_z)M_z\right] M_x, \end{aligned} \tag{1.106}$$

where to first order dM_z/dt is set to zero. Solutions with time dependence $\exp(-i\omega t)$ can be obtained from

$$\begin{vmatrix} i\omega & \gamma\left[B_0 + (N_y - N_z)M\right] \\ -\gamma\left[B_0 + (N_x - N_z)\right] & i\omega \end{vmatrix} = 0, \tag{1.107}$$

where $M_z = M$. Therefore, the ferromagnetic resonance frequency ω_0 of the uniform mode in the applied field B_0 is given by

$$\omega_0^2 = \gamma^2 \left[B_0 + (N_y - N_z)M\right] \left[B_0 + (N_x - N_z)M\right]. \tag{1.108}$$

In this uniform mode, all the moments precess together in phase with the same amplitude. For a sphere $N_x = N_y = N_z$, hence very sharp resonance line with a resonance frequency of $\omega_0 = \gamma B_0$ can be achieved [93, 94]. Note that shape of the specimen plays an important role, because of large demagnetization fields of ferromagnets. Moreover, the strong exchange coupling between the ferromagnetic electrons supresses the dipolar contribution to the line width, so that the ferromagnetic resonance lines are quite sharp. Different than nuclear magnetic resonance, it is not possible to drive a ferromagnetic spin system upto a point where the magnetization M_z is reduced to zero or reversed. Because, the ferromagnetic resonance excitation breaks down into spin waves before the magnetization can be rotated appreciably from its initial direction.

1.4 Spin Torque Nano Oscillators

Spin-polarized current in a magnetic conductor can alter its magnetization, due to a purely quantum mechanical transfer of angular momentum from the charge carriers to the magnetization. This effect, which first predicted by J. Slonczewski [45] and L. Berger [44] independently, offers the possibility of manipulating magnetic-device elements without external cumbersome magnetic fields [95]. However, first predictions indicated the requirement of current densities on the order of 10^8 amperes per square centimetre to generate sufficient torque to overcome the intrinsic viscous damping. Fortunately, the electron transport properties of nanometre sized conducting magnetic heterostructures revealed the possibility of seeing such a phenomenon [46, 96–103].

Spin torque can be used to manipulate magnetic orientation [46, 104] and to cause the magnetization to precess [43, 47, 105] at microwave frequencies. The latter

can be used to develop a spin-based analogue of the voltage-controlled oscillator [106, 107] and holds great promise for microchips [108], where the limited bandwidth of the interconnects between components is starting to constrain device performance. However, in past, the advantages of having a microwave emitting oscillator with a size of only a few hundred nanometres in dimension were greatly outweighed by the need to incorporate a large source of external magnetic field. Recent progress [109, 110] in the area shows the possibility of generating microwave signals in spin-torque nano-oscillators (STNOs) without applying any external magnetic field. Moreover, recent results [111] demonstrate the emission of relatively large and narrowband radiofrequency signals of several hundred Mhz from STNOs in zero applied field. Therefore, zero-field signal emissions can be pushed into the GHz regime by confining the entire device to a nanopillar geometry that is only several hundred nanometres in size [112] and also by phase-locking several nano-oscillators together [113, 114].

In this section, one of the approaches [44] for the emission of spin waves by a magnetic multilayer traversed by a current is summarized. In metallic ferromagnets, the s-d exchange interaction between the spins $\boldsymbol{s}$ of $4s$ conduction electrons and the spins $\boldsymbol{S}(\boldsymbol{r})$ of $3d$ magnetic electrons is given by

$$\begin{aligned} V_{sd} &= g\mu_B \boldsymbol{s} \cdot \boldsymbol{H}_{sd}(\boldsymbol{r}), \\ \boldsymbol{H}_{sd}(\boldsymbol{r}) &= -\frac{2J_{sd}\langle \boldsymbol{S}(\boldsymbol{r})\rangle}{g\mu_B}, \end{aligned} \tag{1.109}$$

where g is the gyromagnetic ratio and μ_B is the Bohr magneton. J_{sd} corresponds to the s-d exchange integral, whereas the intra-atomic s-d exchange field acting on s is given by $\boldsymbol{H}_{sd}(\boldsymbol{r})$.

Large electron-magnon coupling existing at an interface between normal and ferromagnetic layers can be obtained even without localized spin-wave modes. Even though the electrons have conveniently long time to adapt to the existing spin wave at minimal energy cost in the bulk, an electron entering a ferromagnet through a sharp

interface does not have this opportunity. In addition, an emission of coherent spin waves are predicted when the interface is traversed by a dc current.

1.4.1 Spin Torque from a Single Electron at an Interface

Two ferromagnetic layers F_1, F_2 are separated by a normal layer N, in the case where the magnetic spins $\boldsymbol{S}_1$, $\boldsymbol{S}_2$ in F_1, F_2 are at an oblique angle θ. In N, a frame of (x, y, z) is defined in a way that x is normal to the N-F_2 interface and z parallel to $\boldsymbol{S}_1$. The origin of x lies at the N-F_2 interface. $\boldsymbol{S}_1$ and $\boldsymbol{S}_2$ are assumed uniform over F_1 and F_2. The wavefunction of the conduction electron injected from F_1 into N, with expectation $\langle \boldsymbol{s} \rangle$ parallel to z, is given by

$$\psi = \left[e^{ik_x^N x} \left| \begin{array}{c} A \\ 0 \end{array} \right| + e^{-ik_x^N x} \left| \begin{array}{c} B \\ C \end{array} \right| \right] e^{i(k_y^N y + k_z^N z)}, \tag{1.110}$$

where B, C are the spin-up and spin-down amplitudes in N caused by reflection at the N-F_2 interface, and $\boldsymbol{k}^N$ is the wavevector in N.

In the interface F_2, the same frame (x, y, z) can be used to describe the spatial motion of the electron. Arbitrary direction of $\boldsymbol{S}_2$ is given by the polar angles (θ, ϕ) in the (x, y, z) frame. The wavefunction for the transmitted electron into F_2 is

$$\psi = De^{i\boldsymbol{k}_\uparrow \cdot \boldsymbol{r}} \left| \begin{array}{c} e^{-i\varphi/2} \cos(\theta/2) \\ e^{i\varphi/2} \sin(\theta/2) \end{array} \right| + Ee^{i\boldsymbol{k}_\downarrow \cdot \boldsymbol{r}} \left| \begin{array}{c} -e^{-i\varphi/2} \sin(\theta/2) \\ e^{i\varphi/2} \cos(\theta/2) \end{array} \right|. \tag{1.111}$$

Two spin states correspond to $\langle \boldsymbol{s} \rangle$ parallel and anti-parallel to $\boldsymbol{S}_2$, respectively, whereas $\boldsymbol{k}_\uparrow$ and $\boldsymbol{k}_\downarrow$ are the spin-up and spin-down wavevectors. Moreover, D and E are the spin-up and spin-down electron amplitudes, in a frame (x_2, y_2, z_2) with z_2 parallel to $\boldsymbol{S}_2$ and x_2 in the $(\boldsymbol{S}_2, z)$ plane. Continuity of ψ and $d\psi/dx$ at $x = 0$ leads to

$$D = 2Ae^{i\varphi/2} \cos(\theta/2)/(1 + k_x^\uparrow/k_x^N), \tag{1.112}$$

$$E = -2Ae^{i\varphi/2} \sin(\theta/2)/(1 + k_x^\downarrow/k_x^N). \tag{1.113}$$

At a distance $x_0 > 0$ from the N-F_2 interface, the local expectation of the spin

components of a single electron along the x_2 and y_2 axes is

$$\begin{aligned}
\langle s_{x2}\delta(\boldsymbol{r}-\boldsymbol{r}_0)\rangle &= \mathrm{Re}\left[\mathrm{e}^{\mathrm{i}(\mathrm{k}_\mathrm{x}^\uparrow-\mathrm{k}_\mathrm{x}^\downarrow)}\mathrm{E}^*\mathrm{D}\right] \\
&= -2|A|^2\frac{f(x_0)\sin\theta}{(1+k_x^\uparrow/k_x^N)(1+k_x^\downarrow/k_x^N)}\times\cos\left[(k_x^\uparrow-k_x^\downarrow)x_0\right], \\
\langle s_{y2}\delta(\boldsymbol{r}-\boldsymbol{r}_0)\rangle &= \mathrm{Re}\left[\mathrm{e}^{\mathrm{i}(\mathrm{k}_\mathrm{x}^\uparrow-\mathrm{k}_\mathrm{x}^\downarrow)}\mathrm{E}^*\mathrm{D}\right] \\
&= 2|A|^2\frac{f(x_0)\sin\theta}{(1+k_x^\uparrow/k_x^N)(1+k_x^\downarrow/k_x^N)}\times\sin\left[(k_x^\uparrow-k_x^\downarrow)x_0\right]. \quad (1.114)
\end{aligned}$$

At $x_0=0$, $\langle \boldsymbol{s}\cdot\delta(\boldsymbol{r}-\boldsymbol{r}_0)\rangle$ is parallel to the (z_2,x_2) plane. Local $\langle\boldsymbol{s}\rangle$ components along x_2 and y_2 have spatial oscillations with a wavelength of $2\pi/|k_x^\uparrow-k_x^\downarrow|$, because of the electron spin precession around the $s-d$ exchange field $\boldsymbol{H}_sd$ along the motion in F_2 away from the N-F_2 interface.

Multiplying the first and second terms of Eq.(1.111) by introduced damping factors $\exp(-k_\uparrow x_0/\Lambda_\uparrow k_x^\uparrow)$ and $\exp(-k_\downarrow x_0/\Lambda_\downarrow k_x^\downarrow)$, respectively, simulates the effect of electron scattering on ψ, caused by solute atoms and phonons in F_2. Spin-up and down mean free paths in F_2 are given by $\Lambda_\uparrow$ and $\Lambda_\downarrow$. This leads to the existence of the correction factor $f(x_0)$ already introduced in Eq. (1.114),

$$f(x_0)=\exp\left[-\left(\frac{k_\uparrow}{\Lambda_\uparrow k_x^\uparrow}+\frac{k_\downarrow}{\Lambda_\downarrow k_x^\downarrow}\right)x_0\right]. \quad (1.115)$$

The effect of this factor is to attenuate the density $\langle s_{x2}\delta(\boldsymbol{r}-\boldsymbol{r}_0)\rangle$ strongly at distances x_0 from the interface larger than $\Lambda_\uparrow$ or $\Lambda_\downarrow$.

By combining Eq. (1.114) and Eq. (1.115), from the exchange torque exerted by $\boldsymbol{H}_{sd}$, the rate of change of $\langle s_{x2}\rangle$ can be calculated as

$$\begin{aligned}
\hbar\frac{d\langle s_{x2}\rangle}{dt} &= -g\mu_B\langle s_{y2}\rangle {H_{sd}^z}^2 \\
&= -g\mu_B {H_{sd}^z}^2\int\int\int_{x=0}^{x=\infty}\langle s_{y2}\delta(\boldsymbol{r}-\boldsymbol{r}_0)\rangle \\
&= -g\mu_B {H_{sd}^z}^2 L_yL_z2|A|^2\frac{\sin\theta}{(1+k_x^\uparrow/k_x^N)(1+k_x^\downarrow/k_x^N)}\frac{1}{k_x^\uparrow-k_x^\downarrow}, \quad (1.116)
\end{aligned}$$

where the sample dimensions along y and z are given by L_y and L_z, and the mean free paths of spin-up and spin-down are assumed to be $\Lambda_\uparrow,\Lambda_\downarrow \gg 1/|k_x^\uparrow-k_x^\downarrow|$. As

it can be seen from Eq. (1.116), only a region of F_2 of thickness $\simeq 1/|k_x^{\uparrow} - k_x^{\downarrow}|$ contributes appreciably to the total torque on the electron spin. Similarly, in the same frame (x_2, y_2, z_2), the rate of change of other components are obtained as $d\langle s_{y2}\rangle/dt \simeq d\langle s_{z2}\rangle/dt \simeq 0$. Therefore, the vector $d\langle \boldsymbol{s}\rangle/dt$ is shown to be parallel to the x_2 axis and has the effect of bringing $\langle \boldsymbol{s}\rangle$ closer to $\boldsymbol{S}_2$ direction. By using the relation $(\hbar^2/2m)\left(k_x^{\uparrow 2} - k_x^{\downarrow 2}\right) = -2\mu_B {H_{sd}^z}^2$, while setting $g = 2$, Eq. (1.116) can be simplified as

$$\left|\frac{d\langle \boldsymbol{s}\rangle}{dt}\right| = L_y L_z |A|^2 \frac{\left|v_x^{\uparrow} + v_x^{\downarrow}\right|}{(1 + k_x^{\uparrow}/k_x^N)(1 + k_x^{\downarrow}/k_x^N)} \left|\sin\theta\right|, \tag{1.117}$$

in terms of the Fermi velocities in F_2 of spin-up $\boldsymbol{v}_{\uparrow}$, and spin-down $\boldsymbol{v}_{\downarrow}$ electron. Normalization of volume V_N located in N and also including the N-F_2 interface gives $|A|^2 = 1/V_N$.

1.4.2 Spin-Flip and Spin-Wave Relaxation Time

If the original frame (x, y, z) is used in connection with spin waves, the projection of the vector $d\langle \boldsymbol{s}\rangle/dt$ on fixed z axis is given by

$$\frac{d\langle s_z\rangle}{dt} = -\left|\frac{d\langle \boldsymbol{s}\rangle}{dt}\right| \sin\theta. \tag{1.118}$$

For the average $\langle s_z\rangle$ to change in time, the electron should flip its spin along z; because a spin component s_z is only allowed to have measured values of $\pm 1/2$. The total spin-flip rate from up($\uparrow$) to down($\downarrow$) is

$$\frac{dn_{\uparrow\downarrow}}{dt} = -\frac{d\langle s_z\rangle}{dt} \Delta n_{\uparrow}, \tag{1.119}$$

where $\Delta n_{\uparrow}$ corresponds to the total number of spin-up electrons present on a Fermi surface element dS in N. Electron spin-flip time $\tau_{\uparrow\downarrow}$ is defined as

$$\frac{dn_{\uparrow\downarrow}}{dt} = \frac{\Delta n_{\uparrow}}{\tau_{\uparrow\downarrow}}, \tag{1.120}$$

over the Fermi surface dS. Combination of Eqs. (1.118)-(1.120) yields to the spin-flip time of

$$\frac{1}{\tau_{\uparrow\downarrow}} = L_y L_z |A|^2 \frac{v_x^{\uparrow} + v_x^{\downarrow}}{(1 + k_x^{\uparrow}/k_x^N)(1 + k_x^{\downarrow}/k_x^N)} \sin^2\theta. \tag{1.121}$$

If a more realistic situation in which electrons of both spins enter F_2 is considered, the energies involved in the transition are connected to each other through the energy conservation,

$$\varepsilon_{\downarrow} - \varepsilon_{\uparrow} = \hbar\omega. \tag{1.122}$$

The energy quanta (magnon) of a spin wave of angular frequency ω is given as $\hbar\omega$. Due to the precession of the localized spins $\boldsymbol{S}_2$ clockwise around the fixed axis z at a rate of $\omega = -d\phi/dt$, a spin-wave is formed in F_2. Note that the spin-wave wavelength is assumed to be very large in order to achieve a uniform precession present in ferromagnetic resonance. In order to achieve magnons, the $\boldsymbol{S}_2$ needs to be treated quantum mechanically. Conservation of the total angular momentum along z, the electron should flip from $\uparrow$ to $\downarrow$ as a magnon is annihilated, and vice versa, leading to the relation $\varepsilon_{\downarrow} > \varepsilon_{\uparrow}$ between energies of different spins. If n_m is the total number of magnons in F_2, the rate of change of magnons is

$$\frac{dn_m}{dt} = -\frac{dn_{\uparrow\downarrow}}{dt}. \tag{1.123}$$

in terms of the total spin-flip rate. Therefore, by using Eq. (1.120), the rate of spin-flip is obtained as

$$\begin{aligned} \frac{dn_{\uparrow\downarrow}}{dt} &= \int_{-\infty}^{+\infty} d\varepsilon_{\uparrow} \frac{D_{\uparrow}}{2\overline{\tau}_{\uparrow\downarrow}} f_{\uparrow}(\varepsilon_{\uparrow}) \left[1 - f_{\downarrow}(\varepsilon_{\uparrow} + \hbar\omega)\right] \\ &\quad - \int_{-\infty}^{+\infty} d\varepsilon_{\downarrow} \frac{D_{\downarrow}}{2\overline{\tau}_{\uparrow\downarrow}} f_{\downarrow}(\varepsilon_{\downarrow}) \left[1 - f_{\uparrow}(\varepsilon_{\downarrow} - \hbar\omega)\right], \end{aligned} \tag{1.124}$$

where $1/\overline{\tau}_{\uparrow\downarrow}$ is the average of spin-flip time over the active half of the Fermi surface, with $k_x^N > 0$, in N. The N densities of states, and the average occupation numbers for spin-up and spin-down are given by $D_{\uparrow} = D_{\downarrow} = D_N/2$, and $f_{\uparrow}$,$f_{\downarrow}$, respectively, while the factors $(1 - f_{\uparrow})$ and $(1 - f_{\downarrow})$ correspond to the exclusion principle for the final states.

A possible shift of $\Delta\mu_\uparrow$ and $\Delta\mu_\downarrow$ in the spin-up and spin-down Fermi levels from their equilibrium value μ_0 is introduced. If f_0 is the Fermi function at temperature T, then the new average occupation numbers become

$$\begin{aligned} f_\uparrow(\varepsilon_\uparrow) &= f_0(\varepsilon_\uparrow - \mu_0 - \Delta\mu_\uparrow), \\ f_\downarrow(\varepsilon_\downarrow) &= f_0(\varepsilon_\downarrow - \mu_0 - \Delta\mu_\downarrow). \end{aligned} \tag{1.125}$$

Therefore, even at finite temperatures, Eq. (1.124) can be rewritten as

$$\frac{dn_{\uparrow\downarrow}}{dt} = \frac{D_N}{4\overline{\tau}_{\uparrow\downarrow}}(\Delta\mu + \hbar\omega), \tag{1.126}$$

where the net shift is expressed with $\Delta\mu = \Delta\mu_\uparrow - \Delta\mu_\downarrow$. Each magnon has an angular momentum of $-\hbar$ along z, so that if $\theta \ll 1$, the number of magnons

$$n_m = S_2(1 - \cos\theta)n_2 \simeq (S_2 n_2 \sin^2\theta)/2, \tag{1.127}$$

where S_2 is the magnitude of $\boldsymbol{S}_2$ and n_2 the number of atoms in F_2. Therefore, combining Eqs. (1.121),(1.123),(1.126), and (1.127) yields to the following spin-wave relaxation time, τ_m:

$$\begin{aligned} \frac{1}{\tau_m} &= -\frac{dn_m}{n_m dt} \\ &= \frac{D_N V_2}{V_N n_2}\frac{\Delta\mu + \hbar\omega}{2L_2^x S_2} \times \left[\overline{\frac{\varepsilon_x^\uparrow + \varepsilon_x^\downarrow}{(1 + k_x^\uparrow/k_x^N)(1 + k_x^\downarrow/k_x^N)}} \right], \end{aligned} \tag{1.128}$$

where $V_2 = L_2^x L_y L_z$ is the volume of F_2 and L_2^x is the thickness of F_2 along x. Since the enhanced electron-magnon scattering is a surface effect, L_2^x in the denominator controls the validity of Eq. (1.128) with the condition $L_2^x \gg \Lambda_\uparrow, \Lambda_\downarrow$. τ_m is related to the ferromagnetic resonance linewidth ΔH by $\gamma\Delta H \simeq 1/\tau_m$. Note that as it will be clear in the next section, $\Delta\mu + \hbar\omega$ may become negative in Eq. (1.128) leading to negative $1/\tau_m$. Hence, dn_m/dt is positive and proportional to n_m, reflecting stimulated emission of spin waves. There is no spontaneous emission, because there are no quantum fluctuations introduced in $\boldsymbol{S}_2$ formalism.

1.4.3 Stimulated Emission of Spin Waves

If an electric current with spin-up and down densities $j_x^{\uparrow}$, $j_x^{\downarrow}$ is injected across the N-F_2 interface, the Fermi surfaces in N are shifted by amounts $\Delta k_x^{\uparrow}$ and $\Delta k_x^{\downarrow}$ along x in k space, given by

$$\Delta k_x^{\uparrow} = -\frac{2j_x^{\uparrow} m}{e n_e^N \hbar}; \quad \Delta k_x^{\downarrow} = -\frac{2j_x^{\downarrow} m}{e n_e^N \hbar}; \tag{1.129}$$

where n_e^N is the total number of electrons per unit volume in N and e, m are the electron charge and mass, respectively. Shifts $\Delta\mu_{\uparrow}$, $\Delta\mu_{\downarrow}$ of the local Fermi level at a given point of the Fermi surface are

$$\Delta\mu_{\uparrow} = \hbar \Delta k_x^{\uparrow} \varepsilon_x^N; \quad \Delta\mu_{\downarrow} = \hbar \Delta k_x^{\downarrow} \varepsilon_x^N, \tag{1.130}$$

where the Fermi velocity in N is given by $\boldsymbol{\varepsilon}_N$. N is assumed to be much thinner than a spin-diffusion length, so that $j_x^{\uparrow}$ and $j_x^{\downarrow}$ are the same in N as in F_1 and in F_2, where their ratio is $\alpha_1 = j_x^{\uparrow}/j_x^{\downarrow} = \sigma_1^{\uparrow}/\sigma_1^{\downarrow}$. The spin-up and down conductivities in F_1 are given by $\sigma_1^{\uparrow}$, $\sigma_1^{\downarrow}$ far from any interface. Total current density $j_x = j_x^{\uparrow} + j_x^{\downarrow}$, and the Fermi wave vector $\boldsymbol{k}_N$ in N are used to obtain

$$\Delta\mu = \Delta\mu_{\uparrow} - \Delta\mu_{\downarrow} = -2\left(\frac{\alpha_1 - 1}{\alpha_1 + 1}\right) j_x \frac{\hbar k_x^N}{e n_e^N}. \tag{1.131}$$

For the material properties of copper, $n_e^N = 8.5 \times 10^{28}$ m^{-3} and $k_x^N \leq k_N = 1.36 \times 10^{10}$ m^{-1}, with $\alpha_1 \gg 1$, current densities of $j_x = 10^{11}$ A/m^2 achievable in dc or with current pulses, $\Delta\mu = -1.31 \times 10^{-4}$ eV. It can also be easily seen from the above equation that the critical current density is proportional to ω, when spin-wave emission starts with the requirement $\Delta\mu + \hbar\omega = 0$. Therefore, low-frequency spin waves are easiest to excite.

CHAPTER 2
SPIN-CAVITY HAMILTONIAN

In this thesis, we suggest a new physical realization of a CQED system based on the interaction of N spins confined into a very small nanomagnet, rather than atomic systems in the usual sense, with an electromagnetic field inside the cavity. The schematic of our system is shown in Fig. 2.1. The cavity is tuned to be resonant with the energy level spacings of the spins acting as two-level systems. Since the dimensions of the nanomagnet is considered to be very small compared with the wavelength of the field, individual spins will be combined into a single quantum system by introducing the collective spin operators. A constant uniform magnetic field is applied along the **z**-axis of the cavity, causing the precession of the collective spin of the nanomagnet. In the presence of this precession motion, the spin system coherently exchanges energy back and forth with a single mode of the cavity field. Moreover, due to this feedback effect of the cavity field, individual spin flips give rise to an overall change of the collective spin of the system over time. Even though these spin-field interactions are magnetic in nature and generally very small compared to the atom-field interactions, by considering the fact that a typical spherical nanomagnet with a small radius of 100 nm has roughly 10^9 spins, these interactions are predicted to be strong enough to play an important role in quantum computation and spintronics.

In this chapter, nanomagnet-microwave coupling Hamiltonian will be derived starting from the very basic definitions of the Maxwell-field by further introducing the second-quantization of the spherical waves in the presence of a source of magnetization. Transverse-magnetic (TM) and transverse-electric (TE) modes of the cavity field will be seperately demonstrated in a fully quantum treatment by using the suitable algebra

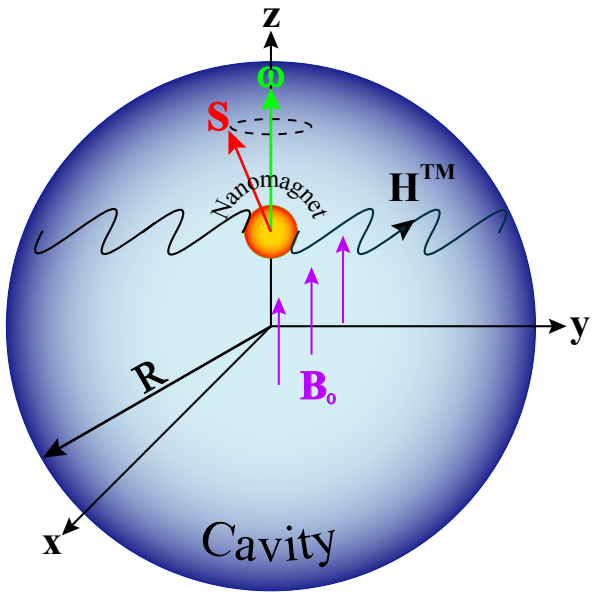

Figure 2.1: Schematic of our nanomagnet-microcavity system consists of a spherical nanomagnet of radius 100 nm placed at a distance of d from the center of a microcavity of radius R. A uniform magnetic field, $\boldsymbol{B}$, is applied along the **z**-axis causing the precession of the total nanomagnet spin, $\boldsymbol{S}$, with frequency of ω.

of vector spherical harmonics.

2.1 Spherical Wave Expansion of the Cavity Field in the presence of Intrinsic Magnetization

Since the total magnetization of the nanomagnet can be treated as a single local source, the only tool we have in hand to examine the cavity field is the following Maxwell equations given by

$$\begin{aligned} \boldsymbol{\nabla}\cdot\boldsymbol{H} &= 0, & \boldsymbol{\nabla}\times\boldsymbol{E} - ikZ_0\boldsymbol{H} &= 0, \\ \boldsymbol{\nabla}\cdot\boldsymbol{E} &= 0, & \boldsymbol{\nabla}\times\boldsymbol{H} + ik\boldsymbol{E}/Z_0 &= \boldsymbol{\nabla}\times\boldsymbol{M}, \end{aligned} \tag{2.1}$$

in the presence of a local source, where Z_0 is defined as $\sqrt{\mu_0/\epsilon_0}$. Note that the corresponding current density can be interpreted as $\boldsymbol{J} = \boldsymbol{\nabla}\times\boldsymbol{M}$ for a given intrinsic magnetization. Since the time dependence of the fields and the magnetization in Eq. (2.1) can be introduced by $e^{-i\omega t}$, the corresponding Helmholtz wave equations for

magnetic field $\boldsymbol{H}$ and electric field $\boldsymbol{E}$ are obtained as

$$\left(\nabla^2 + k^2\right)\boldsymbol{H} = -\boldsymbol{\nabla}\times(\boldsymbol{\nabla}\times\boldsymbol{M}), \tag{2.2}$$

$$\left(\nabla^2 + k^2\right)\boldsymbol{E} = -iZ_0 k\boldsymbol{\nabla}\times\boldsymbol{M}. \tag{2.3}$$

Similar to Bouwkamp and Casimir's trick published in 1954, The spherically symmetric treatment of the cavity becomes trivial by replacing the magnetic field $\boldsymbol{H}$ and electric field $\boldsymbol{E}$ with $(\boldsymbol{r}\cdot\boldsymbol{H})$ and $(\boldsymbol{r}\cdot\boldsymbol{E})$ in the above Helmholtz equations Eq. (2.2) and Eq. (2.3):

$$\left(\nabla^2 + k^2\right)(\boldsymbol{r}\cdot\boldsymbol{H}) = -i\boldsymbol{L}\cdot(\boldsymbol{\nabla}\times\boldsymbol{M}), \tag{2.4}$$

$$\left(\nabla^2 + k^2\right)(\boldsymbol{r}\cdot\boldsymbol{E}) = Z_0 k\boldsymbol{L}\cdot\boldsymbol{M}. \tag{2.5}$$

The solutions to the above equations yield to two distinct solution sets expressed as transverse magnetic (TM) and transverse electric (TE) modes. Hence, TM mode solutions are defined as

$$\begin{aligned}\boldsymbol{r}\cdot\boldsymbol{H}^{(TM)} &= 0,\\ \boldsymbol{r}\cdot\boldsymbol{E}^{(TM)} &= -\frac{Z_0 k}{4\pi}\int\frac{e^{ik|\boldsymbol{r}-\boldsymbol{r'}|}}{|\boldsymbol{r}-\boldsymbol{r'}|}\boldsymbol{L}\cdot\boldsymbol{M}d^3r';\end{aligned} \tag{2.6}$$

whereas TE mode solutions are also given by

$$\begin{aligned}\boldsymbol{r}\cdot\boldsymbol{E}^{(TE)} &= 0,\\ \boldsymbol{r}\cdot\boldsymbol{H}^{(TE)} &= \frac{i}{4\pi}\int\frac{e^{ik|\boldsymbol{r}-\boldsymbol{r'}|}}{|\boldsymbol{r}-\boldsymbol{r'}|}\boldsymbol{L}\cdot(\boldsymbol{\nabla}\times\boldsymbol{M})\,d^3r'.\end{aligned} \tag{2.7}$$

By combining the two types of modes, in the absence of any local sources, the general solutions of the Maxwell equations in Eq. (2.1) can also be written as

$$\boldsymbol{H} = \sum_{l,m}\left[\alpha_{lm}^{(TM)} f_l(kr)\mathbf{Y}_{l,l,m}(\theta,\phi) - \frac{i}{k}\alpha_{lm}^{(TE)}\boldsymbol{\nabla}\times g_l(kr)\mathbf{Y}_{l,l,m}(\theta,\phi)\right], \tag{2.8}$$

$$\boldsymbol{E} = Z_0\sum_{l,m}\left[\frac{i}{k}\alpha_{lm}^{(TM)}\boldsymbol{\nabla}\times f_l(kr)\mathbf{Y}_{l,l,m}(\theta,\phi) + \alpha_{lm}^{(TE)} g_l(kr)\mathbf{Y}_{l,l,m}(\theta,\phi)\right], \tag{2.9}$$

where the vector spherical harmonic (VSH) $\mathbf{Y}_{l,l,m}$ is defined as $\boldsymbol{L}Y_{lm}(\theta,\phi)/\sqrt{l(l+1)}$. Also $f_l(kr)$ and $g_l(kr)$ are the corresponding solutions of the radial part for each mode,

such that $A_l^{(1)}(kr)h_l^{(1)}(kr)+A_l^{(2)}(kr)h_l^{(2)}(kr)$, in terms of the spherical Hankel functions. The most general form of VSH $\mathbf{Y}_{j,l,m}(\theta,\phi)$ and the corresponding important relations used in this section are given in the Appendix A. The coefficients $\alpha_{lm}^{(TM)}$ and $\alpha_{lm}^{(TE)}$ which specify the amounts of transverse magnetic and transverse electric multipole (l,m) field strengths are determined by the sources and the boundary conditions,

$$\alpha_{lm}^{(TE)} f_l(kr) = \frac{k}{\sqrt{l(l+1)}} \int Y_{lm}^*(\theta,\phi)\boldsymbol{r}\cdot\boldsymbol{H}d\Omega, \tag{2.10}$$

$$\alpha_{lm}^{(TM)} g_l(kr) = -\frac{k}{Z_0\sqrt{l(l+1)}} \int Y_{lm}^*(\theta,\phi)\boldsymbol{r}\cdot\boldsymbol{E}d\Omega. \tag{2.11}$$

Note that the spherical Green's function in the above equations, Eq. (2.6) and Eq. (2.7), has the solutions of radial equations,

$$G_l(r,r') = ikj_l(kr_<)h_l^{(1)}(kr_>) \tag{2.12}$$

with boundary conditions of finiteness at origin, outgoing waves at infinity and the correct discontinuity in slope. Therefore, the spherical wave projection

$$\frac{1}{4\pi}\int d\Omega Y_{lm}^*(\theta,\phi)\frac{e^{ik|\boldsymbol{r}-\boldsymbol{r'}|}}{|\boldsymbol{r}-\boldsymbol{r'}|} = ikh_l^{(1)}(kr)j_l(kr')Y_{lm}^*(\theta',\phi'), \tag{2.13}$$

can be combined with Eqs. (2.6, 2.11) and Eqs. (2.7, 2.10) to obtain the following final expression for the multipole field strength of the fields outside the source:

$$\alpha_{lm}^{(TM)} = \frac{ik^3}{\sqrt{l(l+1)}} \int j_l(kr')Y_{lm}^*(\theta',\phi')\boldsymbol{L}\cdot\boldsymbol{M}d^3r', \tag{2.14}$$

$$\alpha_{lm}^{(TE)} = \frac{-k^2}{\sqrt{l(l+1)}} \int j_l(kr')Y_{lm}^*(\theta',\phi')\boldsymbol{L}\cdot(\boldsymbol{\nabla}\times\boldsymbol{M})\,d^3r'. \tag{2.15}$$

2.2 Second Quantization of the Cavity Field Modes

The magnetic and electric fields given in Eq. (2.8) and Eq. (2.9), respectively, can be quantized seperately for TE and TM modes of the cavity (see Fig. 2.2). Hence, each individual field strength coefficients yield to the respective creation and annihilation operators for each modes, satisfying the corresponding Weyl-Heisenberg relations.

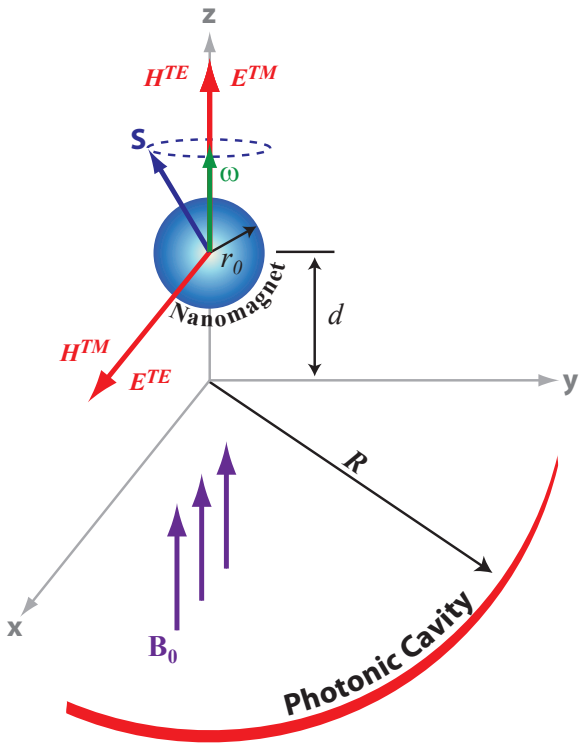

Figure 2.2: The orientations of the electric $\boldsymbol{E}$ and magnetic field $\boldsymbol{H}$ at the nanomagnet site are shown for transverse magnetic (TM) and transverse electric (TE) modes of the photonic cavity.

2.2.1 TE mode

For TE mode, electric and magnetic fields are defined as

$$\boldsymbol{H} = -\frac{i}{k}\sum_{l,m}\alpha_{lm}^{(TE)}\boldsymbol{\nabla}\times\mathbf{u}_{lm}, \tag{2.16}$$

$$\boldsymbol{E} = Z_0\sum_{l,m}\alpha_{lm}^{(TE)}\mathbf{u}_{lm}, \tag{2.17}$$

where the orthogonal basis functions for the expansion are defined as $\mathbf{u}_{lm} = g_l(kr)\mathbf{Y}_{l,l,m}$. The energy of the cavity field is defined as

$$\langle\mathscr{H}\rangle = \frac{1}{2}\int\left(\epsilon_0\boldsymbol{E}^*\cdot\boldsymbol{E} + \mu_0\boldsymbol{H}^*\cdot\boldsymbol{H}\right)d^3r \tag{2.18}$$

in terms of the cavity fields given in Eq. (2.16) and Eq (2.17) rewritten as

$$\boldsymbol{H} = -\frac{i}{2k}\sum_{l,m}\left\{\alpha_{lm}^{(TE)}\left(\boldsymbol{\nabla}\times\mathbf{u}_{lm}\right) - \alpha_{lm}^{*(TE)}\left(\boldsymbol{\nabla}\times\mathbf{u}_{lm}\right)^*\right\}, \tag{2.19}$$

$$\boldsymbol{E} = \frac{Z_0}{2}\sum_{l,m}\left\{\alpha_{lm}^{(TE)}\mathbf{u}_{lm} + \alpha_{lm}^{*(TE)}\mathbf{u}_{lm}^*\right\}. \tag{2.20}$$

Therefore, the energy of the cavity field becomes

$$\langle\mathscr{H}\rangle = \frac{\mu_0}{8}\sum_{l,l'}\sum_{m,m'}\int\alpha_{lm}^{*(TE)}\alpha_{l'm'}^{(TE)}\left\{\mathbf{u}_{lm}^*\mathbf{u}_{l'm'} + \frac{1}{k^2}\left(\boldsymbol{\nabla}\times\mathbf{u}_{lm}\right)^*\cdot\left(\boldsymbol{\nabla}\times\mathbf{u}_{l'm'}\right)\right\}d^3r + c.c. \tag{2.21}$$

where *c.c.* stands for the complex conjugate. The second integrand in Eq. (2.21) can be simplified easily by using the following orthonormality conditions of the basis functions,

$$\begin{aligned}\int\left(\boldsymbol{\nabla}\times\mathbf{u}_{lm}\right)^*\cdot\left(\boldsymbol{\nabla}\times\mathbf{u}_{l'm'}\right)d^3r &= \int\boldsymbol{\nabla}\cdot\left[\mathbf{u}_{l'm'}\times\left(\boldsymbol{\nabla}\times\mathbf{u}_{lm}\right)^*\right]d^3r \\ &\quad + \int\mathbf{u}_{l'm'}\cdot\left[\boldsymbol{\nabla}\times\left(\boldsymbol{\nabla}\times\mathbf{u}_{lm}\right)^*\right]d^3r,\end{aligned} \tag{2.22}$$

where the first term on the right hand side (rhs) will vanish over the surface,

$$\int_V\boldsymbol{\nabla}\cdot\left[\mathbf{u}_{l'm'}\times\left(\boldsymbol{\nabla}\times\mathbf{u}_{lm}\right)^*\right] = \int_S\left[\mathbf{u}_{l'm'}\times\left(\boldsymbol{\nabla}\times\mathbf{u}_{lm}\right)^*\right] = 0, \tag{2.23}$$

from the symmetry properties of TE mode. Moreover, the second term on the rhs can be simplified further by a choice of Coulomb Gauge, $\boldsymbol{\nabla}\cdot\mathbf{u}_{lm} = 0$, i.e.

$$\boldsymbol{\nabla}\times\left(\boldsymbol{\nabla}\times\mathbf{u}_{lm}\right)^* = \boldsymbol{\nabla}\left(\boldsymbol{\nabla}\cdot\mathbf{u}_{lm}\right)^* - \nabla^2\mathbf{u}_{lm} = -\nabla^2\mathbf{u}_{lm} = k^2\mathbf{u}_{lm}. \tag{2.24}$$

Therefore, the second integrand in Eq. (2.21) overall yields to

$$\int (\boldsymbol{\nabla} \times \mathbf{u}_{lm})^* \cdot (\boldsymbol{\nabla} \times \mathbf{u}_{l'm'})\, d^3r = k^2 \int \mathbf{u}^*_{lm} \mathbf{u}_{l'm'} d^3r. \tag{2.25}$$

As a result, the energy of the cavity field takes the simplified form of

$$\langle \mathscr{H} \rangle = \frac{\mu_0}{4} \sum_{l,l'} \sum_{m,m'} \alpha^{*(TE)}_{lm} \alpha^{(TE)}_{l'm'} \int \mathbf{u}^*_{lm} \mathbf{u}_{l'm'} d^3r + c.c. \tag{2.26}$$

Note that for waves having finiteness at the origin, the suitable choice of $g_l(kr)$ becomes the spherical Bessel function of first kind $j_l(kr)$. Imposing the boundary conditions of the transverse magnetic field $\boldsymbol{H}_\perp$ and the longitudinal electric field $\boldsymbol{E}_\parallel$ vanishes at the cavity walls ($r = R$) corresponds to the quantization $k_{l\gamma} = y_{l\gamma}/R$, whereas $y_{l\gamma}$ is the γ-th zero of the spherical Bessel function j_l. Therefore, the following normalization integral

$$\int_0^R j_l(y_{l\gamma} r/R) j_l(y_{lp} r/R) r^2 dr = \frac{R^3}{2} |j'_l(y_{l\gamma})|^2 \delta_{\gamma p}, \tag{2.27}$$

can be used to evaluate the integral given in Eq. (2.26) for the basis functions,

$$\begin{aligned} \int \mathbf{u}^*_{lm} \mathbf{u}_{l'm'} d^3r &= \int j_l(kr) j_{l'}(kr) \mathbf{Y}^*_{l,l,m} \mathbf{Y}_{l',l',m'} r^2 dr d\Omega \\ &= \frac{R^3}{2} |j'_l(y_{l\gamma})|^2 \delta_{ll'} \delta m m', \end{aligned} \tag{2.28}$$

by using the orthogonality properties of VSH. Hence, the final expression for the energy can be obtained as

$$\mathscr{H} = \frac{\mu_0 R^3}{8} \sum_{l,m} |j'_l(y_{l\gamma})|^2 \left(\alpha^{(TE)}_{lm} \alpha^{*(TE)}_{lm} + \alpha^{*(TE)}_{lm} \alpha^{(TE)}_{lm} \right). \tag{2.29}$$

Mapping the multipole field strength coefficients with the corresponding creation and annihilation operators, i.e.

$$\begin{aligned} \alpha^{(TE)}_{lm} &\longmapsto \frac{2}{|j'_l(y_{l\gamma})|} \sqrt{\frac{\hbar \omega_{l\gamma}}{\mu_0 R^3}} a^{(TE)}_{lm}, \\ \alpha^{*(TE)}_{lm} &\longmapsto \frac{2}{|j'_l(y_{l\gamma})|} \sqrt{\frac{\hbar \omega_{l\gamma}}{\mu_0 R^3}} a^{\dagger(TE)}_{lm}, \end{aligned} \tag{2.30}$$

to satisfy the required Weyl-Heisenberg commutation relations of $\left[a_{lm}^{(TE)}, a_{l'm'}^{\dagger(TE)}\right] = \delta_{ll'}\delta_{mm'}$, yields to the second quantized form of the Hamiltonian

$$\mathscr{H}^{(TE)} = \sum_{l,m} \hbar\omega_{l\gamma} \left(a_{lm}^{\dagger(TE)} a_{lm}^{(TE)} + \frac{1}{2}\right). \tag{2.31}$$

for the TE mode of the cavity. The same mapping can also be used to obtain the cavity magnetic field $\boldsymbol{H}$ in a fully quantum treatment,

$$\boldsymbol{H}^{(TE)} = \sum_{l,m} \frac{i}{|j_l'(y_{l\gamma})|} \sqrt{\frac{\hbar\omega_{l\gamma}}{\mu_0 R^3}} \frac{1}{k_{l\gamma}} \left((\boldsymbol{\nabla} \times \mathbf{u}_{lm})^* \, a_{lm}^{\dagger(TE)} - (\boldsymbol{\nabla} \times \mathbf{u}_{lm}) \, a_{lm}^{(TE)} \right) \tag{2.32}$$

2.2.2 TM mode

Similarly, for TM mode, the cavity electric and magnetic fields are given by

$$\boldsymbol{H} = \frac{1}{2} \sum_{l,m} \left\{ \alpha_{lm}^{(TM)} \mathbf{u}_{lm} + \alpha_{lm}^{*(TM)} \mathbf{u}_{lm}^* \right\}, \tag{2.33}$$

$$\boldsymbol{E} = \frac{iZ_0}{2k} \sum_{l,m} \left\{ \alpha_{lm}^{(TM)} \left(\boldsymbol{\nabla} \times \mathbf{u}_{lm}\right) + \alpha_{lm}^{*(TM)} \left(\boldsymbol{\nabla} \times \mathbf{u}_{lm}\right)^* \right\}, \tag{2.34}$$

where the basis functions for TM mode are given by $\mathbf{u}_{lm} = f_l(kr)\mathbf{Y}_{l,l,m}$. By using the properties of basis functions given in Eqs. (2.22-2.25) again, the energy of the cavity field for the TM mode can be written as

$$\langle \mathscr{H} \rangle = \frac{\mu_0}{4} \sum_{l,l'} \sum_{m,m'} \alpha_{lm}^{*(TM)} \alpha_{l'm'}^{(TM)} \int \mathbf{u}_{lm}^* \mathbf{u}_{l'm'} d^3r + c.c. \tag{2.35}$$

The boundary conditions for the TM mode are somewhat more involved than the TE mode. The condition of $H_\perp = 0$ is trivially satisfied by $\boldsymbol{r} \cdot \mathbf{u}_{lm} = 0$ at the cavity walls, whereas the condition of $E_\parallel = 0$ gives

$$\left[\boldsymbol{r} \times (\boldsymbol{\nabla} \times f_l(kr)\mathbf{Y}_{l,l,m})\right]|_{r=R} = -\partial_r \left(r f_l(kr)\right) \mathbf{Y}_{l,l,m} = 0. \tag{2.36}$$

By noting that $f_l(kr) = j_l(kr)$, the appropriate normalization integral needs to be modified for integrating zeros of $|rj_l(kr)|'$, and it may be written as

$$\int_0^R j_l(x_{l\gamma} r/R) j_l(x_{lp} r/R) r^2 dr = \frac{R^3}{2} \left(1 - \frac{l(l+1)}{x_{l\gamma}^2}\right) |j_l(x_{l\gamma})|^2 \delta_{\gamma p}. \tag{2.37}$$

Therefore, the integral in Eq. (2.35) obtained as

$$\begin{aligned}\int \mathbf{u}^*_{lm}\mathbf{u}_{l'm'}d^3r &= \int j_l(kr)j_{l'}(kr)\mathbf{Y}^*_{l,l,m}\mathbf{Y}_{l',l',m'}r^2drd\Omega,\\ &= \frac{R^3}{2}\left(1-\frac{l(l+1)}{x^2_{l\gamma}}\right)|j_l(x_{l\gamma})|^2\delta_{ll'}\delta mm', \end{aligned} \tag{2.38}$$

used with the mapping of the multipole strength coefficients to the appropriate creation and annihilation operators,

$$\begin{aligned}\alpha^{(TM)}_{lm} &\longmapsto \frac{2}{|j_l(x_{l\gamma})|}\left[1-\frac{l(l+1)}{x^2_{l\gamma}}\right]^{-1/2}\sqrt{\frac{\hbar\omega_{l\gamma}}{\mu_0R^3}}a^{(TM)}_{lm},\\ \alpha^{*(TM)}_{lm} &\longmapsto \frac{2}{|j_l(x_{l\gamma})|}\left[1-\frac{l(l+1)}{x^2_{l\gamma}}\right]^{-1/2}\sqrt{\frac{\hbar\omega_{l\gamma}}{\mu_0R^3}}a^{\dagger(TM)}_{lm}, \end{aligned} \tag{2.39}$$

yields to the following second quantized form of the Hamiltonian for the TM mode,

$$\mathscr{H}^{(TM)} = \sum_{l,m}\hbar\omega_{l\gamma}\left(a^{\dagger(TM)}_{lm}a^{(TM)}_{lm}+\frac{1}{2}\right). \tag{2.40}$$

Similarly, the quantum mechanically treated cavity magnetic field is also obtained as

$$\boldsymbol{H}^{(TM)} = \sum_{l,m}\frac{1}{|j_l(x_{l\gamma})|}\left[1-\frac{l(l+1)}{x^2_{l\gamma}}\right]^{-1/2}\sqrt{\frac{\hbar\omega_{l\gamma}}{\mu_0R^3}}\left(a^{\dagger(TM)}_{lm}\mathbf{u}^*_{lm}+a^{(TM)}_{lm}\mathbf{u}_{lm}\right) \tag{2.41}$$

2.3 Interaction Hamiltonian

For a nanomagnet placed inside a microcavity, armed only with the definition of the energy of the Maxwell field, the total Hamiltonian of the system is given by

$$\begin{aligned}\langle\mathscr{H}\rangle &= \frac{1}{2}\int(\boldsymbol{H}\cdot\boldsymbol{B}+\boldsymbol{E}\cdot\boldsymbol{D})\,d^3r\\ &= \frac{1}{2}\int\left(\mu_0|\boldsymbol{H}|^2+\epsilon_0|\boldsymbol{E}|^2\right)d^3r+\frac{1}{2}\int\mu_0\boldsymbol{H}\cdot\boldsymbol{M}d^3r, \end{aligned} \tag{2.42}$$

where the electric displacement field, and magnetic flux are defined as $\boldsymbol{D}=\epsilon_0\boldsymbol{E}$ and $\boldsymbol{B}=\mu_0(\boldsymbol{H}+\boldsymbol{M})$, respectively. It is important to notice that the internal dynamics of the nanomagnet proportional with the square of its magnetization $\boldsymbol{M}^2$ is already included in the above interaction Hamiltonian Eq. (2.39). This can be explicitly seen by rewriting the Hamiltonian in terms of the so-called magnetic flux $\boldsymbol{B}$. Fully quantum treatment of the first integral on the rhs of Eq. (2.42) have already been obtained in Sections 2.2.1 and 2.2.2 by second quantizing the cavity field for TE and TM modes

seperately. Inserting the expressions for $\boldsymbol{H}$, given in Eq. (2.32) for TE mode and in Eq. (2.41) for TM mode, into the second integral term of the above Eq. (2.42) yields to the interaction Hamiltonian in a semiclassical manner,

$$\mathscr{H}_I = \sum_{l,m} \left\{ \Gamma_{l\gamma}^{(TE)} a_{lm}^{(TE)} \int_{V_N} \boldsymbol{M} \frac{(\boldsymbol{\nabla} \times \mathbf{u}_{lm})}{k_{l\gamma}} d^3r + \Gamma_{l\gamma}^{(TM)} a_{lm}^{(TM)} \int_{V_N} \boldsymbol{M} \cdot \mathbf{u}_{lm} d^3r \right\} + H.c. \tag{2.43}$$

where magnetization $\boldsymbol{M}$ is still in the classical form and $H.c.$ corresponds to the Hermitian conjugate. Note that $\Gamma_{l\gamma}^{(TE)}$ and $\Gamma_{l\gamma}^{(TM)}$ stands for the coupling constants defined as

$$\Gamma_{l\gamma}^{(TE)} = \frac{i}{2|j_l'(y_{l\gamma})|} \sqrt{\frac{\hbar\omega_{l\gamma}\mu_0}{R^3}}, \tag{2.44}$$

$$\Gamma_{l\gamma}^{(TM)} = \frac{1}{2|j_l(x_{l\gamma})|} \left[1 - \frac{l(l+1)}{x_{l\gamma}^2}\right]^{-1/2} \sqrt{\frac{\hbar\omega_{l\gamma}\mu_0}{R^3}}, \tag{2.45}$$

for TE and TM modes for simplicity purposes.

The radiation of the cavity field is due to the harmonically oscillating components of the nanomagnet magnetization in the x-y plane, namely $\boldsymbol{M}_{x,y}$. Because of this symmetry property of the cavity-nanomagnet system, it can be readily seen that the multipole field strength coefficients $\alpha_{lm}^{(TE)}$ for TE mode, given in Section 2.1 by Eq. (2.15), will simply vanish by the following relation of any well-behaved vector field,

$$\boldsymbol{L} \cdot (\boldsymbol{\nabla} \times \boldsymbol{M}) = i\nabla^2 (\boldsymbol{r} \cdot \boldsymbol{M}) - \frac{i}{r} \frac{\partial}{\partial r} \left(r^2 \boldsymbol{\nabla} \cdot \boldsymbol{M} \right). \tag{2.46}$$

Note that since the oscillating components of magnetization is perpendicular to the radial direction, all coefficients for TE mode will clearly yield to zero (see Fig. 2.2). Therefore, TM mode is the only non-vanishing mode to be considered in the interaction Hamiltonian of the cavity-nanomagnet system.

We consider the nanomagnet acting like a giant macrospin, as in the case of large iron clusters, hence the magnetization in Eq. (2.43) can be defined as

$$\boldsymbol{M} = \frac{\boldsymbol{\mu}}{V_N} = -\frac{g\mu_B}{\hbar V_N} \Theta \left(r_0 - |\boldsymbol{r} - \boldsymbol{d}| \right) \boldsymbol{S} \tag{2.47}$$

in terms of the collective quantum spin operator of the nanomagnet; where μ_B, and V_N correspond to the Bohr magneton and the volume of the nanomagnet, respectively. Note that the Heaviside theta function Θ localizes the magnetization into the spherical nanomagnet of radius r_0 at a position of d away from the center of the cavity (Fig. 1).

If one writes the coordinate unit vectors $\hat{\mathbf{x}}$, $\hat{\mathbf{y}}$, and $\hat{\mathbf{z}}$ in spherical notation,

$$\hat{\mathbf{e}}_+ = -\tfrac{\hat{\mathbf{x}}+i\hat{\mathbf{y}}}{\sqrt{2}}, \quad \hat{\mathbf{e}}_- = \tfrac{\hat{\mathbf{x}}-i\hat{\mathbf{y}}}{\sqrt{2}}, \quad \hat{\mathbf{e}}_0 = \hat{\mathbf{z}}, \tag{2.48}$$

so that $\hat{\mathbf{e}}_m$ form a spherical tensor of rank 1. Therefore, the collective spin operator can be written in terms of the collective spin raising and lowering operators, i.e.

$$\boldsymbol{S} = \frac{1}{\sqrt{2}}\left(S_+\hat{\mathbf{e}}_- - S_-\hat{\mathbf{e}}_+\right) + S_z\hat{\mathbf{e}}_0 \tag{2.49}$$

in helicity basis. By using the relation between the magnetization and the collective spin operator given in Eq. (2.47), it is obvious from Eq. (2.14) that dipole field strength coefficient dominates over other multipole field strength coefficients, i.e. $\alpha_{1m}^{(TM)} \gg \alpha_{2m}^{(TM)} \gg \alpha_{3m}^{(TM)} \gg \ldots$. It is important to mention that spherical wave expansion of magnetic field has several unique features such that all components of the field are identically zero if $l = m = 0$, dictating that there are no radiating monopoles. This is also equivalent to stating that there are no spherical transverse electromagnetic waves (TEM) in free space. Therefore, for the interaction Hamiltonian given in Eq. (2.43), the multipole terms rather than the dipole term are negligible. In this case, the basis functions for the dipole TM mode can be written as,

$$\begin{aligned}
\mathbf{u}_{11} &= \frac{1}{\sqrt{2}} j_1(kr)\left(Y_{11}(\theta,\phi)\hat{\boldsymbol{e}}_0 - Y_{10}(\theta,\phi)\hat{\boldsymbol{e}}_+\right), \\
\mathbf{u}_{10} &= \frac{1}{\sqrt{2}} j_1(kr)\left(Y_{11}(\theta,\phi)\hat{\boldsymbol{e}}_- - Y_{1\bar{1}}(\theta,\phi)\hat{\boldsymbol{e}}_+\right), \\
\mathbf{u}_{1\bar{1}} &= \frac{-1}{\sqrt{2}} j_1(kr)\left(Y_{1\bar{1}}(\theta,\phi)\hat{\boldsymbol{e}}_0 - Y_{10}(\theta,\phi)\hat{\boldsymbol{e}}_-\right),
\end{aligned} \tag{2.50}$$

by setting $l = 1$ in the relations given in Appendix A. In the case of a very small nanomagnet relative to the size of the cavity, the zenith angle in Eqs. (2.50) can be taken to be very small, i.e. $\sin(\theta) \simeq \theta \simeq 0$. Therefore, the corresponding spherical

harmonics used for the dipole TM mode becomes

$$\begin{aligned} Y_{11} &= -\frac{1}{2}\sqrt{\frac{3}{2\pi}}\sin\theta e^{i\phi} \simeq 0, \\ Y_{10} &= \frac{1}{2}\sqrt{\frac{3}{\pi}}\cos\theta \simeq \frac{1}{2}\sqrt{\frac{3}{\pi}}, \\ Y_{1\bar{1}} &= \frac{1}{2}\sqrt{\frac{3}{2\pi}}\sin\theta e^{-i\phi} \simeq 0, \end{aligned} \tag{2.51}$$

in the limit of $r \cong d$. It is also useful to note that the dot product of two arbitrary vectors given as $\boldsymbol{A} = \sum_{\mu=0,\pm1} A_\mu \hat{\mathbf{e}}_\mu$, is defined as $\boldsymbol{A}\cdot\boldsymbol{B} = \sum_{\mu=0,\pm1}(-1)^\mu A_\mu B_{-\mu}$ in the helicity basis. Combining the relations from Eq.(2.43) through Eq.(2.51) yields to the following final form of the interaction Hamiltonian

$$\mathscr{H}_I = -g\mu_B\Gamma_\gamma\left(a_-S_- + a_-^\dagger S_+ + a_+S_+ + a_+^\dagger S_-\right), \tag{2.52}$$

where the spin-photon coupling constant, Γ_γ is also obtained as

$$\Gamma_\gamma = \frac{j_1(kd)}{8\hbar|j_1(x_{1\gamma})|}\left[1-\frac{2}{x_{1\gamma}^2}\right]^{-1/2}\sqrt{\frac{3\hbar\omega_{1\gamma}\mu_0}{\pi R^3}}. \tag{2.53}$$

The relation between the dipole TM mode frequency $\omega_{1\gamma}$ and the radius of the microcavity R can be easily seen to be $k_{1\gamma} = \omega_{1\gamma}/c = x_{1\gamma}/R$.

Note that the interaction Hamiltonian actually consists of four terms. The term $a_+^\dagger S_-$ corresponds to the process in which the spin is flipped from the up state to the down state and a photon with positive helicity is created, whereas the term a_+S_+ describes the opposite process. The energy as well as the quanta is obviously conserved in both processes. However, the term a_-S_- corresponds to the process in which the spin makes a transition from up to down state and a photon with negative helicity is annihilated, resulting in the loss of roughly $2\hbar\omega_\gamma$ in energy. Similarly, the term $a_-^\dagger S_+$ results with a gain of $2\hbar\omega_\gamma$ in energy. Therefore, these energy nonconserving terms, where the photon possesses a negative helicity, can be dropped by using the rotating-wave approximation. In addition to this necessary reduction, the total Hamiltonian of the spin-cavity system also needs to be modified by including the effect of the applied uniform magnetic field $\boldsymbol{B}_0$ with the term $-\boldsymbol{\mu}\cdot\boldsymbol{B}_0$. As a result the total Hamiltonian

of the spin-cavity system is obtained as

$$\begin{aligned}\mathscr{H} &= \mathscr{H}_0 + \mathscr{H}_I \\ &= \hbar\omega_\gamma \left(a^\dagger a + \frac{1}{2}\right) + \frac{g\mu_B B_0}{\hbar} S_z - g\mu_B \Gamma_\gamma \left(aS_+ + a^\dagger S_-\right), \end{aligned} \tag{2.54}$$

where the helicity dependence of creation and annihilation operators has been dropped for simplicity and the first two terms on the rhs can be combined together to be treated as the homogenous part of the Hamiltonian H_0. Therefore, in the interaction picture the Hamiltonian becomes

$$\begin{aligned}\mathscr{V}(t) &= e^{iH_0 t/\hbar} \mathscr{H}_I e^{-iH_0 t/\hbar} \\ &= g\mu_B \Gamma_\gamma \left(aS_+ e^{i\Delta t} + a^\dagger S_- e^{-i\Delta t}\right), \end{aligned} \tag{2.55}$$

where the frequency difference is defined as $\Delta = \nu - \omega$, in which ν corresponds to the precession frequency due to the applied uniform magnetic field B_0 and given by $\nu = g\mu_B B_0/\hbar$. Hence, it can be readily seen that the exact resonance condition corresponds to $\Delta = 0$. Therefore, everytime any spin of the nanomagnet flips up (down) will result an absorption (emission) of a photon.

In conclusion, we have obtained the Hamiltonian of the spin-cavity system given in Eq. (2.54) with coupling strengths defined in Eq. (2.53) in a fully quantum treatment. Before ending this chapter, it is important to emphasize some of the measures of the physical quantities mentioned in the Hamiltonian. An applied magnetic field B_0 of 7 T corresponding to a precession frequency of $\omega = 196.2$ GHz will cause the nanomagnet to be in exact resonance ($\omega \cong \nu$) with a cavity volume of 1.25 mm^3. Moreover, the system will possesses roughly 10^9 spin 1/2 particles for a spherical nanomagnet of radius $r_0 \approx 108$ nm consisting of Fe-atoms with a magnetic moment of $2.21\,\mu_B$ per atom.

CHAPTER 3
SOLUTIONS OF THE SPIN-CAVITY HAMILTONIAN

Although the similarities of our Hamiltonian in Eq. (2.54) to the Dicke Model and Tavis-Cummings Model are undeniable at the first glance, it is worthwhile to emphasize the details of this analogy here. In standard Dicke Model, for N atoms the atomic product state written as, $|\Phi\rangle = |1_1\rangle|1_2\rangle|2_3\rangle|1_4\rangle \ldots\ldots |1_N\rangle$, where $|1\rangle$ ($|2\rangle$) corresponds to the lower (excited) state, can be chosen as simultaneous eigenstates of the collective atomic spin operators $\mathscr{R}^2$, and $\mathscr{R}_z$ given by $|l, m\rangle$. In addition to a substantial reduction in degeneracy of the energy eigenvalues, this also allows us to immediately identify the constraints on l as $|m| \leq l \leq N/2$. It is important to note that l, the so-called *cooperation number*, plays a key role in determining the rate of cooperative radiation by the atomic system. Although our formalism is similar to the Dicke Model, in our case, the choice of the corresponding subspace of l is determined by the macrospin approach. Due to the applied magnetic field $\boldsymbol{B}_0$ along the positive z-axis (Fig. 2.1), all N spins of the nanomagnet initially pointing upward is similar to the case of initially fully excited atomic system in Dicke Model.

3.1 Fock Basis Representation

The initial state of our spin-cavity system decided by the applied magnetic field dictates the only choice of $l = N/2$ subspace with no degeneracy, amongst all possible subspaces of l. Therefore, the basis kets of the Hamiltonian in Eq. (2.54) can be written as the simultaneous eigenkets of the Fock states for cavity photons ($|n\rangle$), the eigenkets of the collective spin operator, and its z-axis projection ($|l, m\rangle$),

$$\mathscr{F} \oplus (\mathscr{S}^2, \mathscr{S}_z) = |n\rangle \otimes |l, m\rangle. \tag{3.1}$$

Since the total excitation number is conserved in our model, the obvious constant of motion of the spin-cavity system can be easily revealed to be

$$\xi = n + m = N/2\,, \tag{3.2}$$

where the total number of spins considered is given by N. Therefore, the product basis kets $|n\rangle \otimes |l, m\rangle$ can be reduced to a much more simplified formalism of

$$|n\rangle|l, m\rangle \equiv |n, \xi - n\rangle \;\; or \;\; |\xi - m, m\rangle, \tag{3.3}$$

depending solely on either photon number of the cavity n or the eigenvalues of the collective spin operator along the z-axis m. Hence, by operating the Hamiltonian of Eq. (2.54) on these states, one can obtain the Hamiltonian

$$\mathscr{H} = \sum_{n=0}^{2\xi} E_0 |n\rangle\langle n| - \tau(n) \left[|n+1\rangle\langle n| + |n\rangle\langle n+1|\right], \tag{3.4}$$

in Fock basis, where the constant energy term E_0 and magnet-microwave mode coupling $\tau(n)$ are given by

$$\begin{aligned} E_0 &= \hbar\omega\,(\xi + 1/2) \\ \tau(n) &= \hbar\Gamma_\gamma g\mu_B (n+1)\sqrt{2\xi - n}\,. \end{aligned} \tag{3.5}$$

Since the E_0 term does not depend on photon number for the exact resonance case, it only causes a constant shift in all energy levels, and therefore it can be omitted in our calculations. Discrete lattice-like schematic of the Hamiltonian in Eq. (3.4) is shown in Fig. 3.1.

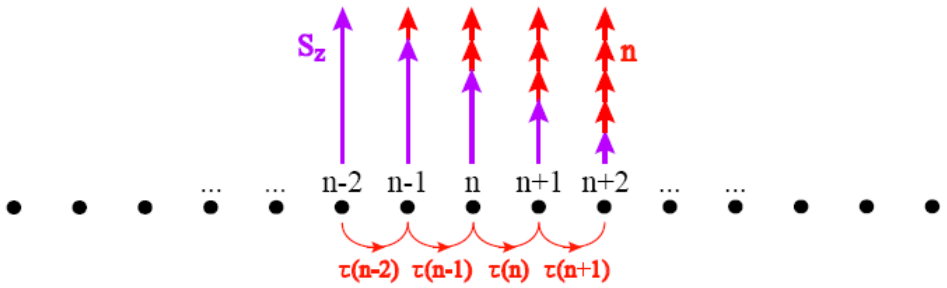

Figure 3.1: Lattice-like schematic of the spin-cavity Hamiltonian is shown where successive lattice sites represent the corresponding photon numbers in the microcavity. Note that the constant of motion of the Hamiltonian can also be clearly seen from the addition of arrows belonging to the nanomagnet spins along the z-axis S_z (*purple*) and corresponding cavity photon numbers n (*red*) for each site.

Starting with an initial configuration of no photons present in the cavity and the collective spin of the nanomagnet oriented parallel to the field $|0,\xi\rangle$, the magnet-microwave mode coupling $\tau(n)$ changes dramatically over a range from MHz to THz. Note that the matrix form of the above Hamiltonian, i.e.

$$\begin{pmatrix} E_0 & -\tau(0) & 0 & 0 & \cdots & 0 \\ -\tau(0) & E_0 & -\tau(1) & 0 & \cdots & 0 \\ 0 & -\tau(1) & E_0 & -\tau(2) & \cdots & 0 \\ \cdots & & & & & \cdots \\ 0 & 0 & 0 & \cdots & -\tau(2\xi-1) & E_0 \end{pmatrix}, \tag{3.6}$$

has a dimension of roughly $10^9 \times 10^9$ and it looks very similar to the one dimensional tight-binding form [115], except the constant diagonal terms E_0. Hence, it can be readily seen from the Hamiltonian given in Eq. (3.4), the first derivative of the magnet-microwave mode coupling $\partial\tau(n)/\partial n$ acts like a driving force between the successive photon numbers of the cavity, i.e. $|0\rangle \rightarrow \cdots\cdots \rightarrow |n-1\rangle \rightarrow |n\rangle \rightarrow |n+1\rangle \rightarrow \cdots\cdots \rightarrow |2\xi\rangle$. Therefore, finding the roots of the following relation

$$\frac{\partial\tau(n)}{\partial n}|_{n_0} = 0, \tag{3.7}$$

reveals the location of the equilibrium point as $n_0 = (4\xi-1)/3$ in terms of the cavity photon number. Equivalently, in terms of the collective spin number along the z-axis m, magnet-microwave mode coupling can be expressed as

$$\tau(m) = (\xi - m + 1)\sqrt{\xi + m} \tag{3.8}$$

with an equilibrium point of $m_0 = (1-\xi)/3$. Therefore, for a nanomagnet consisting of very large number of spins ($\xi \gg 1$), all the eigenfunctions of the Hamiltonian given in Eq. (3.4) are expected to be centered about the equilibrium point $n_0 = 4\xi/3$ or equivalently $m_0 = -\xi/3$.

Now lets assume our spin-cavity system is initially in a random state given by

$|n\rangle|l,m\rangle$. If we are only interested in transitions which conserve energy and in which a photon is emitted, the rate of photon emission can be found to be proportional with the terms like

$$r_n \propto \sum_{\forall\Psi} |\langle\Psi|a^\dagger S_-|n\rangle|l,m\rangle|^2, \tag{3.9}$$

where the sum is carried over all possible final states of the system represented by $|\Psi\rangle$. After matrix elements of the spin system and of the field are seperated, the rate of photon emission can be obtained as

$$\begin{aligned} r_n \propto A\langle m|S_+S_-|m\rangle\langle n|aa^\dagger|n\rangle &= A(n+1)^2(2\xi-n) &(3.10)\\ &\equiv A(\xi-m+1)^2(\xi+m) &(3.11)\end{aligned}$$

in terms of photon number or collective spin number along the z-axis. The physical significance of the factor A can be readily identified by applying the rate of photon emission r_n given above to a single spin case, where $\xi = 1/2$. Assuming this spin is initially pointing upward $m = 1/2$ and there are no photons present in the cavity $n = 0$, the rate of photon emission r_n yields to A, which reveals itself to be nothing more but the spin analog of the Eistein A-coefficient. In the large spin limit, it can be easily seen that the rate of photon emission reaches its maximum value of $4A(N/3)^3$ for the equilibrium point n_0 or equivalently m_0. Therefore, the physical significance of these equilibrium points n_0 and m_0 can be realized as the points where the *superradiance* regime lies at for the spin-cavity system in terms of the photon and collective spin numbers, respectively.

3.2 Continuous Representation

Finding the solutions of the spin-cavity Hamiltonian corresponds to the diagonalization of huge matrices in the form of Eq. (3.6). Fortunately enough, as it will be shown in this and upcoming sections, this disadvantage can still be avoided by treating the Hamiltonian in the proper continuum limit to obtain a coherent state representation of the spin-cavity system. In the most general form, the eigenstates of

the spin-cavity system Hamiltonian in Eq. (3.4) can be expanded in terms of the Fock number states,

$$\Psi_j = \sum_{n'=0}^{2\xi} \psi_j^{n'} |n'\rangle, \tag{3.12}$$

where the proper phase constants are given by $\psi_j^{n'}$ for each photon number in the field basis. Operating the Hamiltonian of Eq. (3.4) on these states, i.e.

$$\mathscr{H}\Psi_j = \sum_{n=0}^{2\xi}\sum_{n'=0}^{2\xi} \left\{ E_0 \psi_j^{n'} |n\rangle\langle n|n'\rangle - \tau(n)\psi_j^{n'} \left[|n+1\rangle\langle n|n'\rangle + |n\rangle\langle n+1|n'\rangle \right] \right\}, \tag{3.13}$$

with the aid of time independent Schrödinger equation $\mathscr{H}\Psi_j = E_j\Psi_j$, where E_j corresponds to the eigenvalues of the spin-cavity system, yields to the following relation,

$$\sum_{n'=0}^{2\xi}\sum_{n=0}^{2\xi} \left\{ E_0 \psi_j^{n'} |n\rangle\delta_{n,n'} - \tau(n)\psi_j^{n'} |n+1\rangle\delta_{n,n'} - \tau(n)\psi_j^{n'} |n\rangle\delta_{n+1,n'} \right\} = \sum_{n'=0}^{2\xi} E_j \psi_j^{n'} |n'\rangle. \tag{3.14}$$

The summation over the states with n will be dropped off by using the Kronecker delta functions obtained from the orthogonality condition of Fock number states, i.e. $\langle n|n'\rangle = \delta_{n,n'}$. Therefore, Eq. (3.14) can be reduced to

$$\sum_{n'=0}^{2\xi} \left\{ (E_j - E_0)\psi_j^{n'} |n'\rangle + \tau(n)\psi_j^{n'} |n'\rangle + \tau(n'-1)\psi_j^{n'} |n'-1\rangle \right\} = 0 \ ; \tag{3.15}$$

furthermore, by changin the dummy indices $n' \to n'-1$ and $n' \to n'+1$ for the second and the third terms in the summation on the left hand side (lhs) of Eq. (3.15) respectively, one can obtain the relation

$$\begin{aligned} 0 &= \sum_{n'=0}^{2\xi} (E_j - E_0)\psi_j^{n'} |n'\rangle + \sum_{n'=1}^{2\xi+1} \tau(n'-1)\psi_j^{n'-1} |n'\rangle + \sum_{n'=-1}^{2\xi-1} \tau(n')\psi_j^{n'+1} |n'\rangle, \\ &= \sum_{n'=0}^{2\xi} \left\{ (E_j - E_0)\psi_j^{n'} + \tau(n'-1)\psi_j^{n'-1} + \tau(n')\psi_j^{n'+1} \right\}, \end{aligned} \tag{3.16}$$

where the values of $\tau(-1) = \tau(2\xi) = 0$ are used to appropriately readjust the range of the summations over the values of n' to allow further reduction leading to the following important recursion relation,

$$(E_j - E_0)\psi_j^n + \tau(n-1)\psi_j^{n-1} + \tau(n)\psi_j^{n+1} = 0, \tag{3.17}$$

for the phase constants ψ_j^n of Fock states. Note that the dummy indice n' has been finally changed to n for simplicity purposes. Since the nanomagnet possesses very large number of spins roughly $2\xi = N = 10^9$, the continuum limit consists in making the replacement of $\psi_j^n \to \psi_j(n\varepsilon)$ to the discrete phase coefficients of Eq. (3.12). Therefore, the continuous lattice-like relation can be easily obtained as

$$E_j\psi_j(n\varepsilon) + \tau(n\varepsilon)\psi_j(n\varepsilon+\varepsilon) + \tau(n\varepsilon-\varepsilon)\psi_j(n\varepsilon-\varepsilon), \tag{3.18}$$

from the discrete recursion relation given in Eq. (3.17) with a so-called lattice constant ε. Since the constant shift in the energy spectrum has no effect on the eigenvalues and eigenfunctions, the E_0 term has been also omitted in Eq. (3.18). Moreover, by introducing the Taylor expansions of the functions ψ_j and τ_j

$$\psi_j(n\varepsilon+\varepsilon) = \psi_j(n\varepsilon) + \varepsilon\frac{d\psi_j(n\varepsilon)}{d(n\varepsilon)} + \frac{1}{2\varepsilon^2}\frac{d^2\psi_j(n\varepsilon)}{d(n\varepsilon)^2} + O(\varepsilon^3), \tag{3.19}$$

$$\psi_j(n\varepsilon-\varepsilon) = \psi_j(n\varepsilon) - \varepsilon\frac{d\psi_j(n\varepsilon)}{d(n\varepsilon)} + \frac{1\varepsilon^2}{2}\frac{d^2\psi_j(n\varepsilon)}{d(n\varepsilon)^2} + O(\varepsilon^3), \tag{3.20}$$

$$\tau(n\varepsilon-\varepsilon) = \tau(n\varepsilon) - \varepsilon\frac{d\tau(n\varepsilon)}{d(n\varepsilon)} + \frac{1\varepsilon^2}{2}\frac{d^2\tau(n\varepsilon)}{d(n\varepsilon)^2} + O(\varepsilon^3), \tag{3.21}$$

into Eq. (3.18) up to the order of $O(\varepsilon^3)$, the eigenvalue problem of the matrix given in Eq. (3.6) can be simply reduced to a problem of finding the solutions of the following second-order ordinary differential equation:

$$\tau(x)\frac{d^2\psi_j(x)}{dx^2} + \frac{d\tau(x)}{dx}\frac{d\psi_j(x)}{dx} + \left(2\tau(x) - \frac{d\tau(x)}{dx} + \frac{1}{2}\frac{d^2\tau(x)}{dx^2} + E_j\right)\psi_j(x) = 0, \tag{3.22}$$

with the boundary conditions of $\psi_j(0) = \psi_j(2\xi) = 0$, where x is defined by the transformation $x \to n\varepsilon$. While the above differential equation needs to be solved in the domain of $[0, 2\xi]$, the lattice constant can be set equal to the difference in successive photon numbers, i.e. $\varepsilon = 1$, since $\varepsilon \ll 2\xi$ and $\psi_j(n\varepsilon)$ is a smoothly varying function.

Since Eq. (3.22) is a linear second-order homogeneous differential equation, it can be transformed into the standard form of

$$\frac{d^2z_j(x)}{dx^2} + q^2(x, E_j)z_j(x) = 0, \tag{3.23}$$

with the first-order term eliminated using the substitution

$$\ln \psi_j(x) = \ln z_j(x) - \frac{1}{2}\int \frac{\tau'(x)}{\tau(x)}dx, \tag{3.24}$$

where the polynomial $q(x)$ is obtained as,

$$q^2(x, E_j) = \frac{2\tau(x) - \tau'(x) + E_j}{\tau(x)} + \frac{\tau'^2(x)}{4\tau^2(x)}. \tag{3.25}$$

Note that by defining the effective potential (see Fig. 3.2) and the effective mass as

$$V_e(x) = \tau'(x) - \frac{\tau'^2(x)}{4\tau(x)} - 2\tau(x), \tag{3.26}$$

$$m_e(x) = \frac{\hbar^2}{2\tau(x)}, \tag{3.27}$$

respectively, the polynomial in Eq. (3.23) can be rewritten as

$$q(x) = \sqrt{\frac{2m_e(E_j - V_e(x))}{\hbar^2}}. \tag{3.28}$$

in a more physically familiar form of so-called wavevector of this continuous representation. Hence the Eq. (3.22) has been transformed into a time-independent Schrödinger equation, application of Wentzel-Kramers-Brillouin (WKB) approximation with a validity of

$$|q(x)| \gg \left|\frac{1}{2q(x)}\frac{dq(x)}{dx}\right|, \tag{3.29}$$

yields to the quantization of the classical action given by

$$S(E_j) = \frac{1}{2\pi}\oint \sqrt{\frac{E_j - V_e(x)}{\tau(x)}}dx = j + \frac{1}{2}, \tag{3.30}$$

for a smoothly varying effective potential $V_e(x)$ as shown in Fig. 3.2. Note that the successive values of the indices j corresponds to the each energy level allowed by Eq. (3.22), i.e. $j = 0$ for the ground state, $j = 1$ for the first excited state, $j = 2$ for the second excited state of the spin-cavity system, and so on. Hence, the energy eigenvalues necessary to solve the differential equation given in Eq. (3.22), and to obtain the wavefunctions of the spin-cavity system, can be easily obtained by the quantization of the classical action defined in Eq. (3.30). Unfortunately, the WKB method fails to produce every energy level of the spin-cavity spectrum precisely.

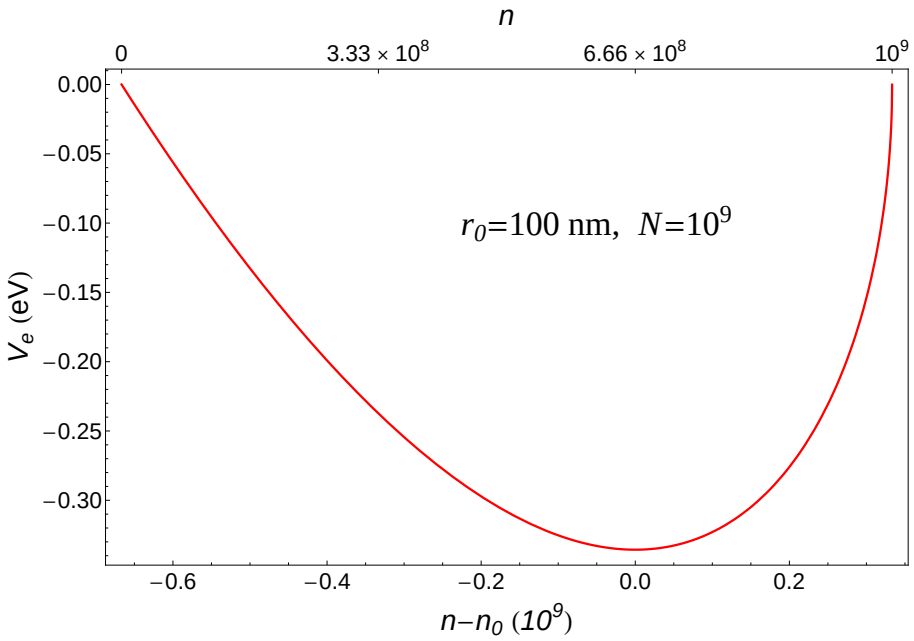

Figure 3.2: The effective potential of the magnet-cavity system (for $N = 10^9$ spins) in the WKB approximation is shown with respect to cavity photon number n centered around the superradiance regime n_0.

However, it is expected to yield very accurate energy values in the vicinity of the minimum of the effective potential $V_e(x)$. This can be easily seen from the fact that around the equilibrium points n_0 (or m_0) the effective potential has its global minimum at a location where it is indeed very slowly varying while it is also satisfying the necessary condition given by Eq. (3.29). The comparison between the wavefunctions obtained by continuous WKB approximation $\psi_j(x)$ and the discreete exact solutions ψ_j^n is shown in Fig. 3.3 and Fig. 3.4 for the eigenfunctions of some small enough spin samples.

Direct comparison of the same order wavefunctions for different cavity photon number and nanomagnet total spin, given in Fig. 3.3f and Fig. 3.4f, reveals the fact that confinement gets better between the continuous wavefunctions and their corresponding exact solutions with increasing number of total photon numbers or spins contained in the spin-cavity system. For the nanomagnet consisting of 10^9 spins (which yields to a

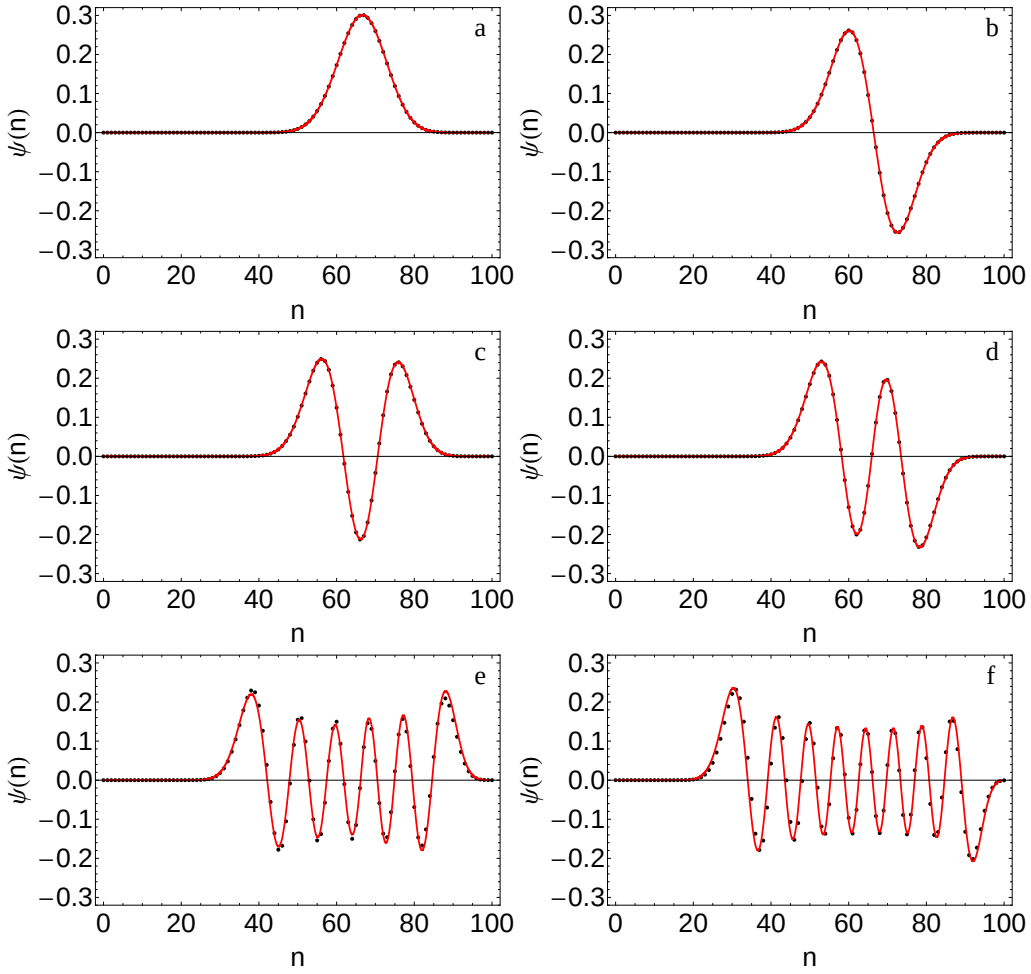

Figure 3.3: Normalized wavefunctions of the nanomagnet-cavity system consisting of 10^2 spins obtained from the exact solutions (*black, dotted*), and from the continuous WKB (*red, solid*) approximation are shown for the (a) ground state, and (b) 1^{st}, (c) 2^{nd}, (d) 3^{rd}, (e) 10^{th}, and (f) 15^{th} excited states.

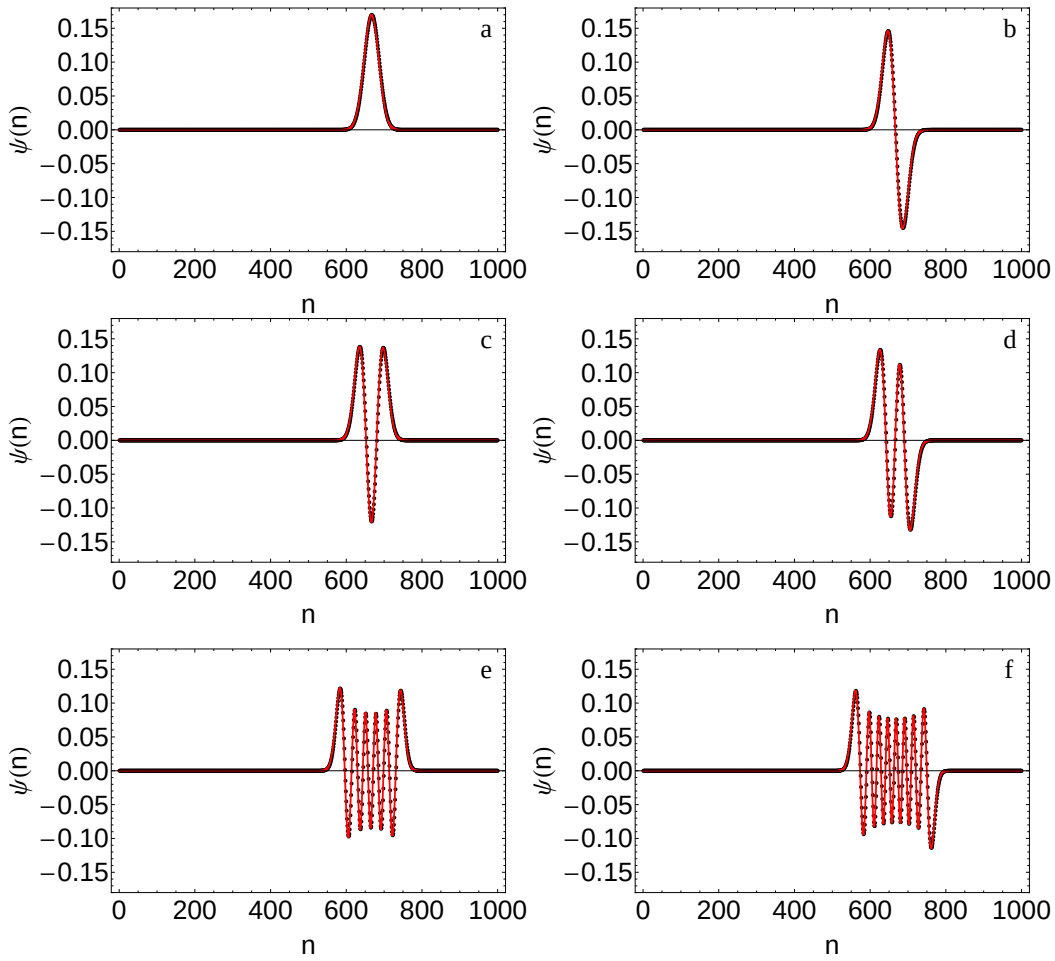

Figure 3.4: Normalized wavefunctions of the nanomagnet-cavity system consisting of 10^3 spins obtained from the exact solutions (*black, dotted*), and from the continuous WKB (*red, solid*) approximation are shown for the (a) ground state, and (b) 1^{st}, (c) 2^{nd}, (d) 3^{rd}, (e) 10^{th}, and (f) 15^{th} excited states.

constant of motion given as $\xi = 10^9/2$), some of the selected wavefunctions up to the 150^{th} excited state ($j = 150$) are shown in Fig 3.5.

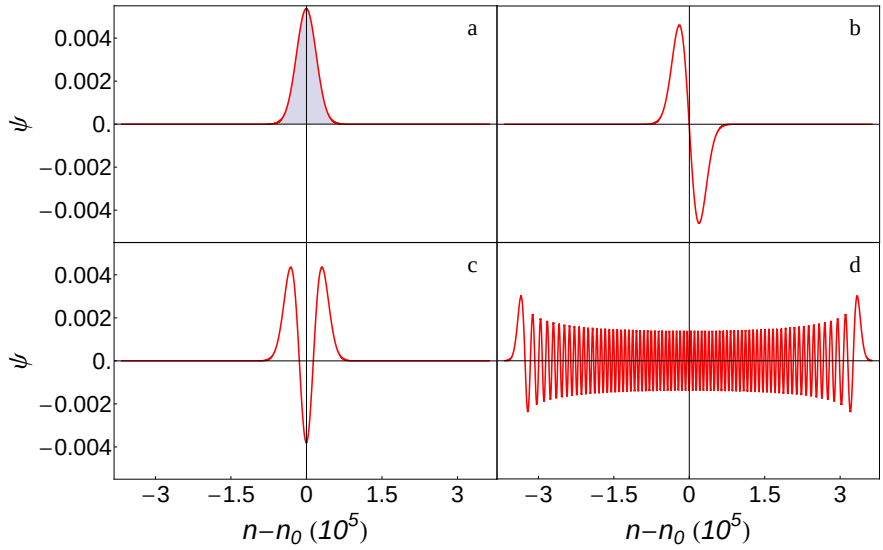

Figure 3.5: Some wavefunctions of the nanomagnet-cavity system are shown as a function of photon number, n, centered about the equilibrium point $n_0 = 4\xi/3 = 6.66667 \times 10^8$ for $N = 10^9$ spins: (a) ground state with a width of roughly 10^4 photons(spins), (b) 1^{st}, (c) 2^{nd}, and (d) 150^{th} excited states.

3.3 Coherent-State Representation

Quantum electrodynamics has historically been developed in terms of the stationary number states of the free-radiation field. Quantum numbers are typically large as well as uncertain in the classical limit of quantum electrodynamics, and therefore the photon number states are not a natural basis in this case. Coherent states were first discovered by Schrödinger, in connection with the quantum harmonic oscillator, and referred as states of minimum uncertainty product. Their usefulness remained hidden, until recent times when their properties were further investigated by Klauder. Later, Bargmann's introduction of a functional representation of quantum states leaded to many common features with the coherent-state representation. However, the

recognition of the coherent states as to be particularly important and appropriate for the quantum treatment of optical coherence is due largely to the work of Glauber [116], who has discussed quantum states forming an overcomplete set which are well suited to treatment of the classical region. The classical dispersion of these states in photon number is equal to the average photon number. It is interesting to see the same classical dispersion for most of the eigenstates of an N-molecule-radiation Hamiltonian.

3.3.1 Fock Representation of the Coherent State

Coherent states can be easily derived with the knowledge of that they are the eigenstates of the annihilation operator,

$$a|\alpha\rangle = \alpha|\alpha\rangle. \tag{3.31}$$

Because the annihilation operator a is not Hermitian, in general, its eigenvalue will be some complex number α; whereas the corresponding eigenstate, so-called coherent state, is represented by $|\alpha\rangle$. Since the Fock states form a complete set, they can be used to represent any coherent state, such as

$$|\alpha\rangle = \sum_{n=0}^{\infty} c_n|n\rangle, \tag{3.32}$$

where the c_n are complex numbers to be determined by substituting the coherent state given in Eq. (3.32) into the Eq. (3.31), i.e.

$$\sum_{n=1}^{\infty} c_n\sqrt{n}|n-1\rangle = \alpha\sum_{n=0}^{\infty} c_n|n\rangle. \tag{3.33}$$

Now this equation can be easily used to obtain the recursion relation for c_n by realizing that it can be satisfied only if the coefficients of corresponding Fock states on both sides are equal. Therefore, by equating the coefficients of $|n-1\rangle$, one can get the recursion relation connecting c_n and c_{n-1},

$$c_n = \frac{\alpha}{\sqrt{n}}c_{n-1}, \tag{3.34}$$

from which its repeated application yields to

$$c_n = \frac{\alpha}{\sqrt{n}} c_{n-1} = \frac{\alpha^2}{\sqrt{n(n-1)}} c_{n-2} = \ldots = \frac{\alpha^n}{\sqrt{n!}} c_0. \tag{3.35}$$

Hence, in terms of only one unknown coefficient, the Fock representation of the coherent state becomes

$$|\alpha\rangle = c_0 \sum_{n=0}^{\infty} \frac{\alpha^n}{\sqrt{n!}} |\alpha\rangle, \tag{3.36}$$

where c_0 can also be determined from the requirement of normalization of the coherent states which implies

$$\begin{aligned} \langle \alpha | \alpha \rangle = 1 &= |c_0|^2 \sum_{n=0}^{\infty} \sum_{m=0}^{\infty} \frac{\alpha^{*n} \alpha^m}{\sqrt{n!m!}} \langle n | m \rangle \\ &= |c_0|^2 e^{|\alpha|^2}. \end{aligned} \tag{3.37}$$

Therefore, the final form of the Fock representation of the coherent state becomes

$$|\alpha\rangle = e^{-\frac{|\alpha|^2}{2}} \sum_{n=0}^{\infty} \frac{\alpha^n}{\sqrt{n!}}. \tag{3.38}$$

It is important to note that for every complex number α other than zero, the coherent state $|\alpha\rangle$ has a non-zero projection, i.e.

$$\langle n | \alpha \rangle = e^{-\frac{|\alpha|^2}{2}} \frac{\alpha^n}{\sqrt{n!}}, \tag{3.39}$$

on every Fock state $|n\rangle$. When $\alpha = 0$, the coherent state $|\alpha\rangle$ becomes the vacuum state which may also be treated as a coherent state. The squared modulus of the projection of $|\alpha\rangle$ onto $|n\rangle$ gives the probability $p(n)$ that n photons will be found in the coherent state $|\alpha\rangle$. Note that, this probability given as

$$p(n) = |\langle n | \alpha \rangle|^2 = \frac{|\alpha|^{2n}}{n!} e^{-|\alpha|^2}, \tag{3.40}$$

can be recognized as a Poisson distribution with a parameter $|\alpha|^2$. Close observation of Eq. (3.38) reveals a remarkable feature of the coherent states that they are unchanged when acted on by the annihilation operator a. Therefore, a possible analogy between the coherent state of the quantum field and a classical field can be suggested by the fact that it is possible to absorb photons from an electromagnetic field in a coherent

state repeatedly, without effecting the state in any way. Even though coherent state is not an eigenstate of any observable, and therefore, misleadingly, it can be concluded that it does not correspond to any readily measurable feature of the field; in practice most measurements of the field are based on the process of photoelectric detection by using instruments such as the photomultiplier, the photoconductor, the photographic plate, and the eye, which all function by the absorption of photons. Since coherent states are the eigenstates of the absorption operator, these states prove to be the most convenient for the description of many properties of the field encountered in photoelectric measurements of the optical domain.

3.3.2 Coordinate Representation of the Coherent State

The coordinate representation $\phi_\alpha(x)$ of the coherent state $|\alpha\rangle$ can be directly evaluated from the matrix element $\langle x|\alpha\rangle$, where $|x\rangle$ is the eigenstate of the position operator $\hat{x}$. From Eq. (3.31), we have

$$\langle x|a|\alpha\rangle = \alpha\langle x|\alpha\rangle = \alpha\phi_\alpha(x). \tag{3.41}$$

Subtituting the annihilation operator s, given by

$$a(t) = \frac{1}{\sqrt{2\hbar\omega}}\left[\omega\hat{x}(t) + i\hat{p}(t)\right] \tag{3.42}$$

in terms of the position and momentum operator, into Eq. (3.41) yields to the following first-order differential equation

$$\frac{1}{\sqrt{2\hbar\omega}}\left[x\omega + \hbar\frac{\partial}{\partial x}\right]\phi_\alpha(x) = \alpha\phi_\alpha(x), \tag{3.43}$$

where momentum operator used in its differential form. The general solution can be written as

$$\phi_\alpha(x) = A\exp\left\{-\frac{\omega}{2\hbar}\left[x - \alpha\left(\frac{2\hbar}{\omega}\right)^{1/2}\right]^2\right\}, \tag{3.44}$$

where the normalization constant A can be determined from the normalization condition of the coherent state,

$$\int |\phi_\alpha(x)|^2 dx = 1, \tag{3.45}$$

to be

$$|A| = \left(\frac{\omega}{\pi\hbar}\right)^{1/4} e^{(\mathrm{Im}\alpha)^2}. \tag{3.46}$$

Therefore, the final form of the coordinate representation of the coherent state is given by

$$\phi_\alpha(x) = \left(\frac{\omega}{\pi\hbar}\right)^{1/4} e^{(\mathrm{Im}\alpha)^2} \exp\left\{-\frac{\omega}{2\hbar}\left[x - \alpha\left(\frac{2\hbar}{\omega}\right)^{1/2}\right]^2\right\}. \tag{3.47}$$

It can be easily seen that $\phi_\alpha(x)$ has the structure of a Gaussian function of x, in which the peak of the Gaussian is displaced by the distance $(2\hbar/\omega)^{1/2}\,\alpha$ from the origin. Since $\alpha = 0$ corresponds to the vacuum state, the coherent state appears as a displacement from the vacuum state.

3.3.3 Coherent State of the Spin-Cavity Hamiltonian

A coherent state of our spin-cavity system consisting of 10^9 spins, which is displaced by an amount of roughly $\approx 2.67 \times 10^5$ photons (or in otherwords spins) from its equulibrium point n_0 (or m_0), characterized by very large oscillations in photon numbers and spins with a period of T. As shown in the previous section, coherent states have the formal structure of a Gaussian function in coordinate representation, and they correspond to a displaced ground state of the eigensystem under consideration. The analytical form of the ground state of our spin-cavity system, shown in Fig 3.5a, can be expressed by a Gaussian function in the form of

$$\psi_0(x) = \frac{1}{\sigma\sqrt{2\pi}} e^{-(x-n_0)^2/2\sigma^2}, \tag{3.48}$$

where the standard deviation σ can be found by matching the values of the full width at half maximum (FWHM) of the ground state and the Gaussian function to each

other, i.e.

$$\text{FWHM}(\psi_0(x)) = 2\sqrt{2\ln 2}\sigma, \tag{3.49}$$

$$\psi_0(n_0) = \left(\sigma\sqrt{2\pi}\right)^{-1}. \tag{3.50}$$

This matching of the ground state, which numerically obtained by solving the differential equation given in Eq. (3.22), to the Gaussian function has been shown in Fig. 3.6 for the proposed nanomagnet-cavity system.

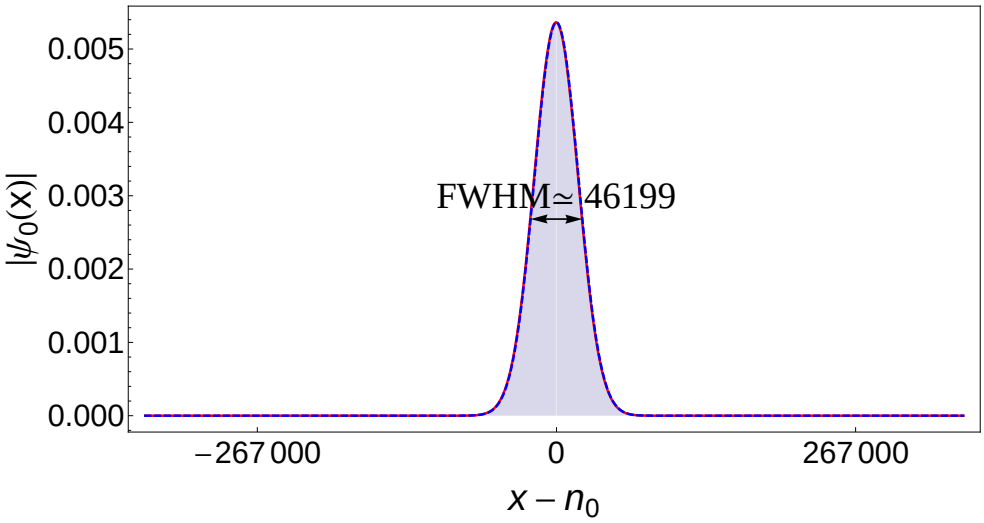

Figure 3.6: Matching between the Gaussian function with FWHM $\simeq$ 46199 (*Red*) and the ground state of the nanomagnet-cavity system centered at $n_0 = 6.67 \times 10^8$ (*Blue,dashed*) is shown with respect to photon number x of the cavity.

Expressing the ground state of the spin-cavity system in the form of a Gaussian function as in Eq. (3.48) allows us to easily obtain the displaced forms of this ground state as well,

$$\psi_0(x - x_0) = \psi_0(n_0)e^{-((x-x_0)-n_0)^2/2\sigma^2}. \tag{3.51}$$

Since each different displacement of the ground state of the eigensystem given by a distance $(2\hbar/\omega)^{1/2}\,\alpha$ corresponds to a different coherent state of that eigensystem, it

is allowed to define any coherent state of the spin-cavity system as

$$\phi(x,t_0) = \psi_0(x-x_0) = \psi_0(n_0)e^{-(x-x_0-n_0)^2/2\sigma^2}, \tag{3.52}$$

initialized at time t_0. Moreover, since the eigenfunctions of the spin-cavity system spans a complete orthogonal space, they can be used as basis functions to expand any coherent state over,

$$\phi(x,t-t_0) = \sum_{j=0}^{\infty} A_j e^{-iE_j(t-t_0)/\hbar}\psi_j(x), \tag{3.53}$$

for any given time t. Equating the relations given in Eq. (3.53) and Eq. (3.52) at an initial time $t = t_0$ leads to the following equation:

$$\sum_{j=0}^{\infty} A_j\psi_j(x) = \psi_0(n_0)e^{-(x-x_0-n_0)^2/2\sigma^2}. \tag{3.54}$$

Multiplying both sides of the Eq. (3.54) with $\psi_{j'}$ and integrating over the region $[0, 2\xi]$,

$$\sum_{j=0}^{\infty} A_j \int_0^{2\xi} \psi_j(x)\psi_{j'}(x)dx = \psi_0(n_0)\int_0^{2\xi} \psi_{j'}(x)e^{-(x-x_0-n_0)^2/2\sigma^2}dx, \tag{3.55}$$

$$A_j = \psi_0(n_0)\int_0^{2\xi} \psi_j(x)e^{-(x-x_0-n_0)^2/2\sigma^2}dx, \tag{3.56}$$

reveals the phase constants A_j of the expansion given in Eq. (3.53). Note that the integration on the lhs of Eq. (3.55) has been evaluated by using the orthonormality condition of the spin-cavity wavefunctions.

In conclusion, any coherent state of the spin-cavity system initially centered at x_0 can be expanded in terms of the eigenfunctions of the spin-cavity system, whereas the coefficients of the expansion are evaluated by using the relation given in Eq. (3.56). Moreover, as demonstrated in Fig. 3.7, time evolution of any coherent state of the spin-cavity system reveals a very large oscillation in photon numbers (in otherwords spins) roughly $\sim 5.34 \times 10^5$ photons or spins for the nanomagnet consisting of $N = 10^9$ spins. The Zeeman energy of the nanomagnet and transverse magnetic field strength of the cavity can be evaluated as $\langle \Delta E_z \rangle = \langle \phi(t)|\mu_z B_0|\phi(t)\rangle$ and $\langle B_T - B_{T_0}\rangle = \langle \phi(t)|\boldsymbol{H}_{TM}(d)|\phi(t)\rangle$, respectively, by using the coherent state representation of the spin-cavity system. Collective oscillations of these quantities

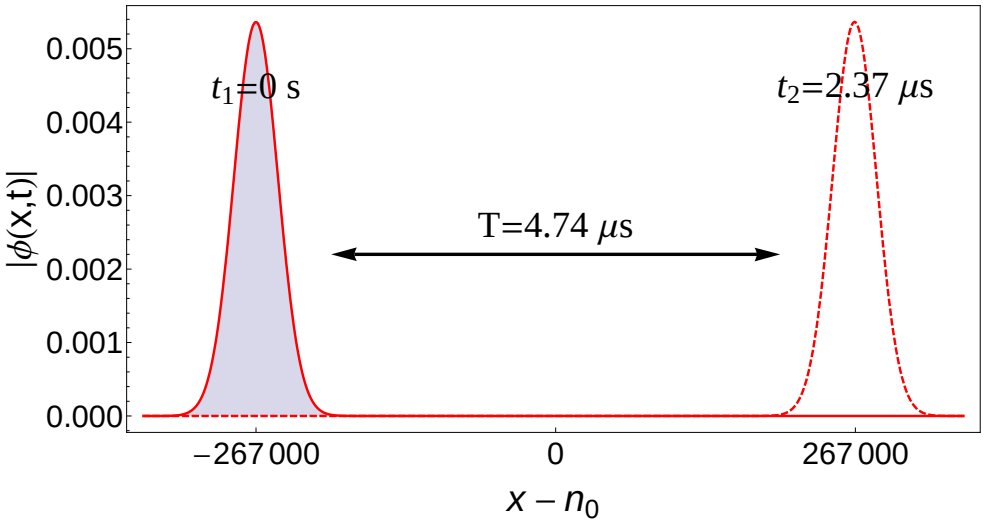

Figure 3.7: Amplitude of the coherent state of the nanomagnet-cavity system is shown as a function of photon number $x - n_0$ at times $t = 0$, and $t = 2.37$ μs. The large oscillations of this coherent state about $n_0 = 6.667 \times 10^8$ occurs between -267000 (*Filled*), and 267000 (*Dashed*) in photon numbers with a period of $T = 4.74$ μs.

shown in Fig. 3.8 corresponds to the coherent energy exchange occuring back and forth between photons of the cavity and the spins of the nanomagnet.

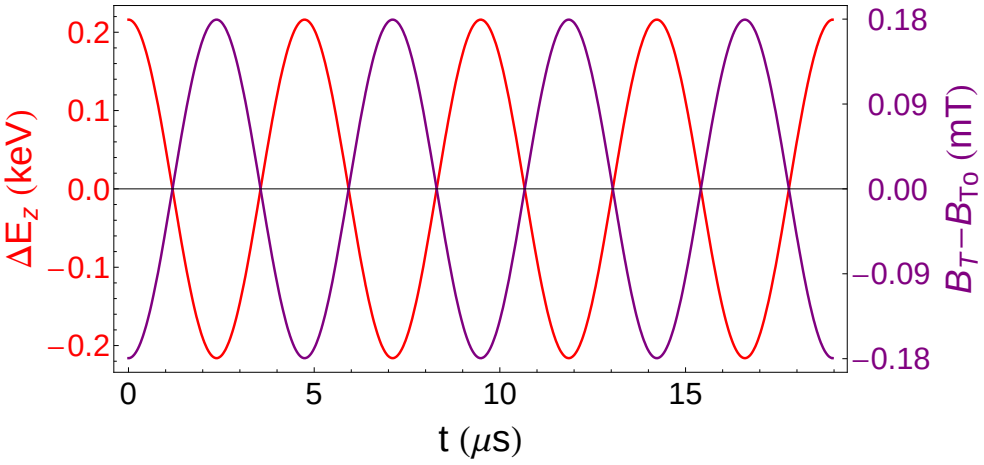

Figure 3.8: Time evolution of the Zeeman energy of the nanomagnet (*Red*), and the amplitude of the transverse magnetic cavity field for the TM mode (*Purple*) are shown in the coherent representation of the spin-cavity system.

Certain autocorrelation function, shown in Fig. 3.9, between the initial coherent state $|\phi(0)\rangle$ and the coherent state at any given time $|\phi(t)\rangle$, defined by

$$P(t) = |\langle\phi(t)|\phi(0)\rangle|^2, \tag{3.57}$$

can be used to extract the period of the coherent state oscillation T as following:

$$\begin{aligned} P(T) &= \left| \int_0^{2\xi} \sum_{j,j'=0}^{\infty} A_j^* A_{j'} \psi_j^*(x) \psi_{j'}(x) e^{iE_j T/\hbar} dx \right|^2, \\ &= \left| \sum_{j,j'=0}^{\infty} A_j^* A_{j'} e^{iE_j T/\hbar} \int_0^{2\xi} \psi_j^*(x) \psi_{j'}(x) dx \right|^2, \\ &= \left| \sum_{j,j'=0}^{\infty} A_j^* A_{j'} e^{iE_j T/\hbar} \delta_{j,j'} \right|^2, \\ &= \left| \sum_{j=0}^{\infty} |A_j|^2 e^{iE_j T/\hbar} \right|^2 = 1. \end{aligned} \tag{3.58}$$

by finding the root T satisfying Eq. (3.58). Hence, for the nanomagnet possessing 10^9 spins, the period of the coherent state oscillation is obtained as $T = 4.74$ μs for the spin-cavity system. Moreover, as an important measure of quantum coherence, phase fluctuation (dephasing) of the coherent state obtained from the auto-correlation function for large time scales is shown in Fig. 3.10 to be exceptionally large in order of few seconds.

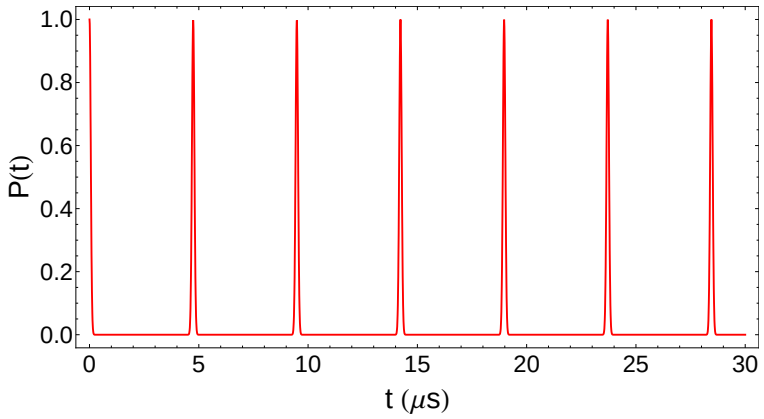

Figure 3.9: Autocorrelation function between the initial coherent state $|\phi(0)\rangle$ and the coherent state at any given time $|\phi(t)\rangle$, defined as $P(t) = |\langle\phi(t)|\phi(0)\rangle|^2$, is shown as a function of time t.

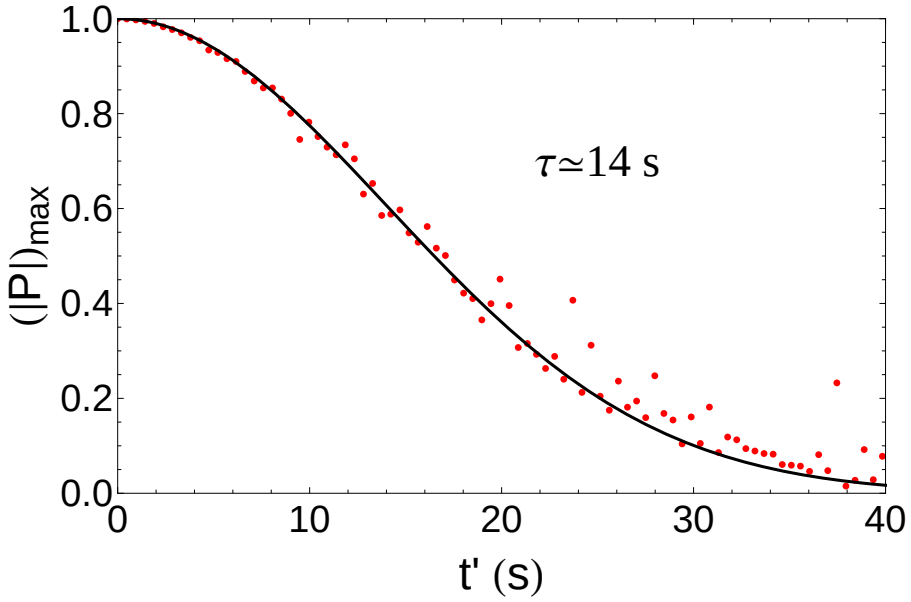

Figure 3.10: Dephasing time of the coherent state is obtained by the Gaussian fit of e^{-t^2/τ^2} to the peak values of the auto-correlation function at successive time intervals.

CHAPTER 4
DECOHERENCE MECHANISMS

4.1 Elementary Excitation of Magnons

Although this treatment is for zero temperature, the coherent properties of the nanomagnet-photon system should persist to as high a temperature (and over as long a timescale) as the macrospin description remains reliable. Since an infinite Q assumed for the cavity, the decoherence of the system is expected to be determined by photon leakage from the cavity, rather than those exceptionally long dephasing times. The validity of the macrospin approximation for the nanomagnet consisting of iron (Fe) atoms can be tested by using the magnon description given in Section 1.3.1. The number of magnons excited is given by

$$\begin{aligned} N_m &= \sum_{\boldsymbol{k}} \frac{1}{\exp(\hbar\omega_{\boldsymbol{k}}/k_BT)-1}, \\ &\int g(\omega)\frac{1}{\exp(\hbar\omega_{\boldsymbol{k}}/k_BT)-1}d\omega, \end{aligned} \tag{4.1}$$

where $g(\omega)$ corresponds to density of states,

$$g(\omega) = n(k)\frac{dk}{d\omega} = \frac{V}{2\pi^2}k^2\frac{dk}{d\omega}. \tag{4.2}$$

Note that the $\gamma_{\boldsymbol{k}}$ given in the dispersion relation of magnons in Eq. (1.97) depends on the crystal structure, and for a bcc Fe crystal structure it can be estimated as

$$\begin{aligned} \gamma_{\boldsymbol{k}} &= \frac{1}{\nu}\sum_{\delta}\exp\left(i\boldsymbol{k}\cdot\boldsymbol{R}_\delta\right) \\ &= \frac{1}{8}\sum\cos(\pm\frac{k_xa}{2}\pm\frac{k_ya}{2}\pm\frac{k_za}{2}) \\ &\approx 1-\frac{a^2k^2}{4}, \end{aligned} \tag{4.3}$$

for small k, resulting with the dispersion relation of

$$\hbar\omega = 4Jk^2a^2. \tag{4.4}$$

Hence the density of states becomes

$$g(\omega) = \frac{V_N}{4\pi^2}\left(\frac{\hbar}{4Ja^2}\right)^{3/2}\omega^{1/2}. \tag{4.5}$$

Finally, the number of magnons excited in the nanomagnet is

$$\begin{aligned} N_m &= \frac{V_N}{4\pi^2}\left(\frac{\hbar}{4Ja^2}\right)^{3/2}\int_0^\infty \frac{\omega^{1/2}}{\exp(\hbar\omega/k_BT)-1}d\omega \\ &= \frac{V_N}{4\pi^2}\left(\frac{\hbar}{4Ja^2}\right)^{3/2}\left(\frac{k_BT}{\hbar}\right)^{3/2}\int_0^\infty \frac{x^{1/2}}{e^x-1}d\omega \\ &= 2.32\frac{V_N}{4\pi^2}\left(\frac{k_B}{4Ja^2}\right)^{3/2}T^{3/2}, \end{aligned} \tag{4.6}$$

where the exchange integral and lattice parameter for Fe are given by $J = 11.9$ meV and $a = 2.87$ Åwith $\nu = 8$ nearest neighbor atoms with spin $s = 1$, respectively.

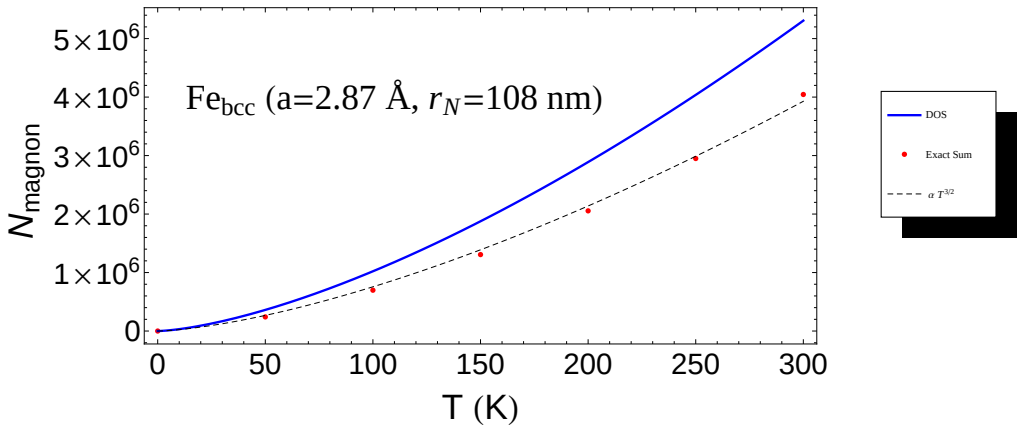

Figure 4.1: Temperature dependence of magnon numbers is shown by using density of states approach (*Blue*) and exact summation (*Red*) over all possible $\boldsymbol{k}$'s for the size of the nanomagnet in consideration. Fitting of a function in the form of $\alpha T^{3/2}$ to the exact summation data yields to the expected temperature behavior of magnons with $\alpha \approx 756$ K$^{-3/2}$.

For a spherical nanomagnet with a radius of $r_0 = 108$ nm, the temperature dependence of the number of magnons excited is evaluated and shown in Fig 4.1 by using the density of states approach mentioned above and also with a more direct approach using the exact summation over every $\boldsymbol{k}$. Note that the expected $\alpha T^{3/2}$

behavior for magnons are also applied with a fit to the exact summation case, yielding a value of $\alpha \approx 756\ \mathrm{K}^{-3/2}$. Even though there are large number of magnons excited in the system, the macrospin approach still proves to be a valid approximation. This can be easily realized by considering that each magnon excited in the system reduces the total magnetic moment in the amount of $2.21\mu_B$ for Fe. Note that the total z component of the magnetic moment μ_z is given by

$$\mu_z = M_s(0)V - g\mu_B \sum_k n_k \tag{4.7}$$

where n_k is the number of magnons with wavevector k and $M_s(0)$ is the saturation magnetization at $T = 0$, in which $M_s(0)V$ is the maximum possible value of M_s attained when all the spins are parallel along the z-direction of the static field. For the spherical nanomagnet in consideration, there are roughly $n_{Fe} = 4.5 \times 10^8$ Fe atoms present with a total magnetic moment of $\boldsymbol{\mu} \approx 2.21\mu_B n_{Fe}$. Therefore, as shown in Fig. 4.2, the reduction of the total magnetic moment of the system due to the magnon excitation will be only 0.87% at room temperature ($T = 300$ K).

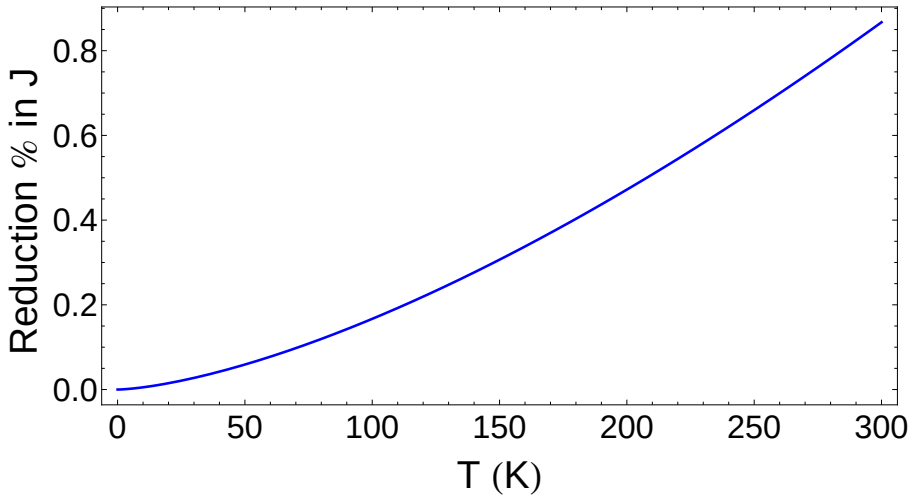

Figure 4.2: Due to the calculated number of magnons N_m excited in the spin system, the reduction percentage of the total magnetic moment $\boldsymbol{J}$ is shown with respect to temperature T.

Furthermore, the elementary spin excitations (magnons) would not directly affect the dephasing of the system, for magnons preserve the spin quantum number m_s, requiring an up spin to flip down for every down spin flipping up. In realistic nanomagnets, spin-lattice coupling of m_s to phonons through spin-orbit coupling will cause a cutoff of the dephasing times shown in Fig. 3.10 [117–121]. For spheres of yttrium iron garnet (YIG) at low temperature, this spin-lattice time is several μs [122, 123] comparable with the period of the coherent oscillation ($T = 4.74$ μs) as shown in Fig. 3.7, therefore, permitting observation of a full oscillation cycle. The times at room temperature in YIG (~ 200 ns [122]) and iron (~ 20 ns [124, 125]) are too small to observe a full oscillation; however, coherent dynamics corresponding to a portion of the oscillation involving ~ 220 photons/ns, or ~ 4400 photons for iron and $\sim 4.4 \times 10^4$ photons for YIG should be still observable.

4.2 Magnetocrystalline Anisotropy

The energy in a ferromagnetic cyrstal which directs the magnetization along certain crystallographic axes is called magnetocrystalline or anisotropy energy, where these axes are also called directions of easy magnetization. Since magnetocrystalline anisotropy (MA) arises from the spin-orbit coupling between the spins and the lattice of the cyrstal, it needs to be calculated from the electronic structure of the material. One of the main mechanisms behind MA is the asymmetry of the overlap of electron distributions on neighboring ions. Due to spin-orbit interaction, the charge distribution is spheroidal instead of spherical. This asymmetry is directly related to the direction of spin such that a rotation of the spin directions relative to the crystal axes changes the exchange energy and also changes the electrostatic interaction energy of the charge distributions on pairs of atoms, where both effects give rise to the MA energy. Two different energy configurations of this type are shown in Fig. 4.3.

The most common anisotropy effect is connected to the existence of only one easy direction and it is called uniaxial anisotropy. In this type of anisotropy, since the free

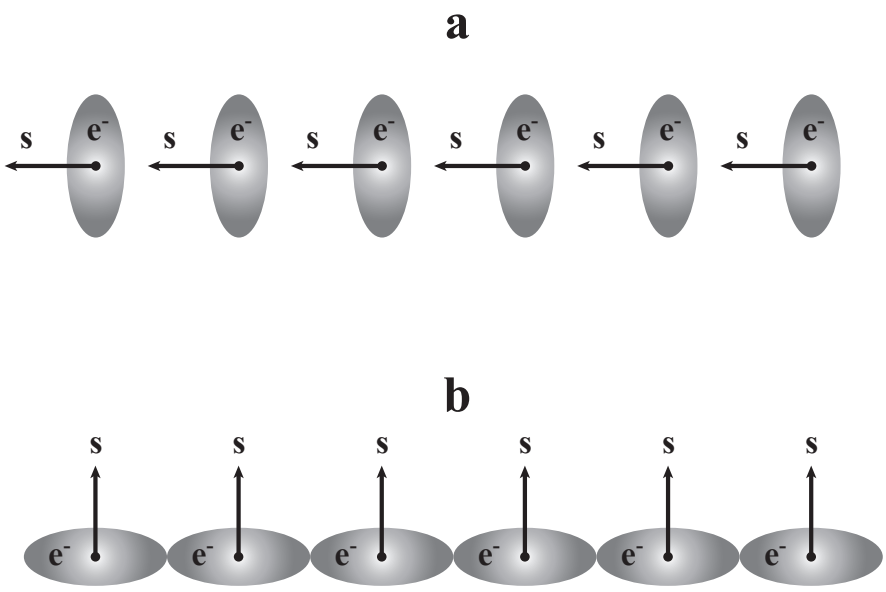

Figure 4.3: Spheroidal charge distribution and the relative spin directions is shown in two different type of configurations. The energy of (a) is different than the energy of (b) due to spin-orbit interactions.

energy density is rotationally-symmetric with respect to the easy axis, it only depends on the relative direction of spin $\boldsymbol{s}$ with respect to this axis. Due to this symmetry restrictions, assuming z-axis is chosen along the easy axis, uniaxial anisotropy energy density can be expanded as an even function of $\boldsymbol{s}_z \sim \cos\theta$. Therefore, the uniaxial anisotropy energy density is given by

$$E_{UA} = K_1' \sin^2\theta + K_2' \sin^4\theta, \tag{4.8}$$

up to second order by anisotropy constants K_1' and K_2'. A hexagonal crystal Cobalt (Co) is one of the most well-known examples of this type of anisotropy. In case of Co, since the hexagonal axis is along the direction of easy magnetization θ corresponds to the angle the magnetization makes with the hexagonal axis, and the anisotropy constants are given by $K_1' = 4.1 \times 10^6$ erg/cm^3 and $K_2' = 1.0 \times 10^6$ erg/cm^3 at room temperature.

Magnetic anisotropy caused by magnetocrystalline sources can lead to several easy

axes, depending on the symmetry of the given crystal structure. In the case of cubic crystal whose easy axis is aligned along the body diagonal, arbitrary magnetization direction is defined by direction cosines α_1,α_2,α_3 referred to the cube edges. Since opposite ends of a crystal axis are magnetically equivalent the cubic anisotropy energy density should be an even power of each α_i and it should be invariant under the interchanges of any α_i. Even though the lowest order combination satisfying the symmetry requirements is given by $\alpha_1^2+\alpha_2^2+\alpha_3^2$, since it identically yields to unity, it does not describe the cubic anisotropy energy. However, the next fourth and sixth order combinations is enough to define the cubic anisotropy as following

$$E_{CMA} = K_1\left(\alpha_1^2\alpha_2^2+\alpha_2^2\alpha_3^2+\alpha_1^2\alpha_3^2\right)+K_2\alpha_1^2\alpha_2^2\alpha_3^2, \tag{4.9}$$

where the cubic anisotropy constants are given by K_1 and K_2. Since iron (Fe) has a body centered cubic crystal structure, it possesses an anisotropy of this type, and its anisotropy constants are given by $K_1' = 4.2\times10^5$ erg/cm^3 and $K_2' = 1.5\times10^5$ erg/cm^3 at room temperature.

The crystalline magnetic anisotropy (CMA) of iron (Fe) causes a detuning of the energy spacing for different spin orientations from the resonant frequency of the cavity, along with a dispersion in that spacing. The uniform detuning, corresponding to a uniform shift in the precession frequency of the nanomagnet spin, can be compensated for with a slight adjustment in the applied magnetic field. Note that CMA energy defined as

$$E_{CMA} = K_1\left(\frac{\xi^4-3m^4+2\xi^2m^2}{4\xi^4}\right)+K_2\left(\frac{\xi^4m^2-2\xi^2m^4+m^6}{\xi^6}\right), \tag{4.10}$$

in terms of the spin m, where directional cosines are estimated as

$$\begin{aligned}\alpha_1^2 &= \alpha_2^2 = \frac{\xi^2-m^2}{2\xi^2},\\ \alpha_3^2 &= \frac{m^2}{\xi^2}.\end{aligned} \tag{4.11}$$

Therefore, obtaining a realistic picture of the nanomagnet-cavity system requires

the consideration of CMA. The dispersion causes a detuning of roughly 0.3 neV for the oscillation region of the coherent state shown in Fig. 3.7. Since this detuning is much smaller than magnet-photon coupling strength ($\tau(n_0) = 0.16$ eV) around the superradiance regime, it will not destroy the coherence.

4.3 Effects of the Nanomagnet Size

The coherent dynamics of a coupled photonic cavity and a nanomagnet is also explored for three different nanomagnet sizes of radius $r_0 \simeq 2.3$nm, 11nm, and 50nm corresponding total number of spins $N = 10^4$, 10^6, and 10^8, respectively. Therefore, the solutions of the nanomagnet-cavity Hamiltonian corresponds to the diagonalization of large matrices in the form of Eq. (3.6) with increasing ranks of 10^4, 10^6, and 10^8 and are shown in Fig. 4.4.

For three sizes of the nanomagnet, the coherent states shown in Fig. 4.5(a)-(c), are characterized by large oscillations over ranges of ($2x_0$=) 1780, 1.76×10^4, and 1.76×10^5 photons with periods of $T = 1.5$ ms, $T = 150$ μs, and $T = 15$ μs, respectively. The Zeeman energy of the nanomagnet ΔE_z and transverse magnetic field amplitude of the cavity B_T at the nanomagnet's location can also be evaluated from

$$\begin{aligned} \langle \Delta E_z \rangle &= \langle \phi(x,t) | \mu_z B_0 | \phi(x,t) \rangle, \\ \langle B_T \rangle &= \langle \phi(x,t) | \boldsymbol{H}_{TM}(d) | \phi(x,t) \rangle, \end{aligned} \tag{4.12}$$

by using these coherent state representation. Large oscillations of these quantities shown in Fig. 4.6 indicates the coherent energy exchange occuring back and forth between photons in the cavity and the spin states of the nanomagnets.

The coherent properties of these nanomagnet-photon systems will also depend on the dephasing of the coherent state $\phi(x,t)$, due to inhomogenity of the coupling $\tau(n)$. The dephasing time of the nanomagnet-cavity coherent states can be extracted by a Gaussian fit to the peak values of the autocorrelation function between a coherent

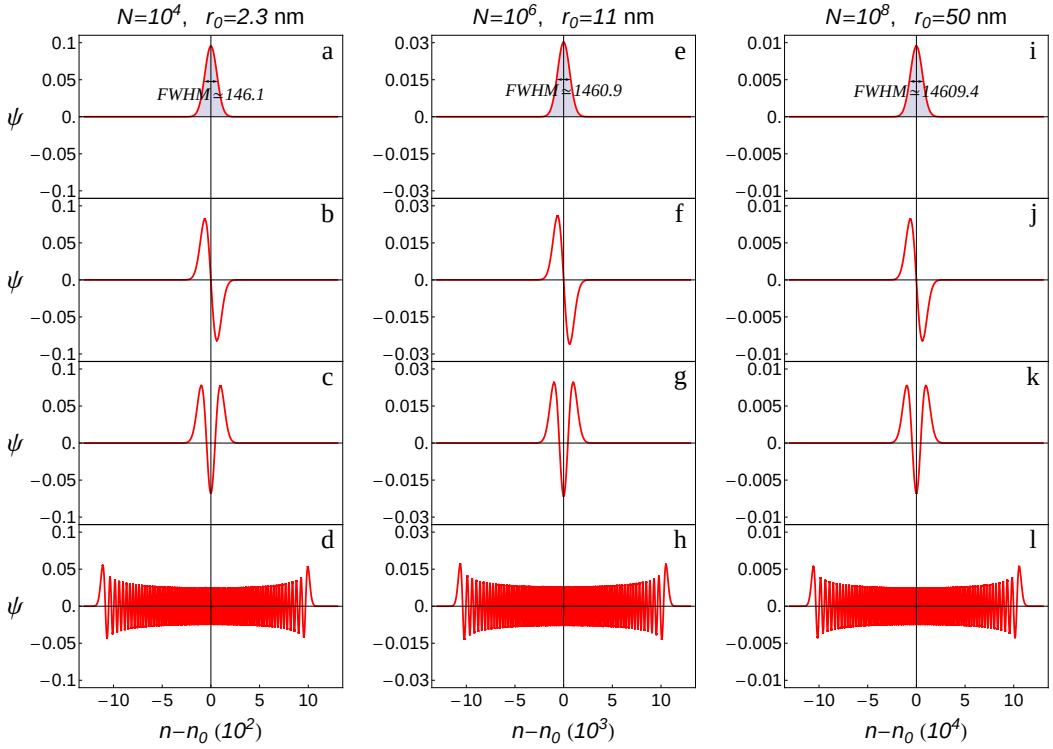

Figure 4.4: Wave functions of the nanomagnet-cavity system shown as a function of photon number, n, centered about n_0, for nanomagnets of radius $r_0 = 2.3, 11, 50$ nm, consisting of $N = 10^4$, $N = 10^6$, and $N = 10^8$ spins respectively. First row (a)-(e)-(i) are the ground states with a full width half maximum (FWHM) represented in photon numbers, second row (b)-(f)-(j) are the first excited states, third row (c)-(g)-(k) are the second excited states, and the fourth row (d)-(h)-(l) are the 150^{th} excited states.

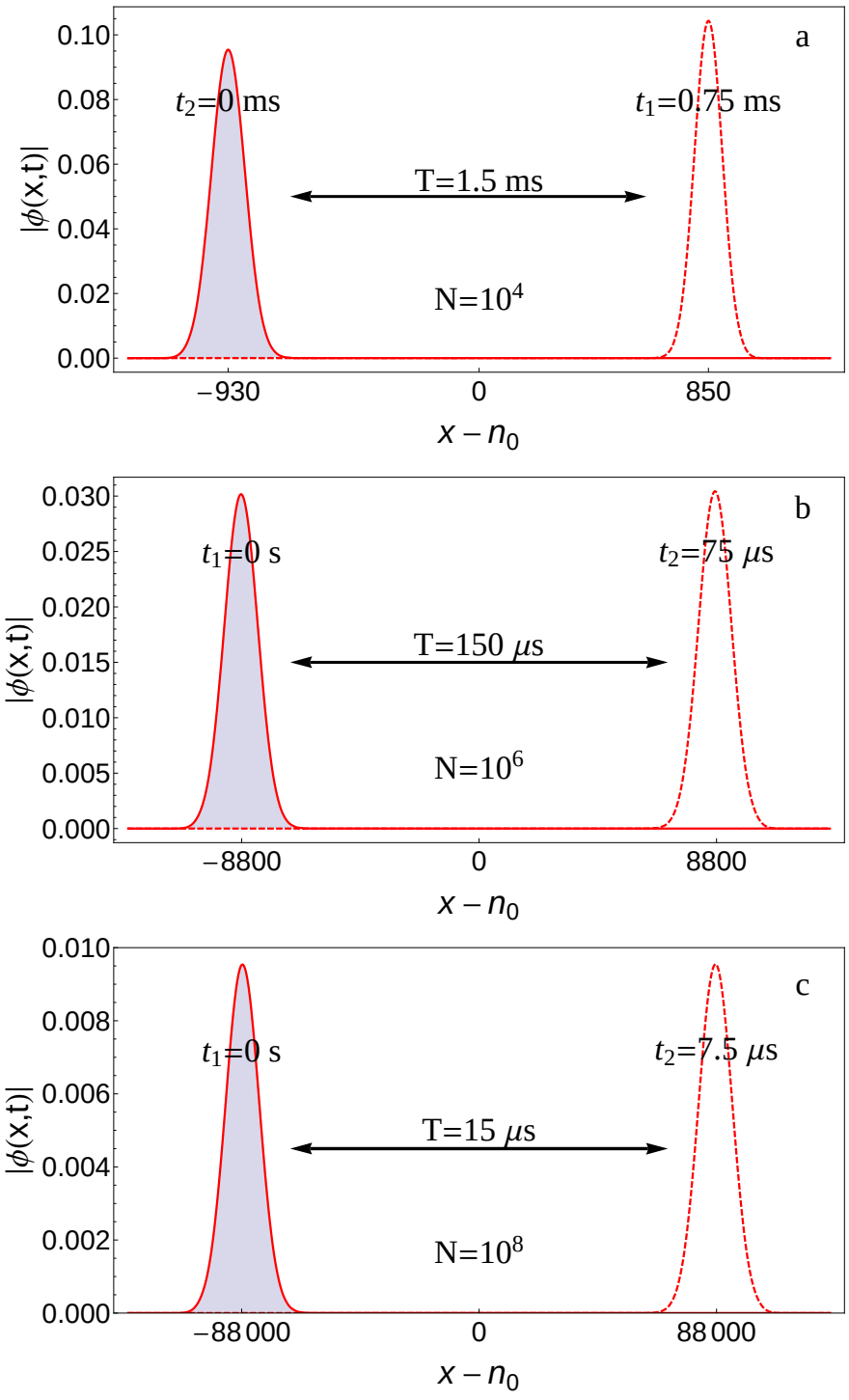

Figure 4.5: Amplitude of a coherent state for 3 different nanomagnet-photon systems consisting of (a) $N = 10^4$, (b) $N = 10^6$, and (c) $N = 10^8$ spins are shown as a function of photon number n. The large oscillations of these coherent states occur about (a) $n_0 \sim 6666$ with a period of $T = 1.5ms$, (b) $n_0 \sim 6.66 \times 10^5$ with a period of $T = 150\mu s$, and (c) $n_0 \sim 6.66 \times 10^7$ with a period of $T = 15\mu s$, respectively.

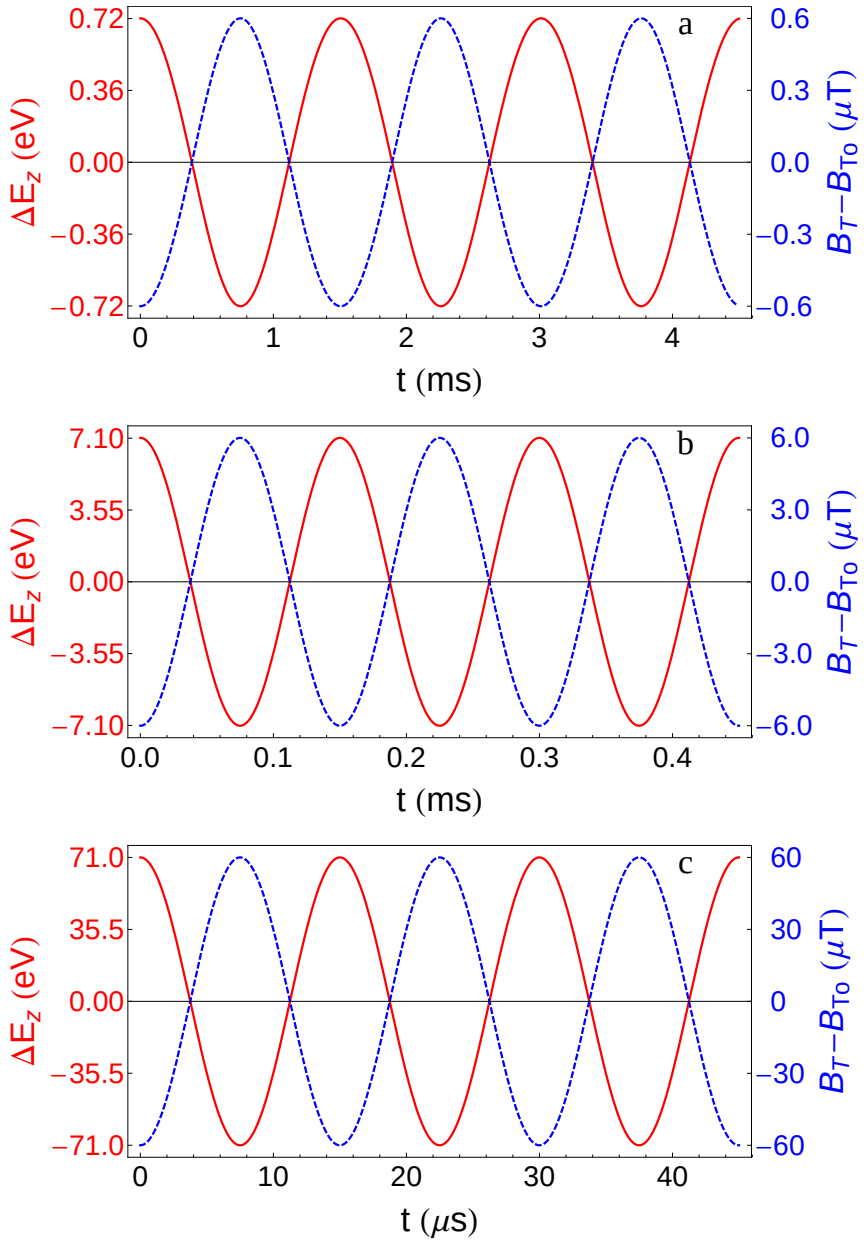

Figure 4.6: Time evolution of the Zeeman energy of the nanomagnets (*red*, *solid*) consisting of (a) $N = 10^4$, (b) $N = 10^6$, and (c) $N = 10^8$ spins are shown in coherent state representation as well as the amplitude of the transverse magnetic mode of the cavity field (*blue*, *dashed*) at nanomagnet location $z = d$.

state at time t and its initial state at $t = 0$,

$$\begin{aligned} P(t) &= |\langle\phi(x,t)|\phi(x,0)\rangle|^2, \\ &= \left|\sum_{j=0}^{\infty} |A_j|^2 e^{iE_j t/\hbar}\right|^2, \end{aligned} \tag{4.13}$$

whereas each peak (inset of Fig. 4.7) is representing the revival amount of the coherent state after every successful period T of oscillation. Exceptionally long dephasing time of order seconds are shown in Fig. 4.7. As the nanomagnet gets bigger the change in $\tau(n)$ with n becomes smoother and smoother, leading to longer dephasing times.

For spheres of yttrium iron garnet (YIG) at low temperature the spin-lattice time is several μs [122, 123, 126, 127]. Therefore, observation of a full oscillation cycle should be possible for nanomagnets with a radius of 50 nm or larger. On the other hand, the times at room temperature in YIG (~ 200) ns [122] and iron (~ 20 ns) [124] are too small to observe a full oscillation. However, coherent dynamics corresponding to a portion of the oscillation involving ~ 24 photons/ns, or ~ 470 photons for iron and 4700 photons for YIG should be still observable for the nanomagnet with radius $r_0 = 50$ nm. If, however, the modal coupling is increased using approaches such as tip-enhancement of the optical field, then the coupling could be far stronger even for a small nanomagnet. Guided by estimates from tip-enhanced Raman spectroscopy [128], the intensity of the mode at the nanomagnet's position could be increased by $10^2 - 10^6$, leading to enhancements of the oscillation frequency of order $10 - 10^3$.

Similar to the work presented in Section 4.2, the dispersion as a result of CMA causes a variable detuning of roughly 200 neV, 13 neV, and 1.3 neV of the E_0 in Eq. (3.4) over the range of oscillation shown in Fig. 4.5(a)-(c), respectively. For the smallest nanomagnets the effect of CMA dominates over the coupling between the photons and the spin. For example, for a nanomagnet radius of 2 nm consisting of 10^4 total spins, the CMA is significantly larger than the magnet-photon coupling strength $\tau(n_0)$ (~ 5.3 neV) as shown in Table 4.1. Therefore the CMA will cause

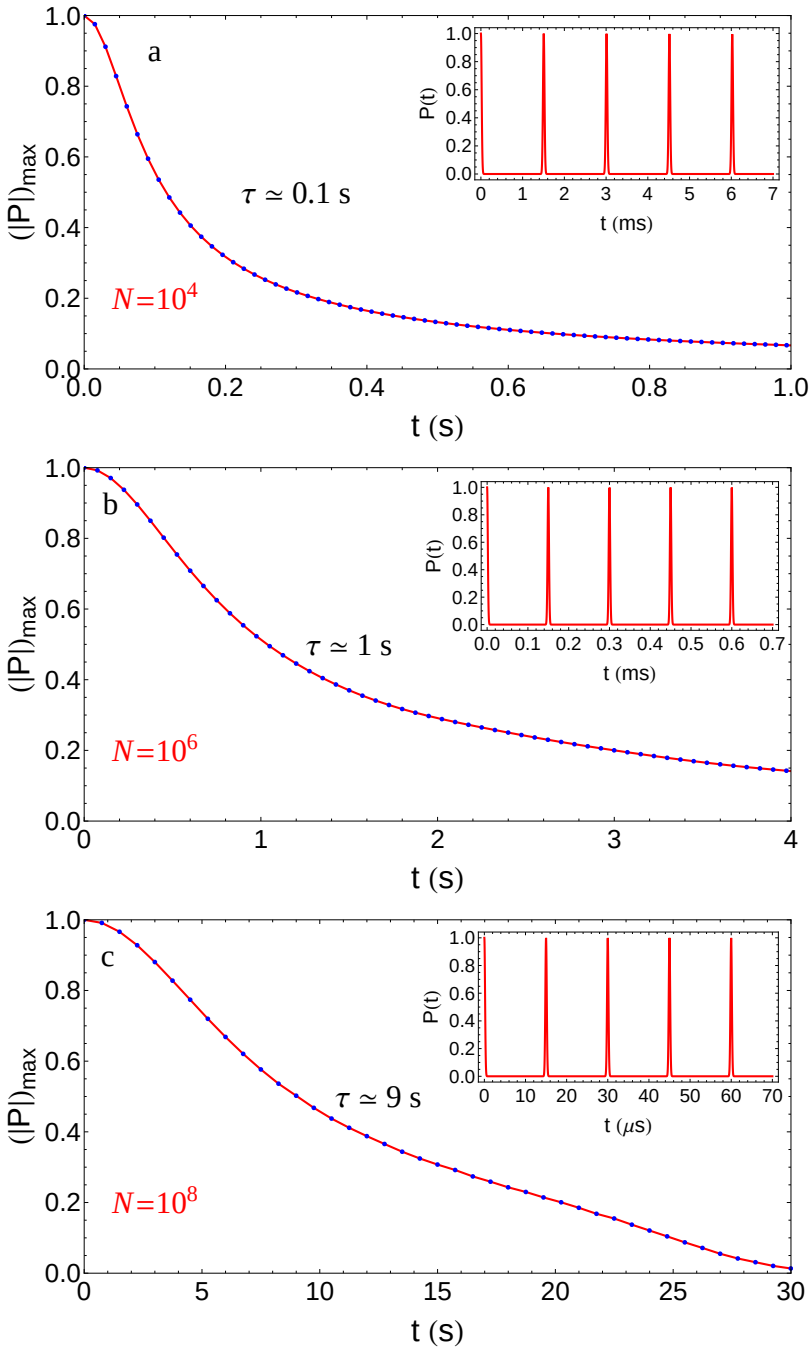

Figure 4.7: Dephasing time of the coherent state for nanomagnet-photon systems of (a) $N = 10^4$, (b) $N = 10^6$, and (c) $N = 10^8$ spins (or equivalently photons) obtained by a Gaussian fit to the peak values of the dephasing functions (insets) at successive time intervals. Each peak value represents the amount of correlation after every full period T of oscillation.

the eigenstates to localize in photon and spin number, producing rapid decoherence for a coherent state. We note that this observation largely rules out the possibility of observing these coherent oscillations in a single molecular magnet [129], for the spins of these molecules are considerably smaller than the spin of the nanomagnet considered above. However, this detuning is much smaller than the magnet-photon coupling strength of other nanomagnet sizes (10 nm and 50 nm in radii) and therefore will not destroy the coherent oscillations for them, although it may still limit the dephasing times to shorter than that shown in Fig. 4.7(b)-(c).

r_0	2.3 nm	11 nm	50 nm	100 nm
N	10^4	10^6	10^8	10^9
E_{CMA}	200 neV	13 neV	1.3 neV	0.3 neV
$\tau(n_0)$	5.3 neV	5.3 μeV	5.3 meV	0.16 eV

Table 4.1: Crystalline magnetic anisotropy energies E_{CMA} for different nanomagnet sizes (with radii r_0 and consisting of N spins) are shown in comparison with the magnet-photon coupling strength at the superradiance regime ($\tau(n_0)$).

As a result, calculations for three different nanomagnet sizes in a photonic cavity indicate that strong-field coupling between photons and spins is possible, and should substantially exceed the coupling observed in solids between orbital transitions and light. This coherent state is characterized by large oscillations in photon number of the cavity (or equivalently the total spin number of the nanomagnet) with exceptionally long dephasing times and is expected to be observable for realistic nanomagnets with radii from $10 - 50$ nm. Approaches to enhance the coupling, such as using a metal tip to enhance the optical field, have been proposed. For the smallest nanomagnet (2 nm radius) the dispersion caused by crystalline magnetic anisotropy would largely

quench the coherent oscillations, but for nanomagnets in the $10 - 50$ nm radius range the coupling to the cavity is much stronger than the dispersion caused by CMA. The dephasing times increase with increasing nanomagnet size, due to the greater uniformity of the coupling terms between states that differ by one photon and one spin flip. Thus the most coherent nanomagnet-cavity systems will be those that are just under the size threshold where the macrospin approximation ceases to be accurate.

CHAPTER 5
PHASE-LOCKING OF LIGHT AND SPIN COHERENT STATES

Phase-locking of coupled oscillators [130] is a well-known phenomenon in nonlinear dynamics, i.e. coherent radiation from Josephson junction arrays [131] as well as in quantum systems in the forms of Bose-Einstein condensation (BEC) (responsible for superfluidity and superconductivity) and lasing. Electromagnetic field quanta in an optical cavity containing a dielectric is called a cavity polariton [132, 133] different than its confined version (bulk polariton) [134]. Since polaritons are simply photons coupled to other excitations which are bosons, they might be considered as candidates for Bose condensation. Polariton condensate is a superposition of coherent states of the dielectric and the electromagnetic field coupled by the dipole interaction which is responsible for the phase locking. When all the oscillators with a finite polarization are mutually coherent, the energy will be minimized. Phase-locking using the Josephson junction array in a microcavity has been also considered [135] and it is in principle comparable to phase locking of cavity polaritons. Moreover, the laser and the polariton condensate are usually studied in seperate context, and the connection between them is usually not quite clear even though both can be described by exactly the same Hamiltonian. However, for a conventional laser the only significant ordering is the coherence of the photons, whereas in the polariton condensate both the photons and the excitons are coherent [136].

5.1 Coherent States of Light and Spin

In the most general sense, the coherent state of the radiation field $|\alpha\rangle$ is defined as a state of the field generated by a clasically oscillating current distribution, meaning the current can be described by a prescribed vector $\boldsymbol{J}(\boldsymbol{r}, t)$ which is not an operator. The same result can also be obtained by defining the coherent state as an eigenstate of the annihilation operator a with an eigenvalue α,

$$a|\alpha\rangle = \alpha|\alpha\rangle. \tag{5.1}$$

Therefore, an expression of $|\alpha\rangle$ in terms of Fock number state is given by

$$|\alpha\rangle = e^{-|\alpha|^2/2} \sum_{n=0}^{\infty} \frac{\alpha^n}{\sqrt{n!}} |n\rangle, \tag{5.2}$$

and since

$$|n\rangle = \frac{(a^\dagger)^n}{\sqrt{n!}} |0\rangle, \tag{5.3}$$

the expression in Eq. (1.2) becomes

$$|\alpha\rangle = D(\alpha)|0\rangle, \tag{5.4}$$

where

$$D(\alpha) = e^{-|\alpha|^2/2} e^{\alpha a^\dagger} e^{\alpha^* a}. \tag{5.5}$$

Also we can obtain the equivalent antinormal form of $D(\alpha)$, i.e.

$$D(\alpha) = e^{|\alpha|^2/2} e^{-\alpha^* a} e^{\alpha a^\dagger}, \tag{5.6}$$

by using the Baker-Haussdorff formula (Zassenhaus lemma)

$$e^{t(A+B)} = e^A e^B e^{-t^2[A,B]/2} e^{t^3(2[B,[A,B]]+[A,[A,B]])/6} \ldots \tag{5.7}$$

Note that $D(\alpha)$ is a unitary operator,

$$D^\dagger(\alpha) = D(-\alpha) = D^{-1}(\alpha) \tag{5.8}$$

and it acts as a displacement operator upon amplitudes a and $a^\dagger$,

$$D^{-1}(\alpha) a D(\alpha) = a + \alpha, \tag{5.9}$$

$$D^{-1}(\alpha) a^\dagger D(\alpha) = a^\dagger + \alpha^*. \tag{5.10}$$

Therefore coherent state is obtained by applying the displacement operator on the vacuum state, and hence it is the displaced form of the harmonic oscillator ground state. Each value of α in Eq. (5.2) corresponds to a different coherent state of light as shown in Fig. 5.1. The relation between α and the photon number n_c which the coherent state is centered at can be obtained as $\alpha \approx \sqrt{n_c}$ by differentiating Eq. (5.2) with respect to α.

On the other hand, by using the same concepts above, one can require that the

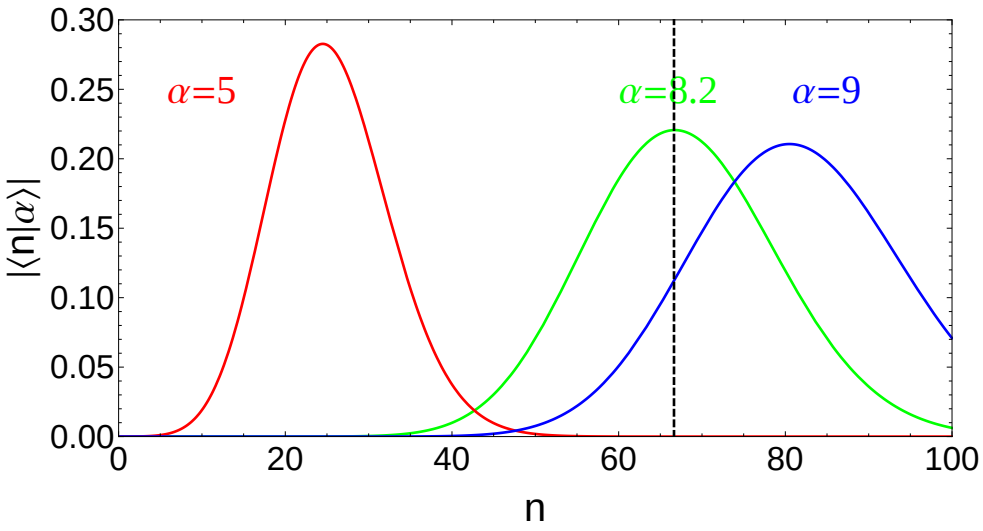

Figure 5.1: Coherent states of light with respect to photon number n are shown with different given values of $\alpha = 5.0(Red), 8.2(Green), 9.0(Blue)$ for a system of 100 photons, whereas superradiance region is represented by dashed lines.

coherent states $|\phi\rangle$ for spin $\boldsymbol{S}$ satisfy the relation,

$$\boldsymbol{S}_-|\phi\rangle = \phi|\phi\rangle. \tag{5.11}$$

Since the operator $\boldsymbol{S}_-$ acting on spin states $|\xi, m\rangle$ in S_z basis are given by

$$\boldsymbol{S}_-|m\rangle = \sqrt{(\xi+m)(\xi-m+1)}|m-1\rangle, \tag{5.12}$$

the expression for the spin coherent state can be obtained as

$$|\phi\rangle = C\sum_{m=-\xi}^{\xi}\sqrt{\frac{(2\xi)!}{(\xi+m)!(\xi-m)!}}\phi^{\xi+m}|m\rangle, \tag{5.13}$$

satisfying the property $\boldsymbol{S}_-|\phi\rangle = \phi|\phi\rangle$ given in Eq. (5.11). Orthonormality of the coherent state, i.e.

$$\begin{aligned}\langle\phi|\phi\rangle &= |C|^2\sum_{m,m'}\sqrt{\frac{(2\xi)!}{(\xi+m)!(\xi-m)!}}\sqrt{\frac{(2\xi)!}{(\xi+m')!(\xi-m')!}}\phi^{\xi+m}\phi^{*\xi+m'}\langle m'|m\rangle,\\ &= |C|^2\sum_{m=-\xi}^{\xi}\frac{(2\xi)!}{(\xi+m)!(\xi-m)!}|\phi|^{2(\xi+m)} = \mathbf{1},\end{aligned} \tag{5.14}$$

yields to the normalization constant

$$C = \frac{1}{(1+|\phi|^2)^{\xi}} \tag{5.15}$$

by binomial expansion. Therefore, the final form of the spin coherent state is obtained as

$$|\phi\rangle = \frac{1}{(1+|\phi|^2)^{\xi}} \sum_{m=-\xi}^{\xi} \sqrt{\frac{(2\xi)!}{(\xi+m)!(\xi-m)!}} \phi^{\xi+m} |m\rangle. \tag{5.16}$$

In the displacement operator form, it can also be written as

$$D(\phi) = (1+|\phi|^2)^{-\xi} e^{\phi S_+} e^{-\phi^* S_-}, \tag{5.17}$$

leading to another expression

$$|\phi\rangle = (1+|\phi|^2)^{-\xi} e^{\phi S_+} e^{-\phi^* S_-} |-\xi\rangle, \tag{5.18}$$

for the spin coherent state. Similar to the photon case, each value of ϕ yields to a different spin coherent state as shown in Fig. 5.2. The relation between ϕ and the spin number m_c which the coherent state centered at can be obtained as

$$\phi = \sqrt{\frac{\xi + m_c}{\xi - m_c}} \tag{5.19}$$

by differentiating Eq. (5.16) with respect to ϕ.

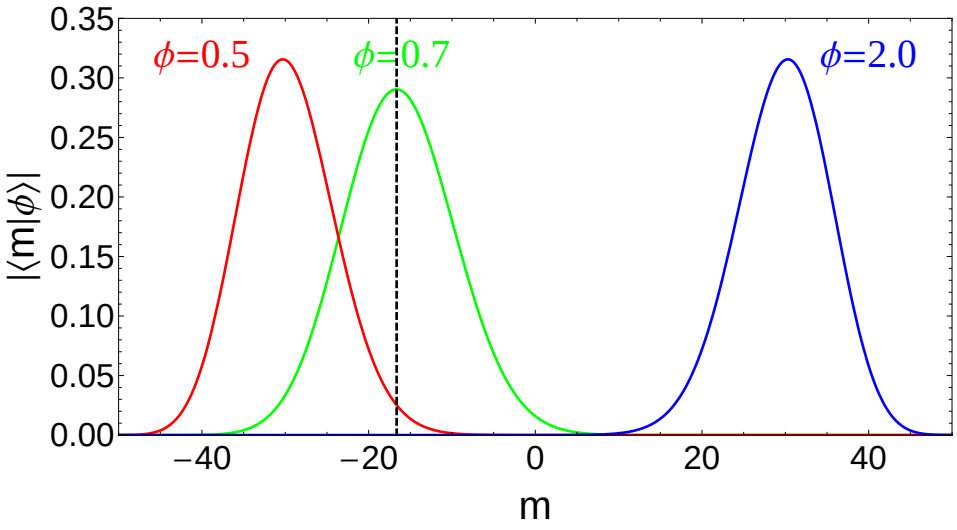

Figure 5.2: Coherent states of spin with respect to S_z eigenvalues m are shown with different given values of $\phi = 0.5(Red), 0.7(Green), 2.0(Blue)$ for a system of $S = 50$ ($\xi = 50$, corresponding to 100 spin one-halves), whereas superradiance region is represented by dashed lines.

5.2 Phase-locked Photon-Spin System

As a quick reminder, the Hamiltonian of the nanomagnet-cavity system is given by

$$\mathscr{H} = \hbar\omega_\gamma \left(a^\dagger a + \frac{1}{2}\right) + \frac{g\mu_B B_0}{\hbar} S_z - g\mu_B \Gamma_\gamma \left(aS_+ + a^\dagger S_-\right), \tag{5.20}$$

and the eigenfunctions of the system are formed of mixed entangled states of n and m, i.e.

$$|\Psi_j\rangle = \sum_{n=0}^{2\xi} \psi_j^n |n\rangle|\xi - n\rangle. \tag{5.21}$$

with energies (eigenvalues) E_j. The nanomagnet-cavity system can be initialized as the product state of the coherent state of light and spin, i.e. $|K(0)\rangle = |\alpha\rangle|\phi\rangle$,

$$\begin{aligned} |K(0)\rangle &= \frac{e^{-|\alpha|^2/2}}{(1+|\phi|^2)^\xi} e^{\alpha a^\dagger} e^{\alpha^* a} e^{\phi S_+} e^{-\phi^* S_-} |0\rangle_p|-\xi\rangle_s, & (5.22)\\ &= \frac{e^{-|\alpha|^2/2}}{(1+|\phi|^2)^\xi} \sum_{n=0}^{2\xi} \sum_{-\xi}^{\xi} \frac{\alpha^n}{\sqrt{n!}} \phi^{\xi+m} \sqrt{\frac{(2\xi)!}{(\xi+m)!(\xi-m)!}} |n\rangle|m\rangle, & (5.23) \end{aligned}$$

where the spins of the nanomagnet and the photons of the cavity are initially independent of each other and intrinsically coherent. However, over time, they get coupled with each other through the interaction part of the Hamiltonian given in Eq. (5.20).

Time evolution of the initial state $|K(0)\rangle$ can be expanded over the eigenfunctions of the cavity-nanomagnet system since they span a complete orthogonal Hilbert space,

$$\begin{aligned} |K(t)\rangle &= e^{-i\mathscr{H}t/\hbar}|K(0)\rangle \\ &= \sum_j |\Psi_j\rangle\langle\Psi_j|e^{-itH/\hbar}|K(0)\rangle \\ &= \sum_j e^{-itE_j/\hbar}|\Psi_j\rangle\langle\Psi_j|K(0)\rangle. \end{aligned} \tag{5.24}$$

Using the Eq. (5.21) and Eq. (5.23) for the constants $\langle\Psi_j|K(0)\rangle$ leads to

$$\begin{aligned} \langle\Psi_j|K(0)\rangle &= \sum_{n,p=0}^{2\xi} \sum_{m=-\xi}^{\xi} \psi_j^{n*} \langle n, \xi-n|p,m\rangle \frac{e^{-|\alpha|^2/2}}{(1+|\phi|^2)^\xi} \sqrt{\frac{(2\xi)!}{(\xi+m)!(\xi-m)!}} \frac{\alpha^p}{\sqrt{p!}} \phi^{\xi+m} \\ &= \sum_{n,p=0}^{2\xi} \sum_{m=-\xi}^{\xi} \psi_j^{n*} \delta_{p,n}\delta_{m,\xi-n} \frac{e^{-|\alpha|^2/2}}{(1+|\phi|^2)^\xi} \sqrt{\frac{(2\xi)!}{(\xi+m)!(\xi-m)!}} \frac{\alpha^p}{\sqrt{p!}} \phi^{\xi+m} \\ &= \sum_{n=0}^{2\xi} \psi_j^{n*} \frac{e^{-|\alpha|^2/2}}{(1+|\phi|^2)^\xi} \sqrt{\frac{(2\xi)!}{(2\xi-n)!}} \frac{\alpha^n}{n!} \phi^{2\xi-n} \end{aligned} \tag{5.25}$$

$$= \sum_{n=0}^{2\xi} C_j^n = C_j. \tag{5.26}$$

Therefore, the time dependent product of photon and spin coherent states is obtained as

$$|K(t)\rangle = \sum_j \sum_{n'=0}^{2\xi} C_j e^{-itE_j/\hbar} \psi_j^{n'} |n'\rangle, \tag{5.27}$$

in terms of the wavefunctions of the cavity-nanomagnet system.

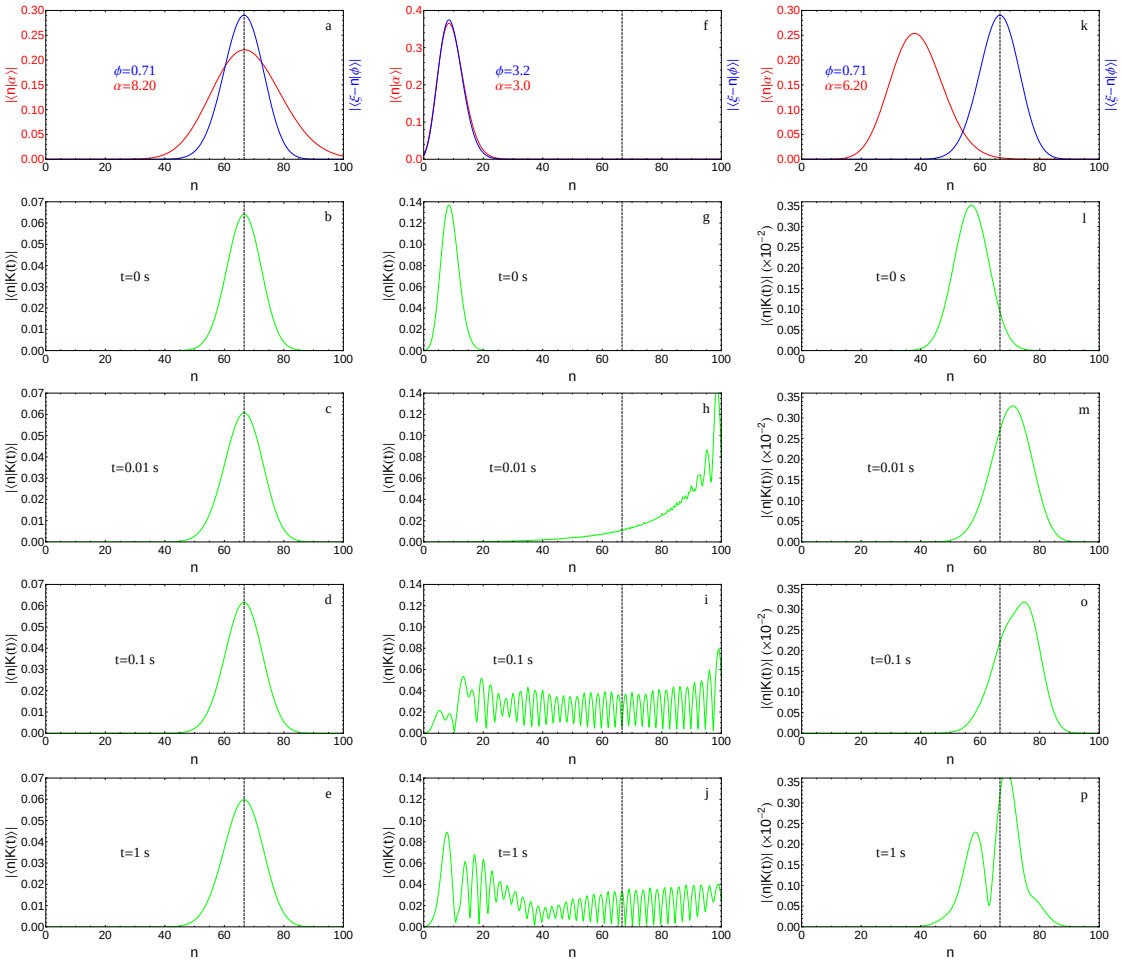

Figure 5.3: For $N = 100$ spins and photons, the initial independent photon (*Red*) and spin (*Blue*) coherent states before the interaction is turned on are shown for different values of α and ϕ (a)-(f)-(k), whereas superradiance regime is represented by a *Dashed* line. For each initial configuration (columns), products of these photon and spin coherent states (*Green*) under the influence of coupling are plotted for times $t = 0$, 0.01, 0.1, and 1 seconds with respect to photon number n.

The initial configuration of photon and spin coherent states given in Eq. (5.2) and Eq. (5.16) are determined by the parameters α and ϕ as shown in Fig. 5.3(a)-(f)-(k) for $N = 100$ spins and photons ($\xi = 50$). For different values of α and ϕ, these coherent states are initially localized around different photon and spin numbers. As shown in the first column of Fig. 5.3, if both of these coherent states are initially localized around the superradiance regime before the interaction is turned on, they can be efficiently phase-locked together into a coherent state of the system due to the strong nanomagnet-cavity coupling between them. On the other hand, if they are both localized at different photon/spin number rather than where the superradiance regime lies (see second column of Fig. 5.3), product state will decohere very fast and phase-locking will not be achieved. However, if only one of these initial coherent states is centered around the superradiance regime (see third column of Fig. 5.3) and there is an overlap between the coherent states, there will still be a short-lived phase-locking. Therefore, the efficient and stable phase-locking via nanomagnet-cavity coupling is only feasible if both of these unentangled coherent states of spin and photon are initially localized at the superradiance regime.

CHAPTER 6
CONCLUSION

In conclusion, we have examined the strong-field interactions between a nanomagnet of radius roughly 100 nm consisting of 10^9 spins and a spherical microcavity roughly 1 mm^3 in volume in the presence of a static magnetic field of 7 T in magnitude. Our results demonstrate that the interaction Hamiltonian contains magnet-microwave mode coupling terms that can exceed several THz, indicating that strong-field coupling between magnets and light is possible, and should substantially exceed the coupling observed in solids between orbital transitions and light. These strong-field effects should be observable in the nanomagnet-cavity dynamics. Furthermore, the coherent states of our spin-photon coupling around the superradiance regime are characterized by large oscillations in photon number n of the cavity (or equivalently the collective spin number m_s of the nanomagnet) with exceptionally long dephasing times of few seconds. The effects of magnons have been also considered and shown to not substantially modify these results upto room temperature. Moreover, the coherent dynamics of a coupled photonic cavity and a nanomagnet is explored as a function of nanomagnet size. For sufficiently strong coupling, eigenstates involving highly entangled photon and spin states are found, which can be combined to create coherent states. As the size of the nanomagnet increases its coupling to the photonic mode also monotonically increases, as well as the number of photon and spin states involved in the systems eigenstates. For small nanomagnets the crystalline magnetic anisotropy of the magnet strongly localized the eigenstates in photon and spin number, quenching the potential for coherent states. For a sufficiently large nanomagnet the macrospin approximation breaks down and different domains of the nanomagnet may couple separately to the photonic mode. Thus the optimal nanomagnet size is predicted to be just below the threshold for failure of the macrospin approximation. Therefore, the coherent dynamics is expected to be observable for realistic nanomagnets with radii of

10 - 50 nm. Moreover, it is shown that initially unentangled coherent states of light (cavity field) and spin (nanomagnet spin orientation) can be phase-locked together to evolve into a coherent entangled states of the system under the influence of strong coupling.

The realization and development of quantum information technology and understanding of quantum coherence using this concept of strong coupling between light and spins may greatly advance the field. For instance, entangled states of light and very large ensembles of spins with long coherence times and their utilization to achieve efficient retrieval of the stored quantum state and direct manipulation capability to read and write the states easily can be harnassed to achieve quantum memory and quantum repeaters. Moreover, due to coupling strengths reaching THz frequencies around the spin superradiance region with high power emission and phase-locking capabilities, there lies the possibility to develop the next generation spin torque nano oscillators and spin masers by using our strong coupling scheme.

APPENDIX A
BASIS FUNCTIONS FOR TE AND TM MODES

The basis functions used to quantize the cavity field for each mode are

$$\mathbf{u}_{lm} = \left\{ \begin{array}{l} f_l(kr) \\ g_l(kr) \end{array} \right\} \mathbf{Y}_{l,l,m} \qquad \begin{array}{l} TM, \\ TE. \end{array} \tag{A.1}$$

If one write the coordinate unit vectors $\hat{\mathbf{x}}$, $\hat{\mathbf{y}}$, $\hat{\mathbf{z}}$ in spherical notation

$$\hat{\mathbf{e}}_+ = -\tfrac{\hat{\mathbf{x}}+i\hat{\mathbf{y}}}{\sqrt{2}} \quad , \hat{\mathbf{e}}_- = \tfrac{\hat{\mathbf{x}}-i\hat{\mathbf{y}}}{\sqrt{2}} \quad , \hat{\mathbf{e}}_0 = \hat{\mathbf{z}}, \tag{A.2}$$

so that $\hat{\mathbf{e}}_m$ form a spherical tensor of rank 1, the spherical harmonics coupled with the $\hat{\mathbf{e}}_m$ to total angular momentum $\boldsymbol{J}$ using the Clebsch-Gordon coefficients leads to the following definition of vector spherical harmonics

$$\boldsymbol{Y}_{j,l,m_j}(\theta,\phi) = \sum_{m_l,m} CG\langle l,1,j|m_l,m,m_j\rangle Y_l^{m_l}(\theta,\phi)\hat{\mathbf{e}}_m. \tag{A.3}$$

They obey the orthogonality relations

$$\int \boldsymbol{Y}^*_{j,l,m_j}(\theta,\phi)\cdot\boldsymbol{Y}_{j',l',m'_j}(\theta,\phi)d\Omega = \delta_{jj'}\delta_{ll'}\delta_{m_j m'_j}. \tag{A.4}$$

The inversion of Eq. (A.3) by using the selection rules of angular momentum and substituting their corresponding Clebsch-Gordon coefficients yields to

$$\hat{\mathbf{r}}Y_l^m(\theta,\phi) = -\sqrt{\frac{l+1}{2l+1}}\boldsymbol{Y}_{l,l+1,m} + \sqrt{\frac{l}{2l+1}}\boldsymbol{Y}_{l,l-1,m}, \tag{A.5}$$

showing the vector character of $\boldsymbol{Y}$'s and the orbital angular momentum relations, $l+1$ and $l-1$. If $j=l$, as in the case of the basis functions of Eq. (A.1), the vector spherical harmonics can also be expressed in a simplified way

$$\boldsymbol{Y}_{l,l,m}(\theta,\phi) = \frac{\boldsymbol{L}Y_l^m(\theta,\phi)}{\sqrt{l(l+1)}} = \boldsymbol{X}_{l,m}(\theta,\phi), \tag{A.6}$$

by using the orbital angular momentum operator $\boldsymbol{L}$. Curl of the basis functions satisfy

$$\begin{aligned} \nabla\times[f_l(kr)\boldsymbol{Y}_{l,l,m}] &= i\sqrt{\frac{l}{2l+1}}\left[\frac{df_l(kr)}{dr} - \frac{l}{r}f_l(kr)\right]\boldsymbol{Y}_{l,l+1,m} \\ &\quad + i\sqrt{\frac{l+1}{2l+1}}\left[\frac{df_l(kr)}{dr} + \frac{l+1}{r}f_l(kr)\right]\boldsymbol{Y}_{l,l-1,m}. \end{aligned} \tag{A.7}$$

where $f_l(kr)$ (or $g_l(kr)$, depending on the mode) is the appropriate Green function solution

$$g_l(kr) = A_l^{(1)} h_l^{(1)}(kr) + A_l^{(2)} h_l^{(2)}(kr), \tag{A.8}$$

in terms of spherical Hankel functions $h_l^{(1,2)}(kr)$. The differential recursion relations of $f_l(x)$ can be obtained as

$$\frac{d}{dx}\left[x^{l+1} f_l(x)\right] = (l+1)x^l f_l(x) + x^{l+1}\frac{df_l(x)}{dx} = x^{l+1} f_{l-1}(x), \tag{A.9}$$

$$\frac{d}{dx}\left[x^{-l} f_l(x)\right] = -l x^{-l-1} f_l(x) + x^{-l}\frac{df_l(x)}{dx} = -x^{-l} f_{l+1}(x). \tag{A.10}$$

Dividing Eq. (A.9) and Eq. (A.10) by x^{l+1} and x^{-l}, respectively, results with

$$\frac{df_l(x)}{dx} + \frac{l+1}{x} f_l(x) = f_{l-1}(x), \tag{A.11}$$

$$\frac{df_l(x)}{dx} - \frac{l}{x} f_l(x) = -f_{l+1}(x). \tag{A.12}$$

Therefore, substitution of Eq. (A.11) and Eq. (A.12) into Eq. (A.7) yields to the curl of the basis functions,

$$\begin{aligned} \nabla \times [f_l(kr)\boldsymbol{X}_{lm}(\theta,\phi)] &\equiv \nabla \times [f_l(kr)\boldsymbol{Y}_{l,l,m}(\theta,\phi)] \\ &= -ik\sqrt{\frac{l}{2l+1}} f_{l+1}(kr)\boldsymbol{Y}_{l,l+1,m}(\theta,\phi) \\ &\quad +ik\sqrt{\frac{l+1}{2l+1}} f_{l-1}(kr)\boldsymbol{Y}_{l,l-1,m}(\theta,\phi) \end{aligned} \tag{A.13}$$

BIBLIOGRAPHY

[1] R. H. Dicke. Coherence in spontaneous radiation processes. *Phys. Rev.*, 93:99, 1954.

[2] M. Tavis and F. W. Cummings. Exact solution for an n-molecule-radiation-field hamiltonian. *Phys. Rev.*, 170:379, 1968.

[3] H. J. Kimble. Strong interactions of single atoms and photons in cavity QED. *Phys. Scr.*, T76:127, 1998.

[4] J. M. Raimond, M. Brune, and S. Haroche. Manipulating quantum entanglement with atoms and photons in a cavity. *Rev. Mod. Phys.*, 73:565, 2001.

[5] H. Walther. Quantum phenomena of single atoms. *Adv. Chem. Phys.*, 122:167, 2002.

[6] G. Nogues, A. Rauschenbeutel, S. Osnaghi, M. Brune, J. M. Raimond, and S. Haroche. Seeing a single photon without destroying it. *Nature*, 400:239, 1999.

[7] A. Rauschenbeutel, G. Nogues, S. Osnaghi, P. Bertet, M. Brune, J. M. Raimond, and S. Haroche. Coherent operation of a tunable quantum phase gate in cavity QED. *Phys. Rev. Lett.*, 83:5166, 1999.

[8] Q. A. Turchette, C. J. Hood, W. Lange, H. Mabuchi, and H. J. Kimble. Measurement of conditional phase shifts for quantum logic. *Phys. Rev. Lett.*, 75: 4710, 1995.

[9] G. Rempe. One atom in an optical cavity: Spatial resolution beyond the standard diffraction limit. *Appl. Phys. B*, 60:233, 1995.

[10] P. W. H. Pinkse, T. Fischer, P. Maunz, and G. Rempe. Trapping an atom with single photons. *Nature*, 404:365, 2000.

[11] M. Weidinger, B. T. H. Varcoe, R. Heerlein, and H. Walther. Trapping states in the micromaser. *Phys. Rev. Lett.*, 82:3795, 1999.

[12] Simon Brattke, Benjamin T. H. Varcoe, and Herbert Walther. Generation of photon number states on demand via cavity quantum electrodynamics. *Phys. Rev. Lett.*, 86:3534, 2001.

[13] G. T. Foster, L. A. Orozco1, H. M. Castro-Beltran, and H. J. Carmichae. Quantum state reduction and conditional time evolution of wave-particle correlations in cavity QED. *Phys. Rev. Lett.*, 85:3149, 2000.

[14] W. P. Smith, J. E. Reiner, L. A. Orozco, S. Kuhr, and H. M. Wiseman. Capture and release of a conditional state of a cavity QED system by quantum feedback. *Phys. Rev. Lett.*, 89:133601, 2002.

[15] A. Kiraz, P. Michler, C. Becher, B. Gayral, A. Imamoglu, Lidong Zhang, E. Hu, W. V. Schoenfeld, and P. M. Petroff. Cavity-quantum electrodynamics using a single inas quantum dot in a microdisk structure. *Appl. Phys. Lett.*, 78:3932, 2001.

[16] P. F. Herskind, A. Dantan, J. P. Marler, M. Albert, and M. Drewsen. Realization of collective strong coupling with ion coulomb crystals in an optical cavity. *Nature Physics*, 5:494, 2009.

[17] K. J. Boller, A. Imamoglu, and S. E. Harris. Observation of electromagnetically induced transparency. *Phys. Rev. Lett.*, 66:2593, 1991.

[18] L.V. Hau, S. E. Harris, Z. Dutton, and C. H. Behroozi. Light speed reduction to 17 metres per second in an ultracold atomicgas observation of electromagnetically induced transparency. *Nature*, 397:594, 1999.

[19] M. O. Scully and M. Fleischhauer. Lasers without inversion. *Science*, 263:337, 1994.

[20] G. G. Padmabandu et al. Laser oscillation without population inversion in a sodium atomic beam. *Phys. Rev. Lett.*, 76:2053, 1996.

[21] O. Kocharovskaya, P. Mandel, and M. O. Scully. Atomic coherence via modified spontaneous relaxation of driven three-level atoms. *Phys. Rev. Lett.*, 74:2451, 1995.

[22] S. Sultana and M.S. Zubairy. Effect of finite bandwidth on refractive-index enhancement and lasing without inversion. *Phys. Rev. A*, 49:438, 1994.

[23] C. H. Bennett, G. Brassard, R. Jozsa C. Crpeau, A. Peres, and W. K. Wootters. Teleporting an unknown quantum state via dual classical and Einstein-Podolsky-Rosen channels. *Phys. Rev. Lett.*, 70:1895, 1993.

[24] D. Bouwmeester, J.-W. Pan, K. Mattle, M. Eibl, H. Weinfurter, and A. Zeilinger. Experimental quantum teleportation. *Nature*, 390:575, 1997.

[25] D. Boschi, S. Branca, F. De Martini, L. Hardy, and S. Popescu. Experimental realization of teleporting an unknown pure quantum state via dual classical and Einstein-Podolsky-Rosen channels. *Phys. Rev. Lett*, 80:1121, 1998.

[26] M. A. Nielsen, E. Knill, and R. Laflamme. Complete quantum teleportation using nuclear magnetic resonance. *Nature*, 396:52, 1998.

[27] Q. Zhang, A. Goebel, C. Wagenknecht, Y.-A. Chen, B. Zhao, T. Yang T, A. Mair, and J. Schmiedmayer. Experimental quantum teleportation of a two-qubit composite system. *Nat. Phys.*, 2:678, 2006.

[28] J. F. Sherson, H. Krauter, R. K. Olsson, B. Julsgaard, K. Hammerer, I. Cirac, and E. S. Polzik. Quantum teleportation between light and matter. *Nature*, 443: 557, 2006.

[29] L. Davidovich, N. Zagury, M. Brune, J. M. Raimond, and S. Haroche. Teleportation of an atomic state between two cavities using nonlocal microwave fields. *Phys. Rev. A*, 50:R895, 1994.

[30] J. I. Cirac and A. S. Parkins. Schemes for atomic-state teleportation. *Phys. Rev. A*, 50:R4441, 1994.

[31] S. B. Zheng and G. C. Guo. Teleportation of an unknown atomic state through the Raman atom-cavity-field interaction. *Phys. Lett. A*, 232:171, 1997.

[32] S. Bose, P. L. Knight, M. B. Plenio, and V. Vedral. Proposal for teleportation of an atomic state via cavity decay. *Phys. Rev. Lett.*, 83:5158, 1999.

[33] S. Bandyopadhyay. Teleportation and secret sharing with pure entangled states. *Phys. Rev. A*, 62:012308, 2000.

[34] A. Forchel et al. Strong coupling in a single quantum dotsemiconductor microcavity system. *Nature*, 432:197, 2004.

[35] J. D. Jackson. *Classical Electrodynamics*. Wiley, New York, 3 edition, 1998. p. 259.

[36] D. D. Awschalom, N. Samarth, and D. Loss. *Semiconductor Spintronics and Quantum Computation*. Springer Verlag, Heidelberg, 2002.

[37] D. D. Awschalom and M. E. Flatté. Challenges for semiconductor spintronics. *Nature Physics*, 3:153–159, 2007.

[38] G. Feher, J. P. Gordon, E. Buehler, E. A. Gere, and C. D. Thurmond. Spontaneous emission of radiation from an electron spin system. *Phys. Rev.*, 109: 221–222, 1958.

[39] M. G. Benedict. *Super-radiance: Multiatomic Coherent Radiation*. CRC Press, new york, 1996.

[40] A. V. Andreev, V. J. Emelyanov, and Yu. A. Ilinskii. *Cooperative Effects in Optics*. IOP Publishing, Bristol, 1993.

[41] E. M. Chudnovsky and D. A. Garanin. Superradiance from crystals of molecular nanomagnets. *Phys. Rev. Lett.*, 89(15):157201, Sep 2002.

[42] W. H. Rippard et al. Direct-current induced dynamics in co90fe10/ni80fe20 point contacts. *Phys. Rev. Lett.*, 92:027201, 2004.

[43] J. C. Sankey et al. Spin-transfer-driven ferromagnetic resonance of individual nanomagnets. *Phys. Rev. Lett.*, 96:227601, 2006.

[44] L. Berger. Emission of spin waves by a magnetic multilayer traversed by a current. *Phys. Rev. B*, 54:9353–9358, 1996.

[45] J. C. Slonczewski. Current-driven excitation of magnetic multilayers. *J. Magn. Magn. Mat.*, 159:L1–L7, 1996.

[46] E. B. Myers, D. C. Ralph, J. A. Katine, R. N. Louie, and R. A. Buhrman. Current-induced switching of domains in magnetic multilayer devices. *Science*, 285:867–870, 1999.

[47] S. I. Kiselev. Microwave oscillations of a nanomagnet driven by a spin-polarized current. *Nature*, 425:380–383, 2003.

[48] S. Urazhdin et al. Manipulating current-induced magnetization switching. *J. Appl. Phys.*, 97:10C701, 2005.

[49] E. T. Jaynes and F. W. Cummings. Comparison of quantum and semiclassical radiation theories with application to the beam maser. *Proc. IEEE*, 51:89, 1963.

[50] M. Tavis and F. W. Cummings. Approximate solution for an n-molecule-radiation-field hamiltonian. *Phys. Rev.*, 188:692, 1969.

[51] B. W. Shore and P. L. Knight. The Jaynes-Cummings model. *J. Mod. Opt.*, 40: 1195, 1993.

[52] D. Ellinas and I Smyrnakis. Asymptotics of a quantum random walk driven by an optical cavity. *J. Opt. B*, 7:S152, 2005.

[53] F. W. Cummings. Stimulated emission of radiation in a single mode. *Phys. Rev.*, 140:A1051, 1965.

[54] J.H. Eberly, N.B. Narozhny, and J.J. Sanchez-Mondragon. Periodic spontaneous collapse and revival in a simple quantum model. *Phys. Rev. Lett.*, 44:1323, 1980.

[55] G. Rempe, H. Walther, and N. Klein. Observation of quantum collapse and revival in a one-atom maser. *Phys. Rev. Lett.*, 58:353, 1987.

[56] S. Haroche and J.M. Raimond. *Advances in Atomic and Molecular Physics*. Academic Press, New York, 1985. p. 350.

[57] J.A.C. Gallas, G. Leuchs, H. Walther, and H. Figger. *Advances in Atomic and Molecular Physics*. Academic Press, New York, 1985. p. 414.

[58] A. Kundu. Quantum integrable multiatom matter-radiation models with and without the rotating-wave approximation. *Theor. Math. Phys.*, 144:975, 2005.

[59] I.I. Rabi, J.R. Zacharias, S. Millman, and P. Kusch. A new method of measuring nuclear magnetic moment. *Phys. Rev.*, 53:318, 1938.

[60] N. Bloembergen, E. M. Purcell, and R. V. Pound. Relaxation effects in nuclear magnetic resonance absorption. *Phys. Rev.*, 73:679, 1948.

[61] W. Gordy. Microwave spectroscopy. *Rev. Mod. Phys.*, 20:668, 1948.

[62] R. H. Romer and R. H. Dicke. New technique for high-resolution microwave spectroscopy. *Phys. Rev.*, 99:532, 1955.

[63] G. Grynberg, B. Lounis, P. Verkerk, J. Y. Courtois, and C. Salomon. Quantized motion of cold cesium atoms in two- and three-dimensional optical potentials. *Phys. Rev. Lett.*, 70:2249, 1993.

[64] F. Dimer, B. Estienne, A. S. Parkins, and H. J. Carmichael. Proposed realization of the Dicke-model quantum phase transition in an optical cavity qed system. *Phys. Rev. A*, 75:013804, 2007.

[65] M. G. Raymer and J. Mostowski. Stimulated raman scattering: Unified treatment of spontaneous initiation and spatial propagation. *Phys. Rev. A*, 24:1980, 1981.

[66] K. Drühl, R. G. Wenzel, , and J. L. Carlsten. Observation of solitons in stimulated raman scattering. *Phys. Rev. Lett.*, 51:1171, 1983.

[67] J. Mostowski and B. Sobolewska. Transverse effects in stimulated raman scattering. *Phys. Rev. A*, 30:610, 1984.

[68] J. Mostowski and B. Sobolewska. Waveguide effects in superfluorescence and stimulated raman scattering. *Phys. Rev. A*, 34:3109, 1986.

[69] A. A. Zabolotskiĭ, S. G. Rautian, A. P. Satanov, and B. M. N. Chernabrod. Investigation of effects of energy-level degeneracy in cooperative raman scattering of light. *Sov. Phys. JETP*, 59:696, 1984.

[70] M. G. Raymer, I. A. Walmsley, J. Mostowski, and B. Sobolewska. Quantum theory of spatial and temporal coherence properties of stimulated raman scattering. *Phys. Rev. A*, 32:332, 1985.

[71] A. A. Zabolotskiĭ, S. G. Rautian, A. P. Satanov, and B. M. N. Chernabrod. Coherent raman light conversion in a two-level medium. *Sov. Phys. JETP*, 66: 47, 1987.

[72] Y. K. Wang and F. T. Hioe. Phase transition in the Dicke model of superradiance. *Phys. Rev. A*, 7:831, 1973.

[73] H. J. Carmichael, C. W. Gardiner, and D. F. Walls. Phase transition in the Dicke model of superradiance. *Phys. Lett.*, 46A:47, 1973.

[74] C. Emary and T. Brandes. Phase transition in the Dicke model of superradiance. *Phys. Rev. Lett.*, 90:044101, 2003.

[75] J. P. Gordon, L. R. Walker, and W. H. Louiselle. Quantum statistics of masers and attenuators. *Phys. Rev.*, 130:806, 1963.

[76] A. E. Glassgold and D. Holliday. Quantum statistical dynamics of laser amplifiers. *Phys. Rev.*, 139:A1717, 1965.

[77] J. A. Fleck. Quantum theory of laser radiation. i. many-atom effects. *Phys. Rev.*, 149:309, 1966.

[78] M. O. Scully and W. E. Lamb. Quantum theory of an optical maser. i. general theory. *Phys. Rev.*, 159:A208, 1967.

[79] T. Yu and J. H. Eberly. Finite-time disentanglement via spontaneous emission. *Phys. Rev. Lett.*, 93:140404, 2004.

[80] K. Roszak and P. Machnikowski. Complete disentanglement by partial pure dephasing. *Phys. Rev. A*, 73:022313, 2006.

[81] Z. Ficek and R. Tanas. Dark periods and revivals of entanglement in a two-qubit system. *Phys. Rev. A*, 74:024304, 2006.

[82] R. F. Liu and C. C. Chen. Role of the bell singlet state in the suppression of disentanglement. *Phys. Rev. A*, 74:024102, 2006.

[83] M. Yönac, T. Yu, and J. H. Eberly. Sudden death of entanglement of two Jaynes-Cummings atoms. *J. Phys. B: At. Mol. Opt. Phys.*, 39:S621, 2006.

[84] J. H. Eberly T. Yu. Qubit disentanglement and decoherence via dephasing. *Phys. Rev. B*, 68:165322, 2003.

[85] M. Sparks. *Ferromagnetic Relaxation Theory.* McGraw-Hill, New York, 1964.

[86] C. Kittel. *Quantum Theory of Solids.* John Wiley & Sons, New York, 1963.

[87] W. Heitler and F. London. Reciprocal action of neutral atoms and homopolar combination according to quantum mechanics. *Z. Physik*, 44:455, 1927.

[88] T. Oguchi. Theory of spin wave interactions in ferro- and antiferromagnetism. *Phys. Rev.*, 117:117, 1960.

[89] T. Holstein and H. Primakoff. Field dependence of the intrinsic domain magnetization of a ferromagnet. *Phys. Rev.*, 58:1098, 1940.

[90] F. J. Dyson. General theory of spin-wave interactions. *Phys. Rev.*, 102:1217, 1956.

[91] F. J. Dyson. Thermodynamic behavior of an ideal ferro-magnet. *Phys. Rev.*, 102:1230, 1956.

[92] J. H. E. Griffith. Anomalous high-frequency resistance of ferromagnetic metals. *Nature*, 158:670, 1946.

[93] C. Kittel. Interpretation of anomalous larmor frequencies in ferromagnetic resonance experiment. *Phys. Rev.*, 71:270, 1947.

[94] C. Kittel. On the theory of ferromagnetic resonance absorption. *Phys. Rev.*, 73: 155, 1948.

[95] C. Kittel. Developments in nano-oscillators based upon spin-transfer point-contact devices. *J. Magn. Magn. Mater.*, 320:1260, 2008.

[96] M. Tsoi, A. G. M. Jansen, J. Bass, W. C. Chiang, M. Seck, V. Tsoi, and P. Wyder. Excitation of a magnetic multilayer by an electric current. *Phys. Rev. Lett.*, 80:4281, 1998.

[97] J. Z. Sun. Current-driven magnetic switching in manganite trilayer junctions. *J. Magn. Magn. Mater.*, 202:157, 1999.

[98] M. Tsoi, A. G. M. Jansen, J.Bass, W. C. Chiang, V. Tsoi, and P. Wyder. Generation and detection of phase-coherent current-driven magnons inmagnetic multilayers. *Nature*, 406:46, 2000.

[99] J. A. Katine, F. J. Albert, R. A. Buhrman, E. B. Myers, and D. C. Ralph. Current-driven magnetization reversal and spin-wave excitations in co/cu/co pillars. *Phys. Rev. Lett.*, 84:3149, 2000.

[100] J. Grollier, V. Cros, A. Hamzic, J. M. George, H. Jaffres, A. Fert, G. Faini, J. B. Youssef, and H. Legall. Spin-polarized current induced switching in co/cu/co pillars. *Appl. Phys. Lett.*, 78:3663, 2001.

[101] R. Urban, G. Woltersdorf, and B. Heinrich. Gilbert damping in single and multilayer ultrathin films: Role of interfaces in nonlocal spin dynamics. *Phys. Rev. Lett.*, 87:217204, 2001.

[102] J. Z. Sun, D. J. Monsma, M. J. Rooks, and R. H. Koch. Batch-fabricated spin-injection magnetic switches. *Appl. Phys. Lett.*, 81:2202, 2002.

[103] J. E. Wegrowe, X. Hoffer, Ph. Guittienne, A. Fabian, L. Gravier, T. Wade, and J. Ph. Ansermet. Spin-polarized current induced magnetization switch: Is the modulus of the magnetic layer conserved? *J. Appl. Phys.*, 91:6806, 2002.

[104] D. V. Berkov and J. Miltat. Spin-torque driven magnetization dynamics: Micromagnetic modeling. *J. Magn. Magn. Mater.*, 320:1238, 2008.

[105] M. D. Stiles, J. Xiao, and A. Zangwill. Phenomenological theory of current-induced magnetization precession. *Phys. Rev. B*, 69:054408, 2004.

[106] D. Houssameddine et al. Spin-torque oscillator using a perpendicular polarizer and a planar free layer. *Nature. Mater.*, 6:447, 2007.

[107] I. N. Kirovotorov, D. V. Berkov, N. L. Gorn, N. C. Emley, J. C. Sankey, D. C. Ralph, and R. A. Buhrman. Large-amplitude coherent spin waves excited by spin-polarized current in nanoscale spin valves. *Phys. Rev. B*, 76:024418, 2007.

[108] S. A. Wolf, D. D. Awschalom, R. A. Buhrman, J. M. Daughton, S. von Molnar, M. L. Roukes, A. Y. Chtchelkanova, and D. M. Treger. Spintronics: A spin-based electronics vision for the future. *Science*, 294:1488, 2001.

[109] V. S. Pribiag. Magnetic vortex oscillator driven by d.c. spin-polarized current. *Nature Phys.*, 3:498–503, 2007.

[110] O. Boulle. Shaped angular dependence of the spin-transfer torque and microwave generation without magnetic field. *Nature Phys.*, 3:492–497, 2007.

[111] M. R. Pufall, W. H. Rippard, M. L. Schneider, and S. E. Russek. Low-field current-hysteretic oscillations in spin-transfer nanocontacts. *Phys. Rev. B*, 75: 140404, 2007.

[112] J. N. Kupferschmidt, S. Adam, and P. W. Brouwer. Theory of the spin-torque-driven ferromagnetic resonance in a ferromagnet/normal-metal/ferromagnet structure. *Phys. Rev. B*, 74:134416, 2006.

[113] Shehzaad Kaka, Matthew R. Pufall, William H. Rippard, Thomas J. Silva, Stephen E. Russek, and Jordan A. Katine. Mutual phase-locking of microwave spin torque nano-oscillators. *Nature*, 437:389, 2005.

[114] W. H. Rippard, M. R. Pufall, S. Kaka, T. J. Silva, and S. E. Russek. Injection locking and phase control of spin transfer oscillators. *Phys. Rev. Lett.*, 95:067203, 2005.

[115] W. A. Harrison and S. Ciraci. Bond-orbital model. ii. *Phys. Rev. B*, 10:1516, 1974.

[116] R.J. Glauber. Coherent and incoherent states of the radiation field. *Phys. Rev.*, 131:2766, 1963.

[117] T. L. Gilbert. A phenomenological theory of damping in ferromagnetic materials. *IEEE. Trans. Magn.*, 40:3443, 2004.

[118] S. P. Bayrakci, T. Keller, K. Habicht, and B. Keimer. Spin-wave lifetimes throughout the brillouin zone. *Science*, 312:1926, 2006.

[119] R. C. Fletcher, R. C. LeCraw, and E. G. Spencer. Electron spin relaxation in ferromagnetic insulators. *Phys. Rev.*, 117:955, 1960.

[120] L. H. Bennett and E. D. Torre. The chemical potential of magnons in quasi-equilibrium. *Physica B*, 403:324, 2008.

[121] K. P. Sinha and U. N. Upadhyaya. Phonon-magnon interaction in magnetic crystals. *Phys. Rev.*, 127:432, 1962.

[122] R. C. LeCraw and E. G. Spencer. Intrinsic relaxation of the uniform precession in ferromagnetic resonance of yttrium iron garnet. *J. Phys. Soc. Jpn.*, 17:401, 1962. Supp. B1.

[123] M. Sparks and C. Kittel. Ferromagnetic relaxation mechanism for mz in yttrium iron garnet. *Phys. Rev. Lett.*, 4:232, 1960.

[124] Z. Frait and D. Fraitova. Ferromagnetic resonance and surface anisotropy in iron single crystals. *J. Magn. Magn. Mater.*, 15-18:1081, 1980.

[125] G. F. Dionne and G. L. Fitch. Temperature dependence of spin-lattice relaxation in rare-earth iron garnets. *J. Appl. Phys.*, 87:4963, 2000.

[126] M. Rajendran, S. Deka, P. A. Joy, and A. K. Bhattacharya. Size-dependent magnetic properties of nanocrystalline yttrium iron garnet powders. *J. Magn. Magn. Mater.*, 301:212, 2006.

[127] B. Hillebrands and A. Thiaville. *Spin Dynamics in Confined Magnetic Structures III*. Springer-Verlag, Berlin, 2006.

[128] M. Moskovits. Surface-enhanced spectroscopy. *Rev. Mod. Phys.*, 57:783, 1985.

[129] L. Bogani and W. Wernsdorfer. Molecular spintronics using single-molecule magnets. *Nature Materials*, 7:179, 2008.

[130] A. Pikovsky, M. Rosenblum, and J. Kurths. *Synchronization*. Cambridge University Press, Cambridge, 2001.

[131] A. K. Jain, K. K. Likharev, J. E. Lukens, and J. E. Sauvageau. Mutual phase-locking in josephson junction arrays. *Phys. Rep.*, 109:309, 1984.

[132] C. Weisbuch, M. Nishioka, A.Ishikawa, and Y.Arakawa. Observation of the coupled exciton-photon mode splitting in a semiconductor quantum microcavity. *Phys. Rev. Lett.*, 69:3314, 1992.

[133] M. S. Skolnick, T. A. Fisher, and D. M. Whittaker. Strong coupling phenomena in quantum microcavity structures. *Semicond. Sci. Technol.*, 13:645, 1998.

[134] J. J. Hopfield. Theory of the contribution of excitons to the complex dielectric constant of crystals. *Phys. Rev.*, 112:1555, 1958.

[135] D. R. Tilley. Superradiance in arrays of superconducting weak links. *Phys. Lett.*, 33A:205, 1970.

[136] H. Haken. *Laser Theory*. Springer-Verlag, Berlin, 1984.